nature communications

Article

https://doi.org/10.1038/s41467-023-38380-1

4D nanoimaging of early age cement hydration

Received: 18 November 2022

Accepted: 26 April 2023

Published online: 08 May 2023

Check for updates

Shiva Shirani[1], Ana Cuesta[1], Alejandro Morales-Cantero[1], Isabel Santacruz[1], Ana Diaz[2], Pavel Trtik[3], Mirko Holler[2], Alexander Rack[4], Bratislav Lukic[4], Emmanuel Brun[5], Inés R. Salcedo[6] & Miguel A. G. Aranda[1]

Despite a century of research, our understanding of cement dissolution and precipitation processes at early ages is very limited. This is due to the lack of methods that can image these processes with enough spatial resolution, contrast and field of view. Here, we adapt near-field ptychographic nanotomography to in situ visualise the hydration of commercial Portland cement in a record-thick capillary. At 19 h, porous C-S-H gel shell, thickness of 500 nm, covers every alite grain enclosing a water gap. The spatial dissolution rate of small alite grains in the acceleration period, ~100 nm/h, is approximately four times faster than that of large alite grains in the deceleration stage, ~25 nm/h. Etch-pit development has also been mapped out. This work is complemented by laboratory and synchrotron microtomographies, allowing to measure the particle size distributions with time. 4D nanoimaging will allow mechanistically study dissolution-precipitation processes including the roles of accelerators and superplasticizers.

Portland concrete is the world's largest fabricated commodity, ~20 billion tonnes/yr. The enormous production of Portland cement (PC), ~4 billion tonnes/yr, results in ~2.7 billion tonnes/yr of CO_2 emissions[1]. Therefore, there are many attempts to decrease the cement CO_2 footprint[1,2]. In order to rationally design approaches to decrease the embodied carbon content of binders, maintaining the performances, cement hydration understanding is key. Unfortunately, there are many unanswered questions[3] regarding the complex dissolution and precipitation processes that lead the setting and early hardening of cements[4].

The hydration of PC can be divided into five periods[3], see Fig. 1b. Stage-I is the initial dissolution (first minutes); stage-II is the low activity, induction, period (some hours); stage-III is the acceleration (several hours until the maximum of the heat flow trace); stage-IV is the deceleration (tens of hours); and stage-V is the diffusion-controlled hydration (months to years). There was a strong debate about the mechanism responsible of the induction period. However, it is now accepted that it is the dissolution controlled by undersaturation[5] and not the protective membrane theory. Conversely, there is no agreement in the mechanism(s) to explain the transition from acceleration to deceleration, when there is a degree of hydration of just 10-20% and plenty of space for the hydrates to grow. The most advanced theories, recently discussed[6], are based on heterogeneous nucleation and growth within confined regions taking into account the initial particle size distributions[7], for instance, see the reaction zone hypothesis[8]. There are alternatives[9] like the needle model[6] where alite, the most abundant component of PC, hydrates[10,11] to yield nonstoichiometric calcium-silicate-hydrate (C-S-H) gel[12], which nucleates and grows as needles. Neither the dissolution of small grains, nor water diffusion, nor etch-pits coalescence, nor C-S-H gel impingement −alone− can currently explain the transition from the acceleration to the deceleration periods[3]. The factors affecting the C-S-H gel growth in these two periods, III and IV, are not known. Moreover, the role of etch-pits[13] needs to be better understood as well as the consequences of the spatial gap which opens between the dissolving (inward) alite grains and the growing (mainly

[1]Departamento de Química Inorgánica, Cristalografía y Mineralogía, Universidad de Málaga, 29071 Málaga, Spain. [2]Laboratory for Macromolecules and Bioimaging, Paul Scherrer Institut, 5232 Villigen PSI, Switzerland. [3]Laboratory for Neutron Scattering and Imaging, Paul Scherrer Institut, 5232 Villigen PSI, Switzerland. [4]ESRF-The European Synchrotron, 71 Rue des Martyrs, 38000 Grenoble, France. [5]Université Grenoble Alpes, Inserm UA7 STROBE, 38000 Grenoble, France. [6]Servicios Centrales de Apoyo a la Investigación, Universidad de Málaga, 29071 Málaga, Spain. e-mail: g_aranda@uma.es

https://doi.org/10.1038/s41467-023-38380-1

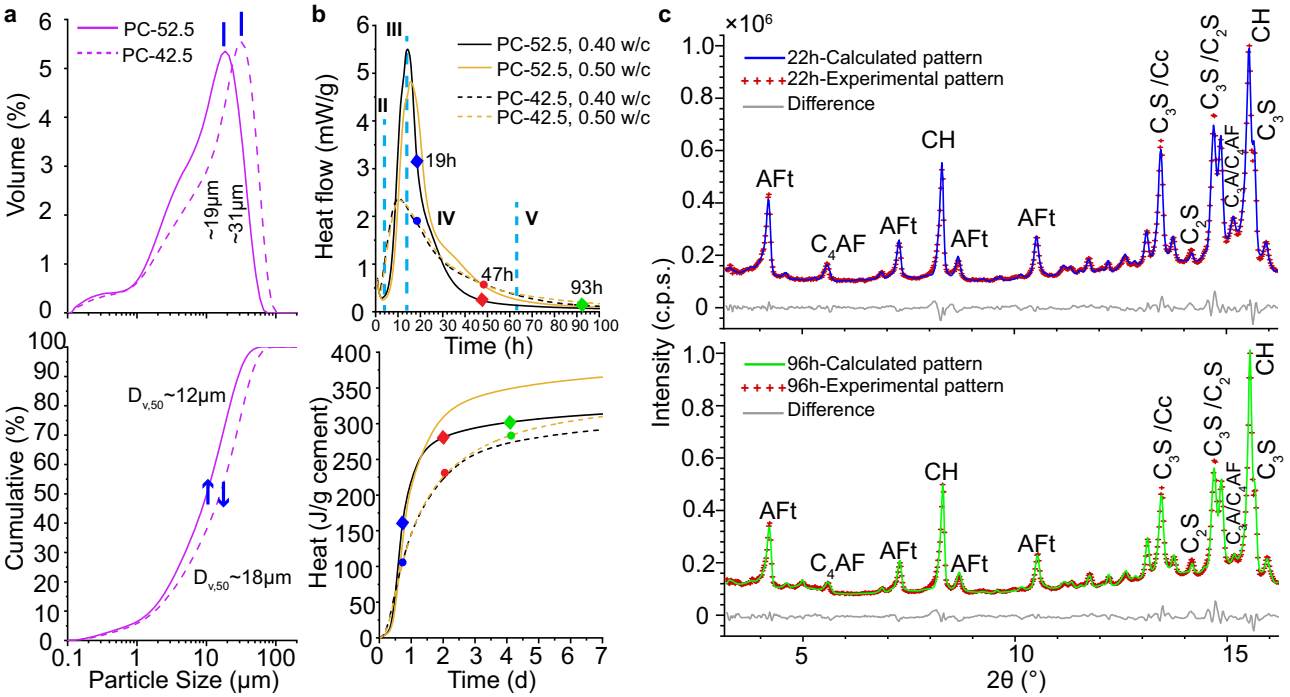

Fig. 1 | Initial characterization of the employed Portland cements. a Textural analysis of the two cements: PC-52.5 and PC-42.5, with Blaine values of 409 and 368 m^2kg^{-1}, respectively. (top) Particle size distributions, (bottom) cumulative volume variation as measured by laser scattering. **b** Isothermal calorimetric study, T = 25 °C, for the cement pastes prepared with w/c values of 0.50 and 0.40, referenced to 1 g of anhydrous cement. (Top) Heat flow curves (where the typical hydration stages are sketched), (bottom) cumulative heat traces for the two cements. **c** Laboratory Rietveld plots (MoKα_1 radiation, λ = 0.7093 Å) for PC-52.5 paste, w/c = 0.40, within a capillary of 1 mm of diameter. The main diffraction peaks are labelled with the contributing crystalline component by using the cement notation: tetracalcium aluminoferrite (C_4AF), belite (C_2S), alite (C_3S), tricalcium aluminate (C_3A), calcite (Cc), portlandite (CH) and ettringite (AFt). (Top) Pattern collected at 22 h, (bottom) pattern collected at 96 h of hydration.

outward) C-S-H gel[14,15]. Finally, the density evolution of the C-S-H gel shells is also unknown.

On the one hand, in situ laboratory[16] and synchrotron[17] powder diffraction allow following the phase development with time. These studies yield volume-averaged information which misses any spatial feature like particle size dependence. On the other hand, electron microscopy (EM) techniques yield very valuable information, with high spatial resolution, but they only give snapshots, as the experimental conditions are not compatible with the hydration in relevant conditions. In situ tomography[18,19] can contribute to filling this gap. In cements, modelling[20] and microstructural characterization methods[21] acknowledge the growing importance of X-ray microtomography (µCT) in their different modalities[22]. Moreover, µCT is being widely used[23] and in particular to follow in situ 4D (3D + time) some specific features of cement hydration[24–33]. In the last three years, important advances have been reported including: i) the automated correction for the movement of suspended particles at very early ages[34] which allowed to follow in situ PC hydration after water mixing[35]; ii) to follow the fast dissolution of plaster and the precipitation of gypsum[36]; iii) the simultaneous use of neutron and laboratory X-ray tomographies for in situ studying the microstructural changes of PC mortars on moderate heating[37]; and iv) the measurement of alite particle dissolution using fast synchrotron nano X-ray computed tomography[38,39]. However, none of these 4D imaging works combine the stringent four requirements needed for carrying out relevant contributions to the understanding of the mechanism(s) of Portland cement hydration at early ages: (i) water to cement mass ratio (w/c) close to 0.50, (ii) submicrometer spatial resolution, (iii) good contrast to be able to identify the different evolving components (more than eight), and (iv) relatively large scanned volume to allow hydration to progress with appropriate particle sampling, the particle sizes of commercial PCs have $D_{v,50}$∈10-20 µm. In particular, hard X-ray synchrotron microtomography has not the required submicrometer spatial resolution neither sufficient component contrast[35,40], hard X-ray synchrotron nanotomography has not the required contrast between the components to be able to classify the hydrates[38,39] and soft X-ray synchrotron nanotomography has the contrast but it requires very large w/c ratios and very small fields of view which does not allow the hydrates to growth in relevant condition (i.e. confined space with low water-cement ratios)[32].

So far, ptychographic X-ray computed tomography (PXCT)[41], which merges scanning X-ray microscopy and coherent diffraction imaging[42–44], met the first three requirements. Hence, it was applied to several binders within capillaries of ~40 µm of diameter[45,46] using a photon energy of 6.2 keV. The second study[46] provided valuable information about C-S-H gel hydrated for 5 months: an average stoichiometry of $(CaO)_{1.80}(SiO_2)(H_2O)_{3.96}$ with a mass density of 2.11 gcm^{-3} and an electron density of 0.64 $e^-Å^{-3}$. Moreover, it allowed quantifying a 6.4 vol% of a second amorphous component, iron-siliceous hydrogarnet, with 2.52 gcm^{-3} and 0.76 $e^-Å^{-3}$. Here, we have used PXCT in near-field configuration[44,47] to acquire data in a record-thick capillary of ~160 µm, employing a higher photon energy, 8.93 keV. This configuration, and the iterative algorithms that allowed the reconstructions[44], now meet simultaneously the four stringent requirements with current data collections of 3-4 h allowing 4D measurements of spatially resolved data during the first four days of cement hydration. On the one hand, the relatively slow overall acquisition time is the main limitation of this work, but this is expected to improve, see last section. On the other hand, the excellent spatial resolution and contrast of ptychographic nanotomography gave quantitative values of relevant parameters in the dissolution-precipitation processes like alite spatial dissolution rates

https://doi.org/10.1038/s41467-023-38380-1

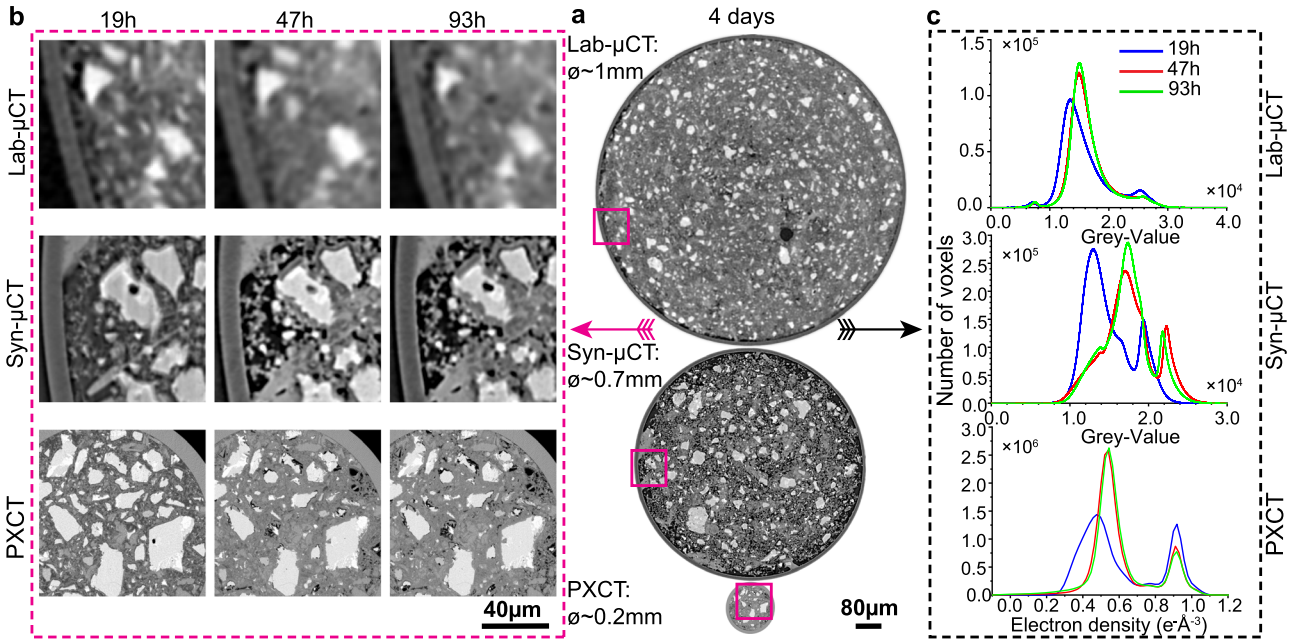

Fig. 2 | In situ multicontrast X-ray tomographic studies of cement hydration. **a** Selected orthoslices for the three imaging approaches. (Top) Attenuation-contrast laboratory data (Lab-µCT) for a PC-52.5 paste with w/c = 0.40. (Middle) Inline propagation-based phase-contrast synchrotron data (Syn-µCT) for a PC-42.5 paste with w/c = 0.50 [phases retrieved by using the Paganin algorithm[51]], (bottom) Quantitative phase-contrast, phases retrieved by near-field PXCT for a PC-52.5 paste scanning a region with w/c~0.40. The thicknesses of the capillaries are given. **b** Enlarged views for the three approaches, at the three hydration ages, to qualitatively illustrate the quality of the data (contrast and spatial resolution). Clinker minerals are seen as whitish particles, porosity as darkish regions, and hydrates have intermediate grey tones. **c** Histograms for the different tomographic studies and hydration times. The histograms were obtained by computing the largest possible volumes without including the glass capillary walls.

and etch-pit growth rate. These values can help to test the above described models.

Result and discussion

Initial cement analysis and cement hydration study

Two commercial PCs have been used and their laboratory X-ray powder diffraction (LXRPD) patterns were analysed by the Rietveld method, see Fig. S1. The elemental and mineralogical analyses are given in Tables S1 and S2, respectively. As reported in Table S2, the anhydrous cements are mixtures with more than eight crystalline phases. The cements have very similar elemental and mineralogical compositions but differ in their textural properties, see Fig. 1a and Table S3. The specific surface areas for PC-52.5 and PC-42.5 were 2.27 and 1.25 m^2g^{-1}, respectively. PC-52.5, with finer particles $D_{v,50}$~12 µm, was used for the PXCT study in order to have more hydrating particles in the analysed volume. It is noted that, in a very recent nanotomographic study[7], researchers milled alite very extensively, all particles<10 µm, in order to fit them within a small field of view (FOV) of ~50 µm. PC-52.5 was used for the PXCT and laboratory µCT imaging studies and the additional laboratory characterization. PC-42.5, with slightly larger average particle size, was used for the synchrotron µCT imaging study.

The calorimetric study, see Fig. 1b, gave the hydration kinetic features at the relevant w/c ratios of 0.50 and 0.40. Table S4 reports the cumulative heat at the hydration times where the imaging data were acquired. Moreover, it also lists the degree of hydration (DoH) at those times to be used as a reference in the imaging studies; for a detailed explanation of this type of calculation, see ref. 48. As expected, PC-52.5 releases more heat than PC-42.5, mainly because of its finesse. The DoH at the maxima of the heat flow peaks were 19% and 10% for PC-52.5 and PC-42.5, respectively. These values are well-known[3,49,50] but they cannot be explained by current models.

Figure 1c displays the LXRPD Rietveld fits for hydrating PC-52.5 taken in the same capillary where the Lab-µCT imaging study was carried out. The in situ LXRPD data were analysed by the Rietveld method resulting in the quantitative phase analyses reported in Table S5. From these data, the DoHs of the different clinker phases are derived at 22, 50 and 96 h of hydration, also used as reference.

In situ X-ray tomographic studies of cement hydration

Two additional in situ X-ray imaging studies were carried out to place the results of the PXCT nanoimaging in context. Emphasis is placed on the accuracy of the results that can only be estimated by comparison. The FOVs were cylinders. Figure 2a displays one orthoslice for each work: (i) Lab-µCT for PC-52.5-w/c = 0.40, FOV = 1200×940 µm (ϕ×L); (ii) Syn-µCT for PC-42.5-w/c = 0.50, FOV = 800 × 1190 µm; and (iii) PXCT for PC-52.5-w/c~0.40, FOV = 186 × 30 µm. Syn-µCT data has a larger w/c value, showing higher porosity (the darkish micro-regions) see the central panel in Fig. 2a. The nominal w/c mass ratio employed to fill the PXCT narrow capillary, 200 µm of nominal diameter, was 0.50, see methods. However, it is very difficult to accurately control the w/c ratio in very thin capillaries. Therefore, the w/c ratio of the scanned volume for the PXCT measurement was measured as previously published[46] and detailed in a subsection of the S.I. The w/c ratio of the scanned volume in the PXCT study was 0.41.

Figure 2b shows enlarged views to illustrate the evolution of the different components and the spatial resolutions. The PXCT study has a much higher resolution and contrast at the expense of a smaller FOV. A minor artefact can be seen in the Syn-µCT data as some borders have grey-values too white. This is a common feature for inline propagation-based data that cannot be fully corrected with the employed Paganin algorithm[51]. Figure 2c shows the histogram evolutions with time. At 19 h (blue traces), there is plenty of free water, which displaces the main peak toward smaller grey-values/electron densities. As hydration progresses, and as expected, the main peak in the histograms densifies and the amount of clinker components decreases. The histogram evolutions for the same cement paste from Lab-µCT and PXCT, see corresponding panels in Fig. 2c, were very similar giving confidence to

https://doi.org/10.1038/s41467-023-38380-1

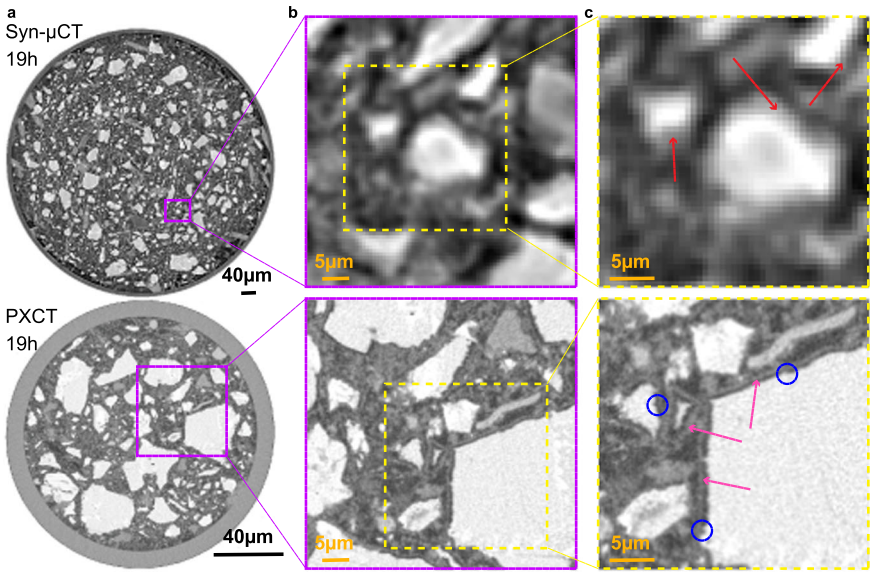

Fig. 3 | Comparison of phase-contrast synchrotron tomography and ptychographic X-ray computed tomography. a Selected orthoslices at 19 h for (top) Syn-μCT [voxel size: 650 nm, total scanned volume: 5.25 10^8 μm^3, overall acquisition time: 5 min], and (bottom) PXCT [voxel size: 186.64 nm, total scanned volume: 8.15 10^5 μm^3, overall acquisition time: 3 h, 55 min]. **b** Enlarged views of the highlighted regions (purple squares) in **a**, in order to illustrate the level of detail that can be observed with these imaging modalities. Every voxel in Syn-μCT image starts to be evident. **c** Further enlarged views to illustrate the maximum level of detail that can be observed. (Top) The Syn-μCT image shows whitish particles (anhydrous cement particles) surrounded by hydrates (greyish voxels) which are highlighted by red arrows. (Bottom) The PXCT data, at the same magnification, shows a much higher level of detail. The C-S-H gel shells surrounding the alite particles are clearly visible (pink arrows). There is a water gap between the shell and the alite grain due to the inward dissolution of alite. Moreover, etch-pits on the surfaces of the alite particles are also visible (blue circles). The highest spatial resolution and better contrast of PXCT data allow visualizing submicrometre features of the dissolution-precipitation processes which are not visible in propagation-based Syn-μCT. Conversely, propagation-based Syn-μCT permits to scan much larger volumes in much smaller acquisition times, showing the complementary nature of both techniques.

the relevancy of the nanoimaging results in spite of the limited amount of volume scanned to have submicrometer resolution. The grey-values in the Lab-μCT study, see Fig. 2c (top panel), are related to the attenuation coefficients of the components in this PC-52.5 paste, but the relationship is not quantitative due to the polychromatic nature of the employed radiation. Conversely, the electron density values obtained for the same paste by PXCT are quantitative. Therefore, the grey scales in the Lab-CT and the electron densities in the PXCT datasets cannot be directly related as they derived from the imaginary and the real part of the refractive index of every component.

The spatial resolution was characterised by two approaches as recently reported[52]. The procedures are thoroughly detailed in Supplementary Information (SI). On the one hand, the spatial resolution can be determined by the edge sharpness across selected interfaces. A point spread function (PSF) used to determine the spatial resolution of the images as ISO/TS 24597 defines the Gaussian radius of the PSF as the resolution, which equals a change between 25%–75% grey value along the studied interfaces[38]. The spatial resolutions, determined by this approach, were 250(25) nm, 264(25) nm, 272(34) nm, 748(19) nm and 2.21(17) μm, for PXCT-19h, PXCT-47h, PXCT-93h, Syn-μCT and Lab-μCT datasets, respectively. As examples of this procedure, Figs. S2–S4 display line profiles of sharp interfaces between high (i.e. alite) and low density (i.e. porosity) components within the capillaries. On the other hand, Fourier-shell-correlation (FSC)[53] has also been employed to estimate spatial resolution. Figs. S5–S7 displays the FSC traces for the three imaging modalities. The agreement between both approaches is satisfactory for Syn-μCT and Lab-μCT, but not for PXCT. The worse spatial resolution estimated by FSC for PXCT is very likely due to the low number of projections, i.e. 420, which make the subtomograms employed in the FSC calculation severely undersampled. Moreover, Fig. 3 compares the level of details that can be obtained with Syn-μCT and PXCT at 19 h of hydration. The latter shows the C-S-H gel shell and a porosity gap between the shell and the dissolving alite particle that it is not observed in the Syn-μCT data because the lack of spatial resolution and contrast.

4D nanoimaging of cement hydration

In situ near-field PXCT data were taken as detailed in methods. To ensure the relevance of the results, the scanned volumes were assessed. Firstly, the w/c ratio was 0.41(2), as determined from the absorption data[46], see Table S6. This w/c value is fully consistent with the obtained degrees of hydration. Secondly, possible signatures of radiation damage were explored. The mean electron density values of the whole sample were 0.600, 0.599 and 0.591 e$^-$Å^{-3}, for the 19, 47 and 93 h datasets, respectively. The spatial resolution from FSC was 470 and 500 nm, for the 47 and 93 h data, respectively. Hence, radiation damage cannot be discarded but it is small, if any. Thirdly, seven sets of components within the tomograms were identified: air, water, AFt/C-S-H gel/others, CH, Cc, C_3A/C_3S/C_2S and C_4AF, using the electron density and the absorption data in the bivariate plots, see Figs. S8 and S9. The calculated electron density and attenuation length values are given in Table S7, and Fig. S10 displays the histogram evolution in logarithm scale. The differences between the theoretical electron densities and the measured ones are mainly due to partial volume effects. For instance, portlandite, i.e. $Ca(OH)_2$, has a theoretical electron density value of 0.69 e$^-$Å^{-3}. The measured values at 19 and 93 h were 0.62(2) and 0.651(5) e$^-$Å^{-3}, see Table S7. These numbers are 6-10% smaller than the theoretical one, with the difference being higher than the errors of the measurements, which are estimated in 2-3%[46,54]. This difference is very likely due to the presence of residual water porosity below the spatial resolution of the measurements, which we refer to partial volume effects. It should be noted that individual C-S-H nanoparticles have sizes close to 5 nm[12,55] much smaller than the spatial resolution of this work, i.e. ~250 nm. Therefore, the C-S-H regions analysed here very likely contain other components like gel and capillary water porosities and interspersed calcium hydroxide. It should also be noted

https://doi.org/10.1038/s41467-023-38380-1

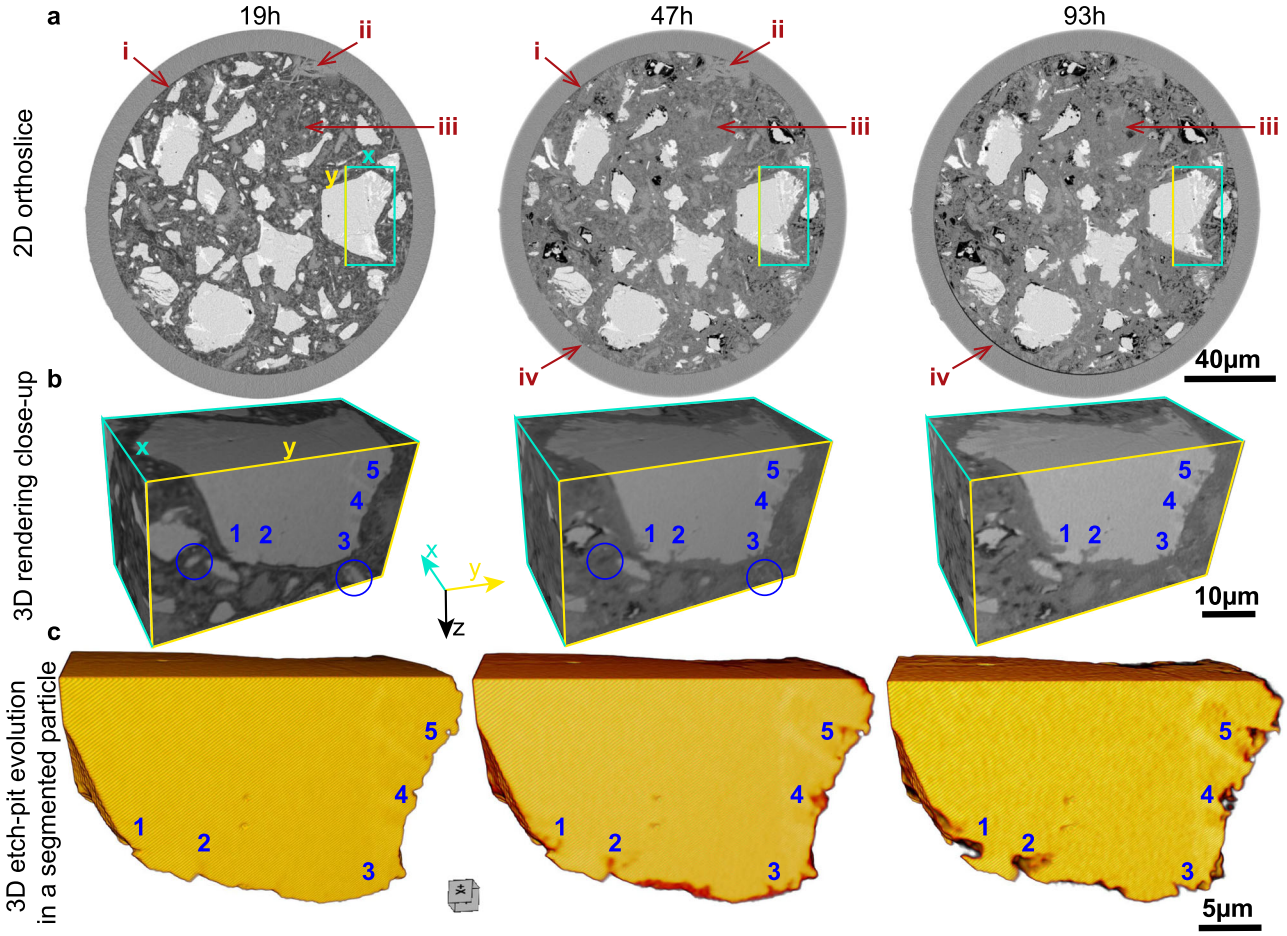

Fig. 4 | 4D nanoimaging study highlighting the etch-pit evolution. a PXCT orthoslices at the studied hydration ages showing the evolution of the PC-52.5-w/c~0.40 paste which includes: i) dissolution of cement particles, ii) portlandite growth, iii) C-S-H gel densification at 2 and 4 days, and iv) chemical shrinkage. Examples of these features are labelled with red arrows. **b** 3D rendering of a volume including a fraction of large alite particle highlighted in **a**, to show the evolution of five selected etch-pits, which are labelled. These images also show the full reaction of small alite particles, featured with blue circles. These 3D rendered views do not show exactly the electron densities as they are affected by visualization features like the lighting source. **c** 3D representation of the segmented particle, shown in the previous panels, to highlight the evolution of the etch-pits. It is noted that three branches within etch-pit #1 at 47 h coalesce at 93 h of hydration which may mean a reduction in surface with hydration time.

that the employed stoichiometry for C-S-H gel, i.e. $(CaO)_{1.80}(SiO_2)(H_2O)_{4.0}$[56,57], is an assumption and slightly smaller Ca/Si ratios, ~1.70, have also been reported[12,58]. On the other hand, ettringite and portlandite particles have larger sizes, usually ranging 1-5 μm[3], and they can be imaged in the present work. In any case, partial volume effect (the presence of components contributing below the spatial resolution of the measurements) is always taking place in cement pastes as some hydrates may have quite small particle sizes[17].

The crux of our results is the 4D submicrometer features of cement hydration, see Figs. 4 to 6. Supplementary Movie 1 also shows a summary of the main findings. It is underlined that PXCT readily distinguishes air and water porosities because of their difference in electron densities, 0 and 0.33 $e^{-}Å^{-3}$, respectively; when the phase retrieval is carried out quantitatively[54]. The paste evolution is displayed in Fig. 4a, showing a partly reacted binder plenty of capillary water at 19 h. The main change from 19 to 47 h is the large consumption of capillary water (dark-grey regions in Fig. 4a-19h) and the densification of C-S-H gel. The main evolution from 47 to 93 h is the appearance of chemical shrinkage, evidenced by the development of many air-containing (black) regions. Importantly, Fig. 4c and Figs. S11–S12 show the evolution of etch-pits with time, including etch-pit coalescence, which contributes, in addition to the consumption of small alite particles, to the decrease of specific surfaces in the deceleration period. The etch-pit growth rate was estimated, as detailed in SI, from the analysis of 27 dissolving regions in five alite grains. The resulting rate, between 19 and 47 h, was 41(29) nm/h. The etch-pit growth rate between 47 and 93 h was slower with a large variability, 7(8) nm/h, showing that the water diffusion is already limiting hydration. The large variability in the growth rates of the etch-pits is highlighted in Fig. S13. Etch-pits at very early ages, i.e. 2-4 h, were imaged by EM with sizes of ~15 nm[59] which is out of in situ PXCT capabilities.

Chiefly, the spatial dissolution rate of alite was determined from the study of the surface evolution of selected particles, see Fig. 5a and Figs. S14–S19, as examples. C_2S particles were identified and excluded from this analysis, because they do not have C-S-H shells at 19 h of hydration. C_3A particles were also recognised and discarded because of their smaller electron density values, i.e. ~0.91 $e^{-}Å^{-3}$, 5% lower than that of alite. From 22 measurements along different surfaces, the dissolution rate between 19 and 47 h was 25(14) nm/h. This value compares well with 36 nm/h from the reaction zone model[8] but poorly with 84 nm/h obtained from the same dataset by using the boundary nucleation and growth model[60]. Moreover, this spatial dissolution rate can also be estimated from the segmentation results presented in the next subsection. Based on the quantitative analysis derived from Machine Learning (ML) segmentation of the PXCT datasets (for the C_3S/C_2S class, dark brown colour code in the 3D visualization of Fig. 7),

https://doi.org/10.1038/s41467-023-38380-1

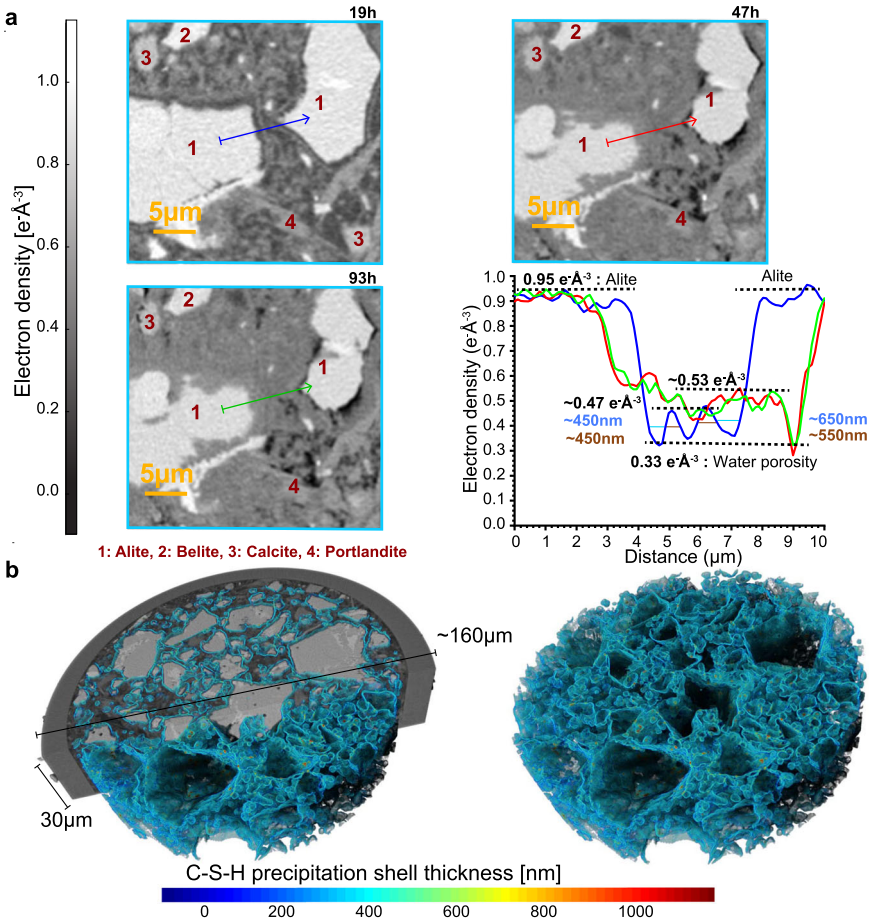

Fig. 5 | C-S-H gel shells and their evolution. a Selected 2D views of the PXCT data. The fourth panel displays the electron density profiles corresponding to the straight lines in the previous plots. At 19 h, the C-S-H shell covers every alite particle. The line profile at 19 h, blue trace in the fourth panel, shows water porosity (gap) between the alite particle and its shells. For these two particles, the shells have a thickness of ~550 nm and an electron density of ~0.47 e·Å^{-3}. This C-S-H densifies at 2 days to ~0.53 e·Å^{-3}. The alite particles partly dissolve and air porosity starts to develop (black regions). **b** 3D rendered views of the ML segmented C-S-H gel shells with the colour signalling its thickness for the 19 h tomogram. (left) View superimposing the C-S-H shells to half of the studied capillary. (Right) 3D view of the segmented C-S-H shells.

it is possible to derive an average spatial dissolution rate. Mathematical morphology tools were used to retrieve the outer layer of the segmented grains at 19 and 47 h. Subsequently, the average distance between these outer layers was computed for each grain, giving a mean value of 1.92 pixels (i.e. ~13 nm/h). This value is smaller than that obtained from the analysis performed in 2D slices for alite, 25 nm/h. However, it should be noted that in the segmentation calculation, alite and belite were classified together and therefore, the obtained spatial dissolution rate is underestimated as belite does not dissolve at early ages. Table S5, Rietveld analysis results, indicates that the amount of belite is half of that of alite during this stage. Therefore, the spatial dissolution rate can be corrected. The alite spatial dissolution rate should be close to 13/0.67 or 19 nm/h. This value agrees relatively well with 25 nm/h, obtained from 22 measurements in 2D slices, given the number of approximations which took place for both calculations.

The analysis of the 12 largest Hadley grains (hollow-shell microstructure, see Fig. 6a, b and larger view at Fig. S20)[14,15,61,62] gave 2.6(3) μm of size. Here, their time-evolution can be followed and it is noted that hollow regions are filled with water at 19 and 47 h but dried at 93 h, see Fig. 6a, directly evidencing the water diffusion through the C-S-H shells. Additionally, the analysis of the 15 smallest alite particles leaving an unhydrated, very small, core gave an average particle size of 3.4(5) μm. Therefore, it is concluded that alite particles smaller than ~3.0 μm are fully hydrated in the 4-19 h range, leading to a spatial dissolution rate of ~100 nm/h. The largest size of the Hadley grains found here agrees well with previous works[61,62] (at 24 h) reporting a maximum size of 5.0 μm with shells of 500 nm. Hence, it seems to be a 3-4 fold difference between the spatial dissolution rate of small alite grains in the acceleration period and that of large alite grains in the deceleration stage.

Figure 5a and Figs. S14–S17 show views detailing the hydration of alite particles and showing the C-S-H gel shells that surround all alite grains enclosing a gap. Similar plots containing belite particles, Figs. S18–S19, did not show gaps, as expected. C-S-H shells on alite have been extensively analysed by EM[6,14,15,61,63], but here their electron density and spatial evolutions can be followed. The C-S-H shells for these two alite particles, Fig. 5a, have ~0.47 e·Å^{-3} which increases to ~0.53 e·Å^{-3} at 47 h. This means a very low mass density shell. For instance, ettringite, a phase with 32 crystallization water molecules has ~0.56 e·Å^{-3}, and mature C-S-H gel, with $(CaO)_{1.8}(SiO_2)(H_2O)_{4.0}$ composition, i.e. including gel pore water, had 0.64 e·Å^{-3} [46]. As this result is critical for discarding diffusion as the mechanism for the deceleration period, a larger study was carried out. 20 shells were analysed giving 0.51(4) e·Å^{-3} and 500(120) nm, for the average electron density and thickness, respectively. Moreover, this study also yields the average width of the gap, 490(140) nm. At 24 h, the thickness of the shells and gaps were reported as ~500 and ~300 nm from EM[62]. Moreover, a gap of 490 nm developed in 15 h, time between the end of the induction period and the first nanoimaging measurement, which means an alite spatial dissolution rate of ~33 nm/h. Therefore, the dissolution rates of

https://doi.org/10.1038/s41467-023-38380-1

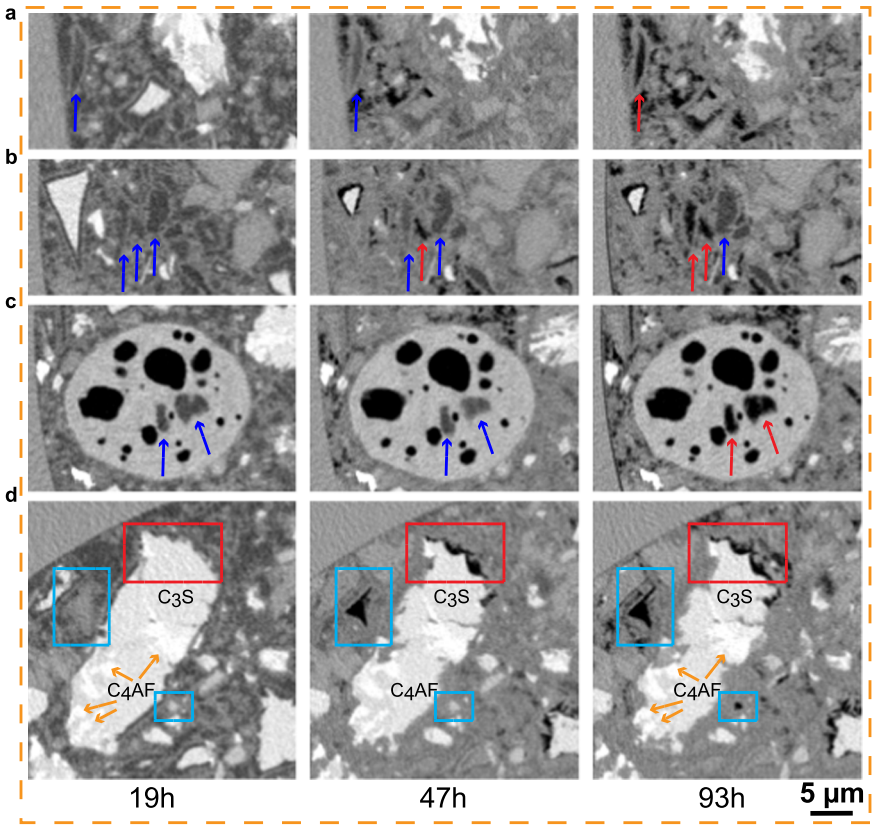

Fig. 6 | Hydration time evolution of selected nano-features directly visualised by near field PXCT. a Hollow-shell microstructure, also known as Hadley grain. The Hadley grains are fully hydrated small alite particles that contain a void within the original boundary of the anhydrous grain. The hollow regions are filled with water at 19 and 47 h (blue arrows) but dried at 93 h (red arrow) directly evidencing the porosity of the C-S-H shells. **b** Evolution of water porosity (dark-grey) to air porosity (black). It is noted that at 47 h, a tiny pore of about 1 µm size is already dried, but being very close to two larger water-filled pores, of sizes larger than 2 µm. This observation remarks the heterogeneity in cement hydration. It can be deduced that the relative humidity is not constant, at a given time, through the sample. This is due to a set of factors including the barriers to water diffusion and the crystallization/precipitation of different hydrates with quite different water contents, for instance ettringite and portlandite. **c** Evolution of water porosity inside a calcite grain, if connected to the surface. This calcite comes very likely from the limestone addition to the Portland cement as quantified in the anhydrous material, see Table S2. **d** Evolution of alite dissolution (hydration) which stops at the C_4AF intergrown regions, highlighted by brown arrows. Moreover, alite hydration also stops as soon as air porosity (pore drying) develops on the surfaces of the anhydrous grains, see red rectangles. This panel also illustrates that (recently precipitated) hydrates can dissolve, see blue rectangles.

large and small alite grains differ at least three-fold, which should be considered for modelling. To further study the C-S-H shells, the components were segmented by ML as described in methods following the procedure summarized in Fig. S21. Subsequently, the C-S-H shells were segmented as detailed in Fig. S22. The results of the C-S-H shell segmentation are presented in Fig. 5b with a relatively constant shell size of ~450 nm. The Supplementary Movie 2 displays a full picture of the segmented shells. Fig. S23 shows a 2D comparison of the raw data and the resulting segmented shells yielding a reasonable good agreement.

Finally, Fig. 6 shows interesting (directly-observed) *nano-features*. Figure 6a, b exhibit the water diffusion through the C-S-H shells for some Hadley grains between 19 and 93 h of hydration. Larger regions are shown in Figs. S20 and S24, respectively. Figure 6c displays the water porosity evolution within a calcite particle evidencing that some small pore regions, 2-3 µm in size, were water filled at 19 and 47 h and dried at 93 h, see also Fig. S25. This observation directly explains the indirect result of water transport within limestone grains obtained by X-ray dark-field tomography[30]. Figure 6d, larger view in Fig. S26, shows how hydration progresses along the surface of an alite particle but it stops at C_4AF intergrown regions, evidencing the importance of alkanolamines at early ages as accelerators[64]. Moreover, Fig. 6d also illustrates that C-S-H gel can dissolve to leave a dry capillary pore. Fig. S27 presents at 47 h the full dissolution of a grain of a size of 4 µm at 19 h. This implies a very large dissolution rate, >75 nm/h, which is likely C_3A.

Segmentations of the X-ray tomographies

Figure 7a displays orthoslices of the trained models overlaid on the three raw datasets and Fig. 7b shows the time evolution of the segmented components. For the PXCT study, the average electron densities and the segmented volumes are reported in Table S8. Moreover, Fig. S28 displays the evolution of the segmented water capillary porosity. It seems that at 19 h, the free water is preferentially located close to the walls of the capillary. This could be related to the 'wall effect' well known in mortars and concretes, where the cement paste content (water and fine cement particles) is slightly higher near the wall of the container respect to the larger aggregate particles which are preferentially arranged towards the centre. This feature, and its implications in the interfacial transition zone, has been extensively studied by numerous techniques, including synchrotron microtomography, see for example[65]. For cement pastes, higher porosity near the capillary wall has been observed by synchrotron microtomography[24]. For a water-rich alite paste, wall effect was clearly observed by PXCT where the resulting C-S-H gel had higher water content near the capillary wall[66]. In order to quantitatively study this feature, the scanned capillary was divided into two volumes, a central cylinder with half of the

https://doi.org/10.1038/s41467-023-38380-1

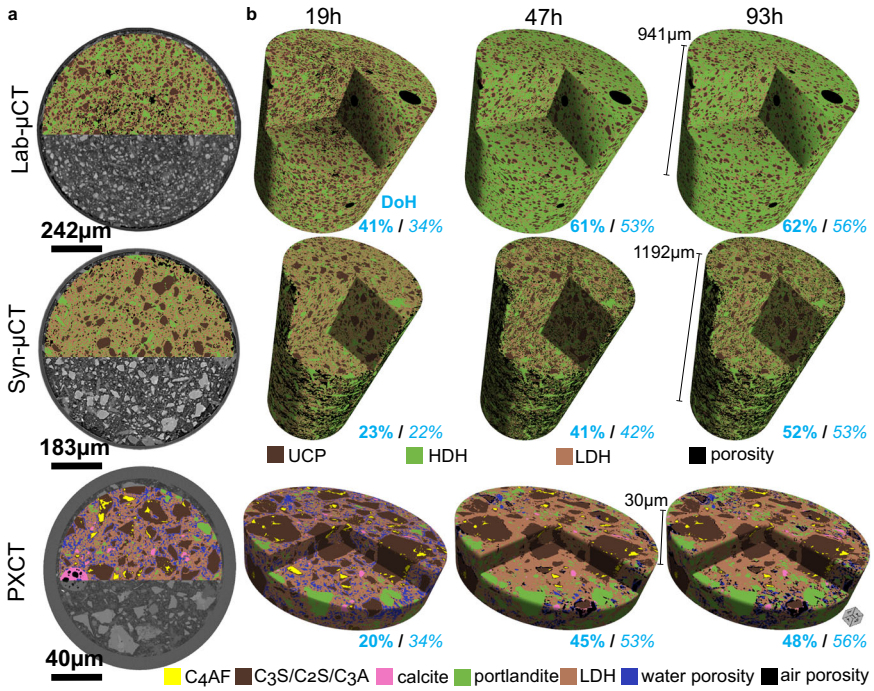

Fig. 7 | ML training and segmentation results for the three datasets with different contrast mechanisms. a ML trained models overlaid on the three raw datasets. **b** 3D rendering of the segmented volumes at the three studied hydration ages. The DoH values determined from microtomography (bold) are compared to the ones from calorimetry (italics). The number of quantified components in the Lab-μCT and Syn-μCT datasets are four: i) porosity (air and water), ii) LDH (low-density hydrates: mainly C-S-H gel and ettringite), iii) HDH (high-density hydrates: mainly portlandite and calcite), and iv) UCP (anhydrous cement particles: all unreacted clinker phases). The number of quantified components in the PXCT datasets is seven: i) air porosity, ii) water porosity, iii) LDH (low-density hydrates: mainly C-S-H gel and ettringite), iv) portlandite, v) calcite, vi) $C_3A/C_3S/C_2S$, and vii) C_4AF. It is noted that with the quality of the data reported in this study (spatial resolution and electron density contrast), it is not possible to disentangle low-density from high-density C-S-H.

radius and the outer region up to the glass capillary wall. The mean electron densities were computed, but the voxels with electron density smaller than 0.24 $e^{-}Å^{-3}$, air porosity, were not included in order to minimise any bias due to the shrinkage/pore drying. The results for the centre volume were 0.614, 0.618 and 0.617 $e^{-}Å^{-3}$ for the 19, 47 and 94 h datasets, respectively. The corresponding mean electron density values for the outer region were 0.608, 0.610 and 0.601 $e^{-}Å^{-3}$. The 1% difference between the two regions at 19 h is quite small but not negligible. Hence, the degree of hydration could slightly be a function of the horizontal position of the particles.

The amount of anhydrous components, together with the initial values, allow determining the DoH from the three imaging studies which are reported in Table S9 and summarised in Fig. 7b. Table S9 also gives the DoH from calorimetry and LXRPD as references. The agreement for Syn-μCT is noteworthy likely due to the large volume probed and the relatively good spatial resolution. The DoHs from Lab-μCT are overestimated probably due to the relatively poor spatial resolution and contrast, which do not allow us to quantify the anhydrous particles smaller than ~3 μm. Finally, PXCT yields underestimated values for the DoH likely due to the limited scanned volume.

Importantly, the high resolution and excellent contrast of the PXCT study allowed us to track down the individual hydration evolution of 1407 particles with connected anhydrous volume, at 19 h, of 1 $μm^3$ or larger. For this particle tracking statistical study, they were arbitrarily classified into four groups having connected volumes ($μm^3$) of $1.0 \geq vol_1 > 27.0 \geq vol_2 > 216.0 \geq vol_3 > 1000.0 \geq vol_4$. A rough estimation of their sizes in μm could be $\sqrt[3]{(vol)}$ or $1.0 \geq size_1 > 3.0 \geq size_2 > 6.0 \geq size_3 > 10.0 \geq size_4$. The groups contained 1117, 204, 61 and 20 particles, respectively. The corresponding volume percentages with respect to the overall anhydrous cement particle volume at this hydration age, were 5.4, 12.9, 21.5 and 60.2%. It is not possible to calculate the DoH of these groups at 19 h because there are no reference values at t_0. The degree of reaction, between 47 and 19 h, was 69.4%, 59.3%, 37.2% and 15.9% for the groups classified as vol_1, vol_2, vol_3 and vol_4, respectively, and they account for 12.9, 26.4, 27.7 and 33.0% of the total dissolved volume. In other words, the twenty particles of vol_4 group has a degree of reaction of 15.9% but it accounts for 33% of the dissolved volume in that period. A similar study can be carried out between 93 and 47 h. The degree of reaction during this period decreased to 14.7%, 11.6%, 6.7% and 3.6% for the corresponding groups. In terms of dissolved volume percentage in this period, the values are 6.8, 16.9, 25.3 and 51.0%, respectively. This simple analysis shows that 51% of the observed reaction during this diffusion-limited period is due to the 20 largest particles as they account for a very large fraction of the volume. The strong decrease of hydration rate in this time range is in line with a diffusion controlled hydration stage.

Finally, Fig. 8a displays the hydration evolution of the segmented anhydrous cement particles. It is readily visible that smaller particles dissolve faster than larger ones. Moreover, the segmentation output allows us to classify the particles and to follow their volumes and cumulative volumes, see Fig. 8b. The cumulative volume results for Lab-μCT and PXCT are very similar and in agreement with the expected DoH from calorimetry showing a large variation between 19 and 47 h and a small variation at 93 h. Moreover, the hydration of PC-42.5 is slower because of their larger average particle sizes, with similar DoH variation between the two studied time intervals, see Fig. 8b, in full agreement with their calorimetric traces, see Fig. 1b. This reflects a good accuracy of the obtained results. Finally, it should be noted that the scanned length in the vertical direction, 30 μm, for PXCT is limited taking into account that some alite grains with sizes of 20 μm, or slightly larger, are present in PC cements. This was mitigated by imaging 160 μm in the transversal direction. This type of experiment will benefit from imaging cylindrical volumes with 60-100 μm of height. However, with the current experimental procedure, this would lead to

https://doi.org/10.1038/s41467-023-38380-1

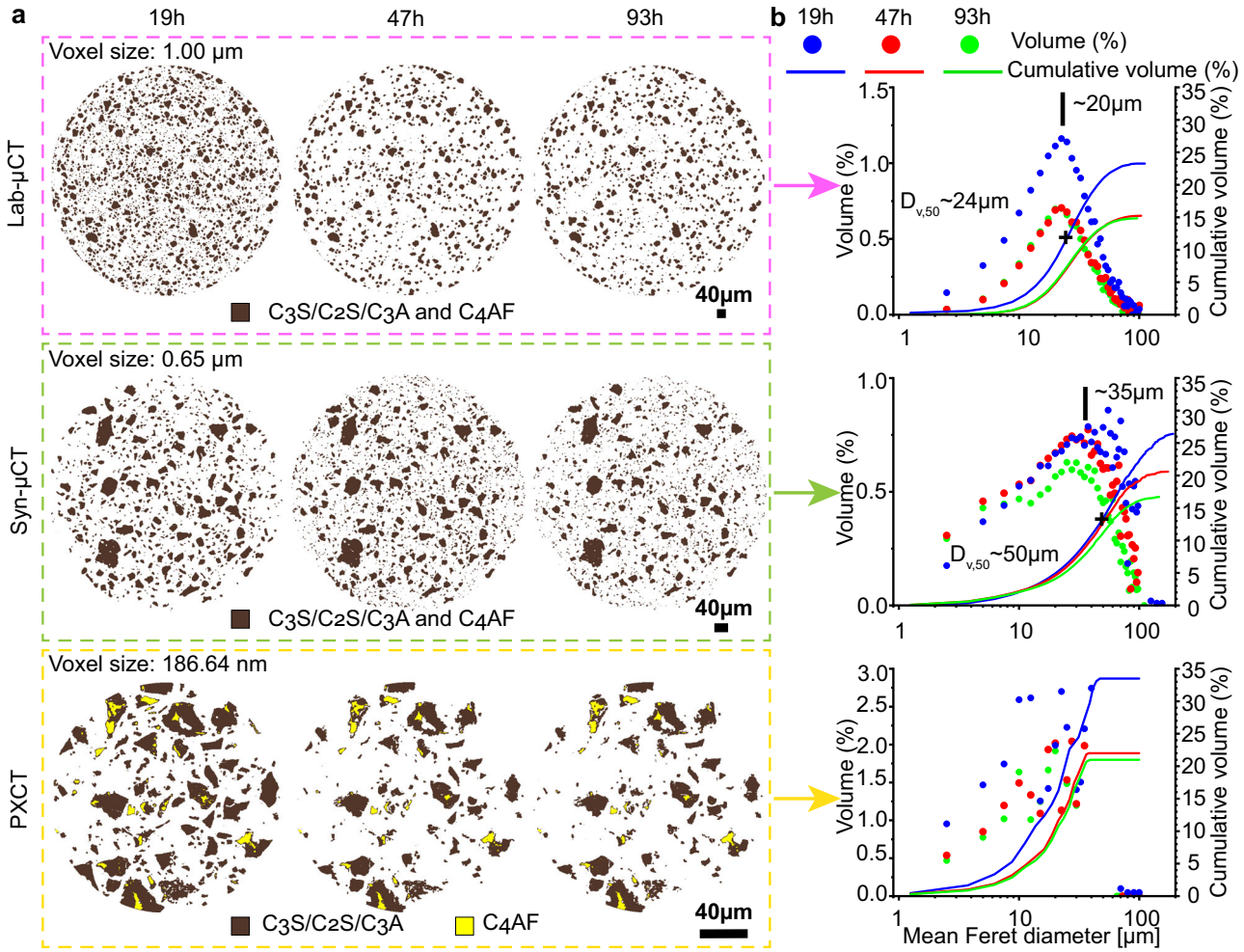

Fig. 8 | Hydration study as a function of time and cement particle sizes. a 2D views of the segmented anhydrous cement particles as a function of time. PXCT data shows that C_4AF hydrates little up to 93 h. This is likely due to the low w/c ratio in the scanned volume and its slow hydration rate. **b** Volumes and cumulative volumes for the anhydrous cement particles as a function of the particle size, represented in logarithmic scale for easy comparison with Fig. 1. The particle sizes are computed as the mean Feret diameter frequency which measures object size along directions. The particles are represented grouped in sets of 2.5 microns, i.e. 0-2.5, 2.5-5.0 µm, etc. The maximum and $D_{v,50}$ values for the Lab-µCT and Syn-µCT are given in the panels. These data are scattered for PXCT because the limited height of the studied cylinder yields a poor representative elementary volume for this feature.

acquisition times larger than 7-9 h and therefore changes due to hydration could take place during an acquisition. Procedures for faster data collection are being explored and they are discussed below.

The hydration of PC, in relevant conditions, has been measured with very high spatial resolution, i.e. 250 nm, and contrast. As expected but not directly measured so far, the hydration of Portland cement at 1 day or earlier is dominated by the small particles, smaller than 3 µm, and the hydration after 3 days is very much dependent of the large alite particles, larger than about 10 µm. The nanoimaging work shows the C-S-H gel shells surrounding every alite grain which does not preclude diffusion. The measured alite spatial dissolution rates, ~100 nm/h for small grains in the acceleration period and ~25 nm/h for large particles in the deceleration stage impose constraints on the cement hydration models. The alite etch-pit growth rate between 19 and 47 h has been estimated as ~40 nm/h, which decreases to ~7 nm/h in the 47 to 93 h interval. Moreover, etch-pit coalescence, the merging of different branches, has also been visually observed. However, better spatial resolution is required for a thorough etch-pit growth rate quantification. The configuration employed here already allows studying the roles of admixtures (accelerators, retarders, superplasticizers, etc.) by measuring C-S-H shell density, C-S-H gel spatial distribution and alite spatial dissolution and etch-pit growth rates. For instance, it would be possible to measure if the acceleration produced by $CaCl_2$ is due to a lower density of the C-S-H shells (higher water diffusion) or if it is mainly due to higher calcium supersaturation.

The current spatial resolution of in situ near-field PXCT, i.e. ~250 nm, could be improved by increasing the number of projections, without larger acquisition times. Moreover, so far the time resolution is modest, i.e. 3-4 h for a complete tomogram, but this is expected to improve in fourth-generation synchrotron sources with tailored beamlines for ptychography. Time resolutions of ~1 h will open the way to accurately study the processes in the acceleration period. However, in these cases, radiation damage could be an issue if the total dose is not kept low. Higher time resolution does not necessarily imply higher doses and therefore possibly larger radiation damage. For instance, sparsity techniques could be coupled to PXCT in order to decrease the overall acquisition time for the whole series by as much as 90%, as recently reported[67]. Another approach could be to use machine learning/deep learning for denoising of datasets collected with much less X-ray dose[68]. On the other hand, gamma irradiation of Portland pastes, mortars and concretes is known to produce water radiolysis finally leading to H_2 microbubbles and calcium peroxide, $CaO_2{\cdot}8H_2O$[69]. Therefore, the signatures of these species should be monitored for studies with high X-ray doses. Higher spatial resolution

and shorter acquisition times will allow to thoroughly study the acceleration stage which will be beneficial to rationally design new accelerator admixtures with the final aim of developing low carbon cements with competitive mechanical strengths and durability performances. Moreover, dissolution-precipitation processes with moderate reaction rates take place also in several other fields like geochemistry or biomaterials, which could benefit from the reported investigation.

Methods

Material provenance and initial characterization

Two different types of commercial cement were used: a CEM I 52.5 R (PC-52.5) and a CEM I 42.5 R (PC-42.5) which conform to EN 197–1. The full characterization of these anhydrous materials is performed with X-ray Fluorescence (XRF) and Laboratory X-ray Powder Diffraction (LXRPD) using the Rietveld Method, see Fig. S1 and Tables S1, S2. Moreover, a polycarboxylate ether (PCE) superplasticiser, containing 35 wt% of the active matter, was employed to efficiently fill the very narrow capillaries required for the PXCT nanoimaging study. The characterisation of this PCE has been recently reported[70].

Textural analysis

The textural characterization was carried out in dry conditions. Particle size distribution (PSD) data were measured by laser diffraction in a MasterSizer 3000 equipment (Malvern). Specific surface areas were determined by N_2 adsorption isotherms in ASAP 2420 equipment (Micromeritics, USA). The air permeabilities were measured with the Blaine fineness apparatus (Controls) according to EN 196–6. The density of the samples was measured with a helium Pycnometer (Accupyc II 1320 Pycnometer, Micromeritics). The resulting data are reported in Table S3.

Isothermal calorimetry

The pastes were prepared using the PC-52.5 and PC-42.5 and with w/c mass ratios of 0.40 and 0.50, respectively. For PC-52.5, 0.43 wt% (by weight of cement) of PCE was used. Water and superplasticizer were mixed by magnetic stirring for 1 min. Then, the cement was mixed with the water/suspension and shaken, for 1 min manually and 1 min with a laboratory vortex mixer. Finally, the pastes were introduced into the glass ampoules. The calorimetric data were taken in an eight-channel Thermal Activity Monitor (TAM) instrument. Data were collected for up to 7 days at 25 °C and at 20 °C and for PC-52.5 and PC-42.5, respectively. The first 45 min were required for the thermal stabilization of the system. The employed conditions mimic the ones used for the imaging studies.

Laboratory X-ray Powder Diffraction (LXRPD) and Data Analysis

The same paste prepared for the calorimetry measurement (PC-52.5-w/c = 0.40) was used to fill the capillaries of ~1 mm in diameter. LXRPD measurements were collected on a D8 ADVANCE diffractometer (Bruker AXS) using strictly monochromatic Mo-Kα_1 radiation ($\lambda = 0.7093$ Å). This diffractometer is located at SCAI, University of Malaga. The incident beam was formed by a primary monochromator with a focusing mirror and a 2 mm anti-scatter slit. Moreover, 2.5° Soller slits were used for the incident and transmitted beams. An EIGER detector (from DECTRIS, Baden, Switzerland) was used which is optimised for Mo anodes. This was used with an aperture of 4 × 21 degrees, working in VDO mode. Data collection was performed from 3 to 35° (2θ) for 2 h and 10 min. Rietveld quantitative phase analysis was performed with GSAS software.

Laboratory X-ray computed microtomography experiment (Lab-μCT)

Lab-μCT experiments were carried out at ~25 °C for the same capillary used in the LXRPD data collection and scanning the same region with time. Lab-μCT experiment was performed on a SKYSCAN 2214 (Bruker) scanner at SCAI, University of Malaga. Images were obtained using an X-ray tube with a LaB_6 source filament and employing a 0.25 mm Al foil to minimise the beam hardening effect. This source was operated at 55 kV and 130 μA. The CCD3 detector with a physical pixel size of 17.427 μm was set in a middle position with a source-to-detector distance of 315.449 mm and a source-to-sample distance of 9.051 mm which yielded a voxel size of 1.00 μm (binning 2 × 2). Finally, the projections were acquired every 0.22° over 360° with a total of 1637 projections per tomogram and using an exposure time of 1.9 s. This results in an overall recording time of 3.5 h per dataset. Image reconstruction of the CTs was carried out using Bruker NRecon software (version 2.1.0.1) and by applying Gaussian smoothing and beam hardening correction.

Because Lab-μCT and LXRPD data were acquired in the same capillary, but not in the same equipment, the description of the timing is important. Lab-μCT data were collected from 17.5 h until 21.0 h, using cement-water mixing time as the reference. This dataset is labelled as 19 h. Then, the capillary was transfer to the diffractometer, in the same room, and the LXRPD data were taken from 21 h 15 min to 23 h 25 min. This dataset is labelled as 22 h. The data collections at 47 h and 93 h followed the same protocol but it is less important at these hydration ages, as the kinetics are slower.

Synchrotron X-ray computed microtomography experiment (Syn-μCT)

PC-42.5 with a w/c ratio of 0.50 was used to prepare the paste for this experiment and PCE was not required. The paste was manually mixed for 3.5 min and then introduced in a capillary of ~0.7 mm of diameter. Inline propagation-based phase-contrast microtomographic data were acquired at ID19 beamline of the European Synchrotron (ESRF) in Grenoble, France. The measurements were performed at 21.5 °C, temperature of the experimental hutch, using a photon energy of 19 keV. The distance between the sample and the detector was 15 mm. The total time to record a full tomogram was 6 min with 0.05 s exposure time. 6000 projection angles were acquired over a 360 degree tomographic scan. For reconstructions, Paganin phase retrieval of the projections was performed[51]. The resulting voxel size was 0.65 μm. Further experimental details are given in the SI.

Near-field ptychographic X-ray computed tomography (PXCT)

The paste employed for the in situ nanoimaging study was PC-52.5 with a nominal w/c ratio of 0.50 and 0.43 wt% of PCE. The suspension was mixed with a mechanical stirrer at 800 rpm for 3.5 min and then introduced in a glass capillary of 200 μm of nominal diameter. Near-field PXCT data were taken at the cSAXS beamline of the Swiss Light Source (SLS) at the Paul Scherrer Institute (PSI), Villigen, Switzerland. Near-field ptychography[47] is a variant of X-ray ptychography[42,44] in which the sample is scanned across a coherent divergent illumination and magnified images of the sample are recorded on the detector at each scanning position. Ptychographic phase retrieval algorithms are employed to reconstruct the complex transmission function of the specimen, with both absorption and phase, at each angular projection. We then repeat measurements of many projections at different incident angles of the X-rays onto the sample and combine them using standard tomographic reconstruction methods to obtain 3D maps of the electron density and the absorption coefficient of the specimen. In near-field ptychography, if a sufficient number of projections are recorded, the spatial resolution is limited by the magnified pixel size, which is determined by the pixel size of the detector, the distance between the sample and the detector, the divergence of the illumination and the position of the specimen from the point source of the beam, i.e. the focus. We performed our measurements using a high-stability instrument designed for high-resolution PXCT working in air[71,72] and at the hutch temperature of 25 °C, using a photon energy of

8.93 keV. The thickness of the capillary in the imaged region was 160 μm. Therefore, it was scanned with a FOV of 186 μm in order to have more than 10 μm of air outside the capillary, which is required for quantitative phase imaging. The total time to record a full tomogram was between 3 and 4 h, including dead time during the motion of stages in between acquisitions. The voxel size was 186.64 nm. Further experimental details are given in the SI.

Tomographic data analysis

A supervised Machine-Learning (ML) image analysis approach was used to segment the different components of imaged samples, using the IPSDK Explorer software (version 3.2.0.0 for Windows™, Reactiv'IP, Grenoble, France). The plot profiles along the scans electron density/grey value slices and the 3D rendering visualization were done by using Dragonfly software (version 2022.1 for Windows™, Object Research Systems (ORS) Inc., Montreal, Canada). More information about data analysis can be found in the SI.

Data availability

The twelve reconstructed tomograms 'raw' data in tiff format, and the laboratory characterisation data, have been deposited and they can be freely accessed on Zenodo at https://doi.org/10.5281/zenodo.7030107, and used under the Creative Commons Attribution license.

References

1. Habert, G. et al. Environmental impacts and decarbonization strategies in the cement and concrete industries. *Nat. Rev. Earth Environ.* **1**, 559–573 (2020).
2. Monteiro, P. J. M., Miller, S. A. & Horvath, A. Towards sustainable concrete. *Nat. Mater.* **16**, 698–699 (2017).
3. Scrivener, K. L., Ouzia, A., Juilland, P. & Kunhi Mohamed, A. Advances in understanding cement hydration mechanisms. *Cem. Concr. Res.* **124**, 105823 (2019).
4. Ioannidou, K. et al. The crucial effect of early-stage gelation on the mechanical properties of cement hydrates. *Nat. Commun.* **7**, 12106 (2016).
5. Juilland, P., Gallucci, E., Flatt, R. & Scrivener, K. L. Dissolution theory applied to the induction period in alite hydration. *Cem. Concr. Res.* **40**, 831–844 (2010).
6. Ouzia, A. & Scrivener, K. L. The needle model: A new model for the main hydration peak of alite. *Cem. Concr. Res.* **115**, 339–360 (2019).
7. Neubauer, J. et al. Evolution of the particle size distribution of tricalcium silicate during hydration by synchrotron X-ray nanotomography. *Cem. Concr. Res.* **156**, 106769 (2022).
8. Masoero, E., Thomas, J. J. & Jennings, H. M. A reaction zone hypothesis for the effects of particle size and water-to-cement ratio on the early hydration kinetics of C3S. *J. Am. Ceram. Soc.* **97**, 967–975 (2014).
9. Shen, D., Wang, X. & Wu, S. Determining hydration mechanisms for initial fall and main hydration peak in tricalcium silicate hydration using a two-scale hydration simulation model. *Cem. Concr. Res.* **156**, 106763 (2022).
10. Pustovgar, E. et al. Understanding silicate hydration from quantitative analyses of hydrating tricalcium silicates. *Nat. Commun.* **7**, 10952 (2016).
11. Cuesta, A. et al. Multiscale understanding of tricalcium silicate hydration reactions. *Sci. Rep.* **8**, 8544 (2018).
12. Allen, A. J., Thomas, J. J. & Jennings, H. M. Composition and density of nanoscale calcium–silicate–hydrate in cement. *Nat. Mater.* **6**, 311–316 (2007).
13. Juilland, P., Nicoleau, L., Arvidson, R. S. & Gallucci, E. Advances in dissolution understanding and their implications for cement hydration. *RILEM Tech. Lett.* **2**, 90–98 (2017).
14. Kjellsen, K. O. & Lagerblad, B. Microstructure of tricalcium silicate and Portland cement systems at middle periods of hydration-development of Hadley grains. *Cem. Concr. Res.* **37**, 13–20 (2007).
15. Gallucci, E., Mathur, P. & Scrivener, K. Microstructural development of early age hydration shells around cement grains. *Cem. Concr. Res.* **40**, 4–13 (2010).
16. de Matos, P. R. et al. In-situ laboratory X-ray diffraction applied to assess cement hydration. *Cem. Concr. Res.* 106988 https://doi.org/10.1016/j.cemconres.2022.106988 (2022).
17. Aranda, M. A. G. Recent studies of cements and concretes by synchrotron radiation crystallographic and cognate methods. *Crystallogr. Rev.* **22**, 150–196 (2016).
18. Lewis, J. A. et al. Linking void and interphase evolution to electrochemistry in solid-state batteries using operando X-ray tomography. *Nat. Mater.* **20**, 503–510 (2021).
19. Zhang, X. et al. In situ imaging of amorphous intermediates during brucite carbonation in supercritical CO2. *Nat. Mater.* **21**, 345–CO351 (2022).
20. Bullard, J. W. et al. Measurement and modeling needs for microstructure and reactivity of next-generation concrete binders. *Cem. Concr. Compos.* **101**, 24–31 (2019).
21. Monteiro, P. J. M. et al. Advances in characterizing and understanding the microstructure of cementitious materials. *Cem. Concr. Res.* **124**, 105806 (2019).
22. Withers, P. J. et al. X-ray computed tomography. *Nat. Rev. Methods Prim. 2021 11* **1**, 1–21 (2021).
23. Brisard, S., Serdar, M. & Monteiro, P. J. M. Multiscale X-ray tomography of cementitious materials: A review. *Cem. Concr. Res.* **128**, 105824 (2020).
24. Gallucci, E., Scrivener, K. L., Groso, A., Stampanoni, M. & Margaritondo, G. 3D experimental investigation of the microstructure of cement pastes using synchrotron X-ray microtomography (μCT). *Cem. Concr. Res.* **37**, 360–368 (2007).
25. Gastaldi, D. et al. In situ tomographic investigation on the early hydration behaviors of cementing systems. *Constr. Build. Mater.* **29**, 284–290 (2012).
26. Parisatto, M. et al. Examining microstructural evolution of Portland cements by in-situ synchrotron micro-tomography. *J. Mater. Sci.* **50**, 1805–1817 (2015).
27. Hu, Q. et al. Direct measurements of 3d structure, chemistry and mass density during the induction period of C3s hydration. *Cem. Concr. Res.* **89**, 14–26 (2016).
28. Hu, Q. et al. Direct three-dimensional observation of the microstructure and chemistry of C3S hydration. *Cem. Concr. Res.* **88**, 157–169 (2016).
29. Bae, S. et al. In situ soft X-ray spectromicroscopy of early tricalcium silicate hydration. *Mater. (Basel).* **9**, 1–16 (2016).
30. Prade, F. et al. Time resolved X-ray Dark-Field Tomography Revealing Water Transport in a Fresh Cement Sample. *Sci. Rep.* **6**, 29108 (2016).
31. Moradian, M. et al. Direct observation of void evolution during cement hydration. *Mater. Des.* **136**, 137–149 (2017).
32. Geng, G. et al. Synchrotron X-ray nanotomographic and spectromicroscopic study of the tricalcium aluminate hydration in the presence of gypsum. *Cem. Concr. Res.* **111**, 130–137 (2018).
33. Moradian, M. et al. Multi-scale observations of structure and chemical composition changes of portland cement systems during hydration. *Constr. Build. Mater.* **212**, 486–499 (2019).
34. Vigor, J. E., Bernal, S. A., Xiao, X. & Provis, J. L. Automated correction for the movement of suspended particulate in microtomographic data. *Chem. Eng. Sci.* **223**, 115736 (2020).
35. Vigor, J. E., Bernal, S. A., Xiao, X. & Provis, J. L. Time-resolved 3D characterisation of early-age microstructural development of Portland cement. *J. Mater. Sci.* **57**, 4952–4969 (2022).

36. Seiller, J. et al. 4D in situ monitoring of the setting of α plaster using synchrotron X-ray tomography with high spatial and temporal resolution. *Constr. Build. Mater.* **304**, 124632 (2021).
37. Cheikh Sleiman, H., Tengattini, A., Briffaut, M. & Huet, B. & Dal Pont, S. Simultaneous x-ray and neutron 4D tomographic study of drying-driven hydro-mechanical behavior of cement-based materials at moderate temperatures. *Cem. Concr. Res.* **147**, 106503 (2021).
38. Li, X. et al. Direct observation of C3S particle dissolution using fast nano X-ray computed tomography. *Cem. Concr. Res.* **166**, 107097 (2023).
39. Li, X., Hu, Q., Robertson, B., Tyler Ley, M. & Xiao, X. Direct observation of C3S particles greater than 10 μm during early hydration. *Constr. Build. Mater.* **369**, 130548 (2023).
40. Poirier, M. et al. Synchrotron X-ray micro-tomography investigation of the early hydration of blended cements: A case study on CaCl2-accelerated slag-based blended cements. *Constr. Build. Mater.* **321**, 126412 (2022).
41. Dierolf, M. et al. Ptychographic X-ray computed tomography at the nanoscale. *Nature* **467**, 436–439 (2010).
42. Pfeiffer, F. X-ray ptychography. *Nat. Photonics* **12**, 9–17 (2018).
43. Miao, J., Ishikawa, T., Robinson, I. K. & Murnane, M. M. Beyond crystallography: diffractive imaging using coherent x-ray light sources. *Science* **348**, 530–535 (2015).
44. Guizar-Sicairos, M. & Thibault, P. Ptychography: A solution to the phase problem. *Phys. Today* **74**, 42 (2021).
45. Cuesta, A. et al. Chemistry and Mass Density of Aluminum Hydroxide Gel in Eco-Cements by Ptychographic X-ray Computed Tomography. *J. Phys. Chem. C.* **121**, 3044–3054 (2017).
46. Cuesta, A. et al. Quantitative disentanglement of nanocrystalline phases in cement pastes by synchrotron ptychographic X-ray tomography. *IUCrJ* **6**, 473–491 (2019).
47. Stockmar, M. et al. Near-field ptychography: phase retrieval for inline holography using a structured illumination. *Sci. Rep.* **3**, 1927 (2013).
48. Linderoth, O., Wadsö, L. & Jansen, D. Long-term cement hydration studies with isothermal calorimetry. *Cem. Concr. Res.* **141**, 106344 (2021).
49. Taylor, H. F. W. *Cement chemistry*. (Thomas Telford Pub, 1997).
50. Scrivener, K. L., Juilland, P. & Monteiro, P. J. M. Advances in understanding hydration of Portland cement. *Cem. Concr. Res.* **78**, 38–56 (2015).
51. Paganin, D., Mayo, S. C., Gureyev, T. E., Miller, P. R. & Wilkins, S. W. Simultaneous phase and amplitude extraction from a single defocused image of a homogeneous object. *J. Microsc.* **206**, 33–40 (2002).
52. Donnelly, C. et al. Time-resolved imaging of three-dimensional nanoscale magnetization dynamics. *Nat. Nanotechnol.* **15**, 356–360 (2020).
53. van Heel, M. & Schatz, M. Fourier shell correlation threshold criteria. *J. Struct. Biol.* **151**, 250–262 (2005).
54. Diaz, A. et al. Quantitative x-ray phase nanotomography. *Phys. Rev. B* **85**, 020104 (2012).
55. Tang, S. et al. Structure, fractality, mechanics and durability of calcium silicate hydrates. *Fractal Fract.* **5**, 47 (2021).
56. Cuesta, A. et al. Local structure and Ca/Si ratio in C-S-H gels from hydration of blends of tricalcium silicate and silica fume. *Cem. Concr. Res.* **143**, 106405 (2021).
57. Zhu, X. & Richardson, I. G. Morphology-structural change of C-A-S-H gel in blended cements. *Cem. Concr. Res.* **168**, 107156 (2023).
58. Duque-Redondo, E., Bonnaud, P. A. & Manzano, H. A comprehensive review of C-S-H empirical and computational models, their applications, and practical aspects. *Cem. Concr. Res.* **156**, 106784 (2022).
59. Bellmann, F., Sowoidnich, T., Ludwig, H. & Damidot, D. Cement and Concrete Research Dissolution rates during the early hydration of tricalcium silicate. *Cem. Concr. Res.* **72**, 108–116 (2015).
60. Scherer, G. W., Zhang, J. & Thomas, J. J. Nucleation and growth models for hydration of cement. *Cem. Concr. Res.* **42**, 982–993 (2012).
61. Diamond, S. The microstructure of cement paste and concrete–a visual primer. *Cem. Concr. Compos.* **26**, 919–933 (2004).
62. Kjellsen, K. O. & Justnes, H. Revisiting the microstructure of hydrated tricalcium silicate—A comparison to Portland cement. *Cem. Concr. Compos.* **26**, 947–956 (2004).
63. Li, X. & Scrivener, K. L. Cement and Concrete Research Impact of ZnO on C 3 S hydration and C-S-H morphology at early ages. *Cem. Concr. Res.* **154**, 106734 (2022).
64. Xu, Z. et al. Research on cement hydration and hardening with different alkanolamines. *Constr. Build. Mater.* **141**, 296–306 (2017).
65. Lavrov, A., Panduro, E. A. C. & Torsæter, M. Synchrotron Study of Cement Hydration: Towards Computed Tomography Analysis of Interfacial Transition Zone. *Energy Procedia* **114**, 5109–5117 (2017).
66. Da Silva, J. C. et al. Mass Density and Water Content of Saturated Never-Dried Calcium Silicate Hydrates. *Langmuir* **31**, 3779–3783 (2015).
67. Gao, Z. et al. Sparse ab initio x-ray transmission spectrotomography for nanoscopic compositional analysis of functional materials. *Sci. Adv.* **7**, eabf6971 (2021).
68. Hendriksen, A. A. et al. Deep denoising for multi-dimensional synchrotron X-ray tomography without high-quality reference data. *Sci. Rep.* **11**, 11895 (2021).
69. Bouniol, P. & Aspart, A. Disappearance of oxygen in concrete under irradiation: the role of peroxides in radiolysis. *Cem. Concr. Res.* **28**, 1669–1681 (1998).
70. Morales-Cantero, A. et al. C-S-H seeding activation of Portland and Belite Cements: an enlightening in situ synchrotron powder diffraction study. *Cem. Concr. Res.* **161**, 106946 (2022).
71. Holler, M. et al. An instrument for 3D x-ray nano-imaging. *Rev. Sci. Instrum.* **83**, 073703 (2012).
72. Holler, M. et al. X-ray ptychographic computed tomography at 16 nm isotropic 3D resolution. *Sci. Rep.* **4**, 3857 (2014).

Acknowledgements

Financial support from PID2019-104378RJ-I00 research grant, which is co-funded by FEDER, is gratefully acknowledged. SLS is thanked for granting beamtime at cSAXS under proposal 20210147. ESRF is thanked for beamtime at ID19. ToScA (United Kingdom) is gratefully acknowledged for awarding Jim Elliott Award to Shiva Shirani, which supported her stay at ESRF. Dr. Manuel Guizar-Sicairos is thanked for his assistance with the ptychography data processing. I.R.S. is thankful for funding from PTA2019-017513–I.

Author contributions

M.A.G.A. conceived, designed and supervised this study. S.S. and I.S. did initial rheological and laboratory-tomographic studies to fill the 200-micron capillaries. S.S. and A.M.-C. carried out the laboratory characterization. M.A.G.A., S.S., A.C., A.D, P.T., M.H. applied for beamtime at the SLS and designed the PXCT experiment. S.S., A.D., P.T. and M.H. carried out the synchrotron ptychographic experiment. S.S., B.L. and A.R. conducted the synchrotron microtomographic experiment. I.R.S. did the laboratory diffraction and microtomographic experiments. S.S. did all the X-ray imaging data analysis with assistance of M.A.G.A., A.D. and A.C. The machine learning segmentation was carried out by S.S. under E.B.'s supervision. M.A.G.A. wrote the first draft. S.S. prepared all the figures, with help of A.C. for bivariate and Rietveld plots. All authors discussed the results and commented on the manuscript.

Competing interests
The authors declare no competing interests.

Additional information
Supplementary information The online version contains supplementary material available at https://doi.org/10.1038/s41467-023-38380-1.

Correspondence and requests for materials should be addressed to Miguel A. G. Aranda.

Peer review information *Nature Communications* thanks the anonymous reviewer(s) for their contribution to the peer review of this work. A peer review file is available.

Supplementary Information

4D nanoimaging of early age cement hydration

Shiva Shirani[1], Ana Cuesta[1], Alejandro Morales-Cantero[1], Isabel Santacruz[1], Ana Diaz[2], Pavel Trtik[3], Mirko Holler[2], Alexander Rack[4], Bratislav Lukic[4], Emmanuel Brun[5], Inés R. Salcedo[6] and Miguel A. G. Aranda[1]*

[1]Departamento de Química Inorgánica, Cristalografía y Mineralogía, Universidad de Málaga, 29071 Málaga, Spain.
[2]Laboratory for Macromolecules and Bioimaging, Paul Scherrer Institut, 5232 Villigen PSI, Switzerland.
[3]Laboratory for Neutron Scattering and Imaging, Paul Scherrer Institut, 5232 Villigen PSI, Switzerland.
[4]ESRF-The European Synchrotron, 71 Rue des Martyrs, 38000 Grenoble, France.
[5]Université Grenoble Alpes, Inserm UA7 STROBE, 38000 Grenoble, France.
[6]Servicios Centrales de Apoyo a la Investigación, Universidad de Málaga, 29071 Málaga, Spain.

*Corresponding author: g_aranda@uma.es

In the format provided by the authors and unedited

Table of contents:

- **Supplementary Methods**

Synchrotron X-ray computed microtomography experiment (Syn-μCT).

Microtomographic scans were acquired at the 150 m-long beamline ID19 of the European Synchrotron (ESRF) in Grenoble, France. A so-called single-harmonic undulator (type: u17.6, gap 16.5 mm) was chosen as a source due to its excellent photon flux density at a narrow bandwidth around approximately 19 keV photon energy. The u17.6 allows beamline ID19 to be operated only with the two mandatory windows (0.8 mm diamond in the front-end and 0.5 mm Beryllium in the experimental hutch) and an 0.7 mm-thick Aluminium attenuator and hence, guaranties a homogeneous wave front: which is suited for high-sensitivity measurements by means of inline propagation-based phase contrast. The propagation distance between sample and detector was set to 15 mm. The indirect high-resolution detector consisted of a so-called revolver-microscope by the French company OptiquePeter (Lentilly, France)[1], the system lens-couples an 8.7 μm-thin LSO:Tb (Tb-doped Lu_2SiO_5) single-crystal scintillator with a 10× Olympus microscope (0.3NA) to a sCMOS-based camera (type: pco.edge, PCO AG, Germany)[2]. The effective pixel size of the detector assembly is approximately 0.6 μm. 6000 projection angles were acquired over a 360 degree tomographic scan with an exposure time of 0.05 s, i.e. 5 minutes scan, at ~21.5 °C. During this experiment, the ESRF operated in so-called 4bunch timing mode with a reduced ring current of maximum 20 mA. The estimated flux density at the sample position was 4.2×10^{11} photons·s^{-1}·mm^{-2}. Phase retrieval of the projections was performed using the Paganin algorithm[3], considering the ratio of the refractive and absorption index δ/β equal to 70. In order to retrieve the microstructural content introduced by the inherent smoothing characteristics of the phase retrieval method, a Gaussian unsharp mask was applied. The voxel size with the employed configuration, to fully image a capillary of 0.7 mm of diameter, was 0.65 μm.

The tomographic reconstructions were performed using the open-source tomography software available at the ESRF, relying on the sub-packages NXtomoMill and NABU[4]. Given its straightforward Graphics Processing Unit (GPU)-based implementation, the full volume reconstructions were performed on the Power9 cluster using the gold-standard filtered back projection (FBP) algorithm. The projections are first corrected for beam profile illumination (flat field), dark current noise of the detector (dark field) and filtered for any potential pixel outliers arising from stray photons. The reconstructed volume, consisting of 2490×2490×1950 pixels, is cast to 16 bit format considering the 10-90% of the volume histogram and cropped to the region of interest. In the case of the reconstructions used for the Fourier Shell Correlation (FSC) analysis,[5] the original reconstruction is split into two sub-sampled reconstructions considering the number of the reconstructed either even or odd projections.

Near-field ptychographic X-ray computed tomography (PXCT).

The measurements were carried out with a high-stability instrument designed for high-resolution PXCT working in air and at room temperature[6,7], using a photon energy of 8.93 keV. The coherent illumination was defined with a Fresnel zone plate (FZP) of 120 μm diameter and 60 nm outer-most-zone width, which at this energy had a focal distance of 51.9 mm. The FZP had locally displaced zones, specifically designed to produce an optimal illumination for ptychograph[8]. The flux of the X-ray beam was 1.7×10^{8} photons·s^{-1} at the sample position. The sample was placed at 13 mm downstream the focus, where the illumination had a size of about 30 μm. Ptychographic scans were recorded following the positions of a Fermat spiral[9] with an average step size of 6 or 7 μm and a field of view of 186 μm × 30 μm (horizontal × vertical). The field of view must be larger than the size of the capillary to include an air region at both sides of the sample, which is needed for successful tomographic reconstructions and for quantitative contrast. At each scanning position, magnified images of the sample were recorded with an in-vacuum Eiger 1.5M detector[10] with a pixel size of 75 μm placed at 5.237 m downstream the sample, with an acquisition time of 0.1 s. A scan speed of ~5 Hz was achieved thanks to a combined motion of the FZP and the sample, while achieving an effective static illumination on the sample during acquisition[11]. Near-field ptychographic scans were repeated at 420 rotation angles of the sample in equal intervals from 0 to 180 deg. We recorded a total of 3 tomograms at different times from the start of the cement hydration at ~25 °C, the temperature of the

experimental hutch. The first tomogram was recorded with an average scanning step size of 6 μm, it started at 17 h and finished at 20h and 55 minutes, after water mixing, i.e. 3h 55 min of total acquisition time. This scan is hereafter labelled 19 h dataset. The other two tomograms were recorded with a step size of 7 μm lasting 3h 6 min. The scans labelled 47 and 93 h started at 46 and 92 h (after water mixing), respectively. The scan times include the dead time during motion of stages in between acquisitions. The dose absorbed by the specimen during data acquisition was estimated to be 0.7 and 0.5 MGy for the tomograms with 6 and 7 μm of step size, respectively.

Near-field ptychographic reconstructions were performed for each projection using the Ptycho Shelves package[12] developed by the Coherent X-ray Scattering group at PSI, using 5000 iterations of a difference map algorithm[13] adapted for near-field geometry. The pixel size of the images, determined by geometric magnification, is 186.64 nm and we estimate by Fourier ring correlation[5] that the 2D resolution of each reconstructed image is about 200 nm. For each tomographic dataset, projections were aligned with sub-pixel accuracy and processed for phase tomographic reconstruction from phase projections as previously reported[14,15]. The 3D spatial resolution was estimated by FSC[5]. The resolution obtained, see subsection dedicated to the spatial resolution, was limited by the number of projections, which was chosen to have reasonable scan times.

PXCT provides 3D maps of the electron density of the specimen with quantitative contrast, the sensitivity being about 0.02 $e^{-}Å^{-3}$.[16] For attaining quantitative electron densities, the entire specimen must be included in the field of view, containing some empty space around it, which was the case in our measurements. Therefore, it is possible to easily distinguish air and water regions in the specimen, which have electron densities of 0.00 and 0.33 $e^{-}Å^{-3}$, respectively. Obviously, neutron imaging is the standard technique to disentangle water from air porosities.[17] A key advantage of neutron imaging is its ability to can scan large volumes. However, it must also be noted that at inferior spatial resolution compared to PXCT.

Tomographic data analysis.

Initially, the re-alignment of the data, when needed must be detailed.

For the PXCT, the capillary position was very accurate, as the capillary/holder system was mounted from the tray storage to the sample stage by the flOMNY gripper (robot). Hence, the angular orientation of the sample was maintained. The field of view of the sample was aligned carefully based on features visible in the 2D projections. The scanned regions with time were consistent within a few voxels and therefore no alignment between different acquisitions was required.

For the Syn-μCT, a mark was drawn on the sample holder and sample stage for the incident beam to minimise the initial incidence angular position variability. Before each scan, a projection was acquired as a reference for the next one in order to scan the same region. A minor manual registration was required, mostly rotations around x- and y-axes.

For the Lab-μCT, manual registration was required to align the different acquisitions. The process is described next. The capillary was considered as a cylinder and we manually made the cylinders vertical and centred in the reconstructed volume. The remaining rotation around the z-axis was visually done by superimposing distinguishable landmarks in the corresponding images.

The segmentation was done on a Volume of Interest (VOI) corresponding to the inner part of the capillaries for each imaged sample. The total volume of these VOIs varies depending on the sample sizes, amounting to $\sim 1\times10^{5}$ μm^3 for each PXCT dataset and $\sim 1\times10^{8}$ μm^3 for Syn-μCT and Lab-μCT samples. A supervised Machine-Learning (ML) image analysis approach was used to segment the different components of the scanned samples, using the IPSDK Explorer software (version 3.2.0.0 for Windows™, Reactiv'IP, Grenoble, France). This software allows us to manually label voxels on a selected training dataset (approximately 31 voxels for each component on average for PXCT, 20 voxels on average for Syn-μCT and Lab-μCT) and to rapidly obtain test results to determine if the labelling is sufficient or if it requires more information/re-training. The initial classification was based on the electron densities with a variation of ~5% of the measured values, from selected volumes, which are given in Table S7. These test results are obtained after

a first learning step using a random forest method. It is also possible for the user to keep or remove features used in the random forest decision trees based on their relevance. This method permitted to segment the components with comparable grey values and/or electron densities, overlaid ML models on raw datasets are shown in Fig. 7.

On the one hand, the good contrast and the high spatial resolution in PXCT allowed to classify the components into seven categories. They are given next from higher to lower electron densities: i) C_4AF (yellow) with highest values; ii) $C_3S/C_2S/C_3A$ (dark brown) which are the clinker particles; iii) calcite (pink); iv) portlandite (green); v) the rest of the hydrated phases with lower electron densities were labelled as 'Low-Density Hydrates' (light brown), i.e. C-S-H gel, iron-silicon-hydrogarnet, hemicarbonate and ettringite; vi) water porosity (blue); and vii) air porosity (black). On the other hand, due to the contrast and spatial resolution limitations in the two other modalities, Syn-μCT and Lab-μCT, the components were classified into four categories. The classification from higher to lower grey-values was: i) clinker particles (dark brown), i.e. $C_4AF/C_3S/C_2S/C_3A$; ii) a component labelled 'High-Density Hydrates' (green), being mainly portlandite and calcite; iii) another component labelled 'Low-Density Hydrates' (light brown), being mainly C-S-H gel, iron-silicon-hydrogarnet, hemicarbonate and ettringite; and iv) porosity (black) which contain both water and air. It is noted that Syn-μCT and Lab-μCT microtomographies do not allow to distinguish water from air porosities due to the similarities in their X-ray attenuation values.

This ML approach also permits to mitigate the influence of partial volume effects in-between labelled components for accurate quantitative analysis of PXCT, i.e. mean electron density. Selected results after the PXCT segmentation procedure are summarised SI. Movie 1. In addition, after grains were segmented using the ML approach described above, the C-S-H gel shell thickness was computed on PXCT imaged sample at 19 h, see Fig. 6 and SI. Movie 2. The wall thickness script computes the object thickness. For a given pixel, the thickness is the radius of the largest circle centred on this pixel entirely included in the object. The steps of the data analysis process are shown in flowcharts, see Fig. S20 and S21. A further post-segmentation data analysis calculation was carried out in order to show the particle size distribution evolution with hydration time. The anhydrous cement particles, at the three hydration times, were classified by computing their mean Feret diameters. Fig. 8b displays the volume percentage of the segmented grains (and their cumulative volumes) as function of the particle sizes that can be compared with the initial characterization by laser diffraction, see Fig. 1a. 3D rendering visualization was done using Dragonfly software (version 2022.1 for Windows™, Object Research Systems (ORS) Inc., Montreal, Canada).

Spatial resolution analysis.

The spatial resolution was characterised by two approaches as recently reported[18]. On the one hand, it can be determined from the grey-value changes in line profiles through the edge sharpness of the interfaces. A point spread function (PSF) used to determine the spatial resolution of the images as ISO/TS 24597 defines the Gaussian radius of the PSF as the resolution, which equals to a change between 25 %–75 % grey value along the studied interfaces.[19] Here, a common interface present in the three imaging modalities has been selected for the line profiles: the glass capillary wall – air (i.e. exterior of the capillaries). We have measured 25 interfaces in every tomogram, which allowed us to determine the average spatial resolution and its associated standard deviation. Moreover, as examples, Figures S2-S4 display line profiles of sharp interfaces between high (i.e. alite) and low density (i.e. porosity) components within the capillaries. The spatial resolutions, as determined by this approach, were 250(25) nm, 264(25) nm, 272(34) nm, 748(19) nm and 2.21(17) μm, for PXCT-19h, PXCT-47h, PXCT-93h, Syn-μCT and Lab-μCT datasets, respectively.

On the other hand, FSC plots[5] have been also computed. The traces are displayed in Figures S5-S7 giving spatial resolution values of 430 nm, 470 nm, 500 nm, 650 nm and 1.9 μm, for PXCT-19h, PXCT-47h, PXCT-93h, Syn-μCT and Lab-μCT datasets, respectively. Moreover, the FSC trace for PXCT-19h shows a smooth decrease in the 0.0-0.2 spatial frequency range, which is likely due to the hydration of cement during the 4-hour measurement. As expected, this behaviour is not shown at later ages.

It should be noted that the agreement between the spatial resolution results between the edge sharpness approach and FSC method is satisfactory for Syn-μCT (750 vs. 650 nm) and Lab-μCT (2.2 vs.1.9 μm) datasets.

However, the agreement between these two approaches is not good for PXCT (for instance, 250 vs 430 nm at 19 h). The poorer resolution estimated by FSC can be explained because the angular sampling is very tight, i.e. 420 projections, so the two employed subtomograms in the FSC, each of 210 projections, were significantly undersampled compared to the number of voxels across the diameter of the sample. This means that the correlation between two such undersampled tomograms can give a low estimation of the spatial resolution. This feature is not observed for Syn-μCT and Lab-μCT as the total number of projections were 6000 and 1637, respectively. In other words, the subtomograms with half the number of projections were not undersampled for these two imaging modalities.

Etch-pit growth rate evaluation.

The estimation of the etch-pit growth rate was based on the analysis of 27 etch-pits from 5 different large alite grains. It is noted that the etch-pits have irregular 3D shapes and therefore, for its spatial dissolution rate estimation, some simplifications were undertaken. Moreover, the spatial resolution of this PXCT work, ~250 nm, is limited for accurate analyses. Therefore, we consider this approach as an estimation. Firstly, etch-pits were visually selected from grains with sizes larger than 10 μm. Secondly, their overall shapes were compared in two hydrating steps. Then, two envelopes from pixels with at least 90% of the electron density of alite were developed. The estimated/calculated distance (in pixels) was computed between these edges for the deepest perpendicular length. These values were converted to dissolution rate by taking the ratio respect to the time between measurements. The result for the analysis between 19 and 47 h datasets gave 6.1 pixels of average distance which is equivalent to 41(29) nm/h. There was large variability in the rates, the fastest being 110 nm/h and the slowest being 10 nm/h. From this investigation, it is not possible to know if this large variability comes from the heterogeneity in the defects within these regions, or if other variables like the spatial resolution of this work and the local water-to-cement ratio variations are also playing important roles. More imaging studies are necessary to establish this. The very same 27 etch-pits were also analysed between 47 and 93 h datasets. In this case, the etch-pit growth rate was slower 7 nm/h, showing that the water diffusion is already limiting hydration at four days.

Water/cement ratio estimation of the scanned sample by PXCT

The w/c ratios of the scanned capillaries in a selected region can be calculated at the different ages according to the procedure previously reported[20]. The final β-mean values obtained by PXCT were used after converting to μ values, see Table S6. Then, using the mineralogical compositions of the anhydrous cement (given in the Supporting information, Table S2) the μ value is estimated, taking into account the μ value of free water, 22.2 cm^{-1}. For instance, for the 19 h sample, it can be estimated that the paste was composed of 69.9 wt% PC and 30.1 wt% water to account for the overall μ of the paste. This calculation yielded a w/c ratio of 0.39, see Table S6.

Chemical reactions

I. The chemical reactions used for the FW calculation, see Table S5, are: (1) the consumption of water by the hydration of C_4AF, with C_3S which is the source of silicates, to give amorphous iron siliceous hydrogarnet (Fe-Si-Hg) and crystalline portlandite; (2) the hydration of C_3S to yield amorphous C-S-H gel and crystalline portlandite; (3) the hydration of C_3A, consuming a calcium sulfate source, to yield ettringite if there are enough sulfates available (which is the case here); and (4) the possible carbonation of portlandite gives crystalline (and amorphous) calcium carbonate(s) and it releases free (capillary) water.

II. In the absence of belite hydration, the chemical reaction contributing to C-S-H gel formation, see Table S5, is just (2). It is underlined that a small fraction of the consumed alite did not result in C-S-H gel but in the formation of iron siliceous hydrogarnet from the ferrite hydration (reaction 1).

It is noted here that for the calculations presented in Table S5, the amount of C_3S which is needed for the silicate groups in iron-silicon-hydrogarnet, is calculated first from the degree of hydration of C_4AF (applying reaction #1). Then, the portlandite and C-S-H gel contents are determined from the reaction of C_3S after subtracting the number obtained in the process described just above.

$$Ca_4Al_2Fe_2O_{10} + 1.68Ca_3SiO_5 + 11.68H_2O \rightarrow 2Ca_3AlFe(SiO_4)_{0.84}(OH)_{8.64}\,(amorph.) + 3.04Ca(OH)_2 \quad (1)$$

$$Ca_3SiO_5 + 5.2H_2O \rightarrow 1.2Ca(OH)_2 + (CaO)_{1.8}SiO_2(H_2O)_{4.0} \quad (2)$$

$$Ca_3Al_2O_6 + 3CaSO_4{\cdot}2H_2O + 26H_2O \rightarrow Ca_6Al_2(SO_4)_3(OH)_{12}{\cdot}26H_2O \quad (3)$$

$$Ca(OH)_2 + CO_2 \rightarrow CaCO_3 + H_2O \quad (4)$$

Open access raw data availability and description

The following raw data has been openly deposited on Zenodo and can be acceded at: https://doi.org/10.5281/zenodo.7030107

1. Tomographic reconstructed raw data of all the X-ray imaging modalities (twelve tomograms) in 16 bit and .tif format. The size of the files is also given in the following table.

Folder Name	Sub-folders Label	File Size*	Additional Information
Phase-PXCT	1_PXCT-19h 2_PXCT-47h 3_PXCT-93h	736.9MB	4D Synchrotron Ptychographic X-ray Computed Tomography Cement Hydration (Delta Dataset)
Syn-microCT	4_Syn-microCT-19h 5_Syn-microCT-47h 6_Syn-microCT-93h	52.8GB	4D Synchrotron Phase-contrast Microtomography Cement Hydration
Lab-microCT	7_Lab-microCT-19h 8_Lab-microCT-47h 9_Lab-microCT-93h	7.5GB	4D Laboratory Attenuation-contrast Microtomography Cement Hydration
Absorption-PXCT	10_abs-PXCT-19h 11_abs-PXCT-47h 12_abs-PXCT-93h	722.9MB	Absorption Dataset for 4D Synchrotron Ptychographic X-ray Computed Tomography Cement Hydration (Beta Dataset)

Net total size of all datasets: **82.8GB**

**These are zipped files. The original file size for every single 16 bit Syn-microCT dataset is 22.8GB, for each Lab-microCT dataset is 3.0GB and for each PXCT dataset is 500MB.*

2. Laboratory raw data

2.1. Particle size distribution (PSD)

"PSD" labelled folder contains two files in .mmes format.

2.2. Isothermal calorimetry

"Calorimetry" labelled folder contains six files in .xlsx excel format.

2.3) Laboratory X-ray powder diffraction (LXRPD)

"LXRPD" labelled folder contains five files in .ASC text format.

• Supplementary Tables

Table S1. Chemical (elemental) analysis (by X-ray fluorescence) of the two employed Portland cements in this investigation. All data expressed in weight percentages of the corresponding oxides.

	CaO	SiO_2	SO_3	Al_2O_3	Fe_2O_3	MgO	K_2O	Na_2O	Others	LoI
PC-52.5	62.2	20.4	3.6	4.9	3.2	1.5	1.1	0.3	0.5	2.3
PC-42.5	62.9	19.7	3.4	5.0	3.4	1.5	1.1	0.3	0.3	2.7

Table S2. Rietveld quantitative phase analysis of the employed anhydrous Portland cements, in wt%.

	C_3S	β-C_2S	C_4AF	o-C_3A	$C\bar{S}H_2$	$C\bar{S}H_{0.5}$	Cc	Q	$K\bar{S}$	CaO
PC-52.5	61.0	11.8	11.5	8.2	1.9	2.0	2.8	0.8	-	-
PC-42.5	61.6	11.1	10.8	7.8	0.9	2.1	3.7	0.6	1.1	0.4

Table S3. Textural details of the two cements.

	Density (gcm^{-3})	BET (m^2g^{-1})	Blaine (m^2Kg^{-1})	$D_{v,10}$ (µm)	$D_{v,50}$ (µm)	$D_{v,90}$ (µm)
PC-52.5	3.108(1)	2.27(1)	409(8)	1.8	11.5	32.7
PC-42.5	3.126(1)	1.25(1)	368(1)	2.1	18.0	50.0

Table S4. Selected cumulative heat release data (from the isothermal calorimetry study) for the two employed cements. All values in J per gram of Portland cement.

	19 h		47 h		93 h		7 d		Maximum peak		
	Heat/J	DoH$^{\$}$/%	Heat/J	DoH$^{\$}$/%	Heat/J	DoH$^{\$}$/%	Heat/J	DoH$^{\$}$/%	Time/h	Heat/J	DoH$^{\$}$/%
PC-52.5, w/c=0.40	180.8	33.7	279.8	52.4	300.7	56.3	313.5	58.7	14.2	102.9	19.3
PC-52.5, w/c=0.50	157.2	29.4	306.6	57.4	346.9	64.9	365.2	68.4	15.6	102.7	19.2
PC-42.5, w/c=0.40	116.5	22.1	220.5	41.9	270.8	51.5	291.5	55.4	10.4	50.4	9.6
PC-42.5, w/c=0.50	114.4	21.7	223.3	42.4	279.8	53.1	310.0	58.9	11.0	53.4	10.2

$^{\$}$Total heat of hydration of PC52.5 as calculated in ref.[21] option-1: **534 J.**

$^{\$}$Total heat of hydration of PC42.5 as calculated in ref.[21] option-1: **526 J.**

Table S5. Rietveld quantitative phase analysis (of MoKα_1 radiation powder diffraction data) results (wt%) for the studied PC-52.5 pastes, w/c=0.40. Laboratory X-ray diffraction data were taken on the same capillary used for the laboratory, attenuation-contrast, microtomographic study. The data are referenced to 100 grams of paste.

phases	t_0*	t=22h	t=50h	t=96h
C_3S	43.57	18.9	17.0	16.3
β-C_2S	8.43	8.3	8.7	9.1
C_3A	5.86	2.9	1.9	1.5
C_4AF	8.21	7.7	5.8	5.4
Cc#	2.00	3.1	3.2	3.6
CH	-	10.6	13.5	13.8
AFt	-	12.2	12.4	12.4
AFm-Hc	-		0.4	0.4
C-S-H&	-	20.3	20.6	20.9
Fe-Si-Hg&	-	0.5	2.8	3.1
FW&	28.57	14.4	12.9	12.7
DoH C_3S (%)	-	56	61	63
DoH C_2S (%)	-	0	0	0
DoH C_3A (%)	-	50	67	74
DoH C_4AF (%)	-	5	29	34

* This cement also has at t_0: 1.4 wt% of gypsum, 1.4 wt% of bassanite and 0.6 wt% of quartz.
& C-S-H, Fe-Si-Hg and FW (free water) contents calculated from the assumed chemical reactions as described in supplementary methods.
# The calcite content increased from 2.0 wt% at t=0 to 3.6 wt% at 96 h, highlighting a significant carbonation of the paste within this large capillary, i.e. 1 mm of diameter. The thinner capillary used in the PXCT study, i.e. 0.2 mm of diameter, did not show a measurable conversion of CH to Cc, see below. Carbonation of a cement paste has been previously measured by PXCT, when its extension was significant.[22]

Table S6. Experimental mean β values converted to μ values obtained from a VoI in the PXCT study. The calculation of the w/c ratio of this region at the different hydration ages is also included. More details about this calculation is given in the Supplementary Methods.

Scan	Experimental β*	Experimental μ/cm^{-1}	Weight /g		Weight /wt%		w/c ratio
			water	cement	water	cement	
PXCT-19h	1.316×10^{-7}	119.1	55.0	139.4	28.3	71.7	0.39
PXCT-47h	1.265×10^{-7}	114.5	57.2	132.8	30.1	69.9	0.43
PXCT-93h	1.274×10^{-7}	115.3	56.8	133.9	29.8	70.2	0.42

*The β values have been calculated using the same volume used for the calculation of delta but excluding the regions where the electron density is smaller than 0.24 e$^-$Å^3, as they have been considered air porosity. It is noted that air is not included in this calculation.

Table S7. Expected (from the crystallographic data,[23,24]) mass and electron densities. The attenuation length values are calculated[$] for the employed wavelength, E=8.93 keV. The measured electron densities for selected components from the PXCT data, where relatively large volumes could be chosen, are also given.

Cement Phases	Abbrev.	Formula	Mass density /gcm^{-3}	Electron density /e$^-$Å^{-3}	Measured electron density /e$^-$Å^{-3} (within selected particles)[#] 19 h	47 h	93 h	Attenuation length /μm	μ /cm^{-1}	β
#0, air	-	-	~0.00	~0.00			0.00(4)			
#1, water	-	H_2O	1.00	0.33	0.31(1)			1388.6	7.2	7.96 10^{-09}
#2, ettringite	AFt	$Ca_6Al_2(SO_4)_3(OH)_{12}\cdot 26H_2O$	1.78	0.56				154.6	64.7	7.15 10^{-08}
Hemicarbo-aluminate[=]	Hc	$Ca_4Al_2(OH)_{13}(CO_3)_{0.5}\cdot 5.5H_2O$	1.90	0.59				118.6	84.3	9.32 10^{-08}
Monosulfate[=]	AFm-SO_4	$Ca_4Al_2(OH)_{12}(SO_4)\cdot 6H_2O$	2.02	0.63				112.4	89.0	9.83 10^{-08}
#3, calcium silicate hydrate	C-S-H	$(CaO)_{1.8}(SiO_2)(H_2O)_4$	*2.11*[%]	*0.66*[%]				*95.9*	*104.3*	*1.15 10^{-07}*
#4, portlandite	CH	$Ca(OH)_2$	2.23	0.69	0.62(2)	0.649(6)	0.651(5)	61.5	162.6	1.80 10^{-07}
#5, calcium carbonate	Cc	$CaCO_3$	2.71	0.82	0.782(3)	0.776(3)	0.776(3)	66.3	150.8	1.67 10^{-07}
#6, tricalcium aluminate	C_3A	$Ca_3Al_2O_6$	3.05	0.91				49.0	204.0	2.25 10^{-07}
#7, alite	C_3S	Ca_3SiO_5	3.15	0.95	0.936(2)	0.931(2)	0.932(1)	41.8	239.1	2.64 10^{-07}
#8, belite	C_2S	Ca_2SiO_4	3.30	0.99	0.98(2)	0.98(1)	0.98(1)	43.3	231.1	2.55 10^{-07}
#9, ferrite	C_4AF	Ca_2AlFeO_5[&]	3.73	1.10				26.4	379.4	4.19 10^{-07}

[#] Electron densities, from particle picking, were obtained by the average of 10 cubes for the capillary; 5, 4, 5 and 6 grains for portlandite, calcium carbonate, alite and belite, respectively. Moreover, 5 cubes at 19 h gave the reported measured electron density for capillary water. Similarly, 5 cubes at 93 h were computed to obtain the value for air. Finally, the electron density of LDH (low density hydrates) was measured at 93 h in 5 cubes yielding 0.56(1) e$^-$Å^{-3} that it corresponds to ettringite and/or C-S-H as they cannot be distinguished.

[=] The expected values for these phases, i.e. hemicarbo-aluminate and monosulfate, are given for the sake of completeness but they are not numbered as they were not identified in the bivariate plots, see Figures S9.

[%] There are not expected values for an amorphous material. The quoted values (italics) were determined for five months cured C-S-H gel by PXCT[20].

[&] The reported values are for stoichiometric Ca_2AlFeO_5, i.e. an Al/Fe molar ratio of 1.0, which is an approximation as this ratio could be different from 1.0.

[$] The *attenuation length* values have been calculated from[25], https://henke.lbl.gov/optical_constants/atten2.html

The μ values were calculated from: $\mu\ [cm^{-1}] = \frac{1}{Attenuation\ Length\ [\mu m] \times 10^{-4}}$

Finally, β was calculated as $\beta = \frac{\mu\lambda}{4\pi}$

Table S8. Component segmentation (vol%) and average electron densities obtained by PXCT at the different hydration ages; expected electron densities (from crystallographic data when it is possible) are also given for reference.

Component	Expected electron density /$e^-Å^{-3}$	19 h			47 h			93 h		
		Vol /%	Electron density* /$e^-Å^{-3}$	Electron density& /$e^-Å^{-3}$	Vol /%	Electron density* /$e^-Å^{-3}$	Electron density& /$e^-Å^{-3}$	Vol /%	Electron density* /$e^-Å^{-3}$	Electron density& /$e^-Å^{-3}$
Capillary	-	-	-	0.63(1)	-	-	0.63(1)	-	-	0.63(1)
Air porosity	0.00	0.2	0.01(5)	-	4.1	0.10(1)	-	6.7	0.10(1)	-
Water porosity	0.33	15.1	0.33(6)	-	2.2	0.33(5)	-	2.8	0.32(6)	-
LD-Hydrates	*0.38-0.53*	45.5	0.50(4)	-	56.5	0.52(4)	-	51.8	0.53(4)	-
Portlandite	0.69	4.6	0.63(1)	0.62(2)	13.1	0.62(4)	0.65(1)	15.7	0.62(4)	0.65(1)
Calcite	0.82	2.5	0.74(2)	0.78(1)	2.2	0.74(4)	0.78(1)	2.3	0.74(5)	0.78(1)
Belite/Alite/C_3A	0.99/0.95/0.91	30.4	0.90(1)	0.94(1)/0.98(2)	20.3	0.90(4)	0.93(1)/0.98(1)	19.3	0.90(5)	0.93(1)/0.98(1)
Ferrite	1.10	2.1	1.02(2)	-	1.5	1.01(4)	-	1.4	1.02(4)	-

*Electron densities, from full volume, were obtained by segmentation excluding the external voxels to avoid partial volume effect

&Electron densities, from particle picking, were obtained by the average of 10 cubes for the capillary; 5, 4, 5 and 6 grains for portlandite, calcium carbonate, alite and belite, respectively.

Table S9. Volume percentages for the cement pastes at the different ages of hydration determined by the techniques used in this paper. Degrees of hydration are also included.

Technique	Hydration age /h	Porosity /vol%: air & water	LD-hydrates /vol%	Portlandite & calcite /vol %	Anhydrous components /vol %: $C_3S/C_2S/C_3A/C_4AF$	DoH /%
Calorimetry PC-52.5, w/c=0.40	19	-	-	-	-	34
	22	-	-	-	-	39
	47-50	-	-	-	-	53
	93-96	-	-	-	-	56
Calorimetry PC-42.5, w/c=0.50	19	-	-	-	-	22
	47	-	-	-	-	42
	93	-	-	-	-	53
LXRPD PC-52.5, w/c=0.40	0	56.1[$]	-	-	39.9[$]	-
	22	26.4	39.6	11.6	22.0	45
	50	22.3	44.8	13.7	20.6	48
	96	21.9	45.5	14.2	19.9	50
Lab-µCT PC-52.5, w/c=0.40	0	56.1[$]			39.9[$]	-
	19	5.6	35.7	35.7	23.5	41
	47	2.1	21.7	60.8	15.4	61
	93	2.1	20.2	62.8	15.0	62
Syn-µCT PC-42.5, w/c=0.50	0	61.5[#]	-	-	35.0[#]	-
	19	1.9	43.8	27.3	27.0	23
	47	14.5	32.9	31.7	20.8	41
	93	13.7	34.3	35.2	16.9	52
PXCT PC-52.5, w/c=0.40	0	56.1[$]			39.9[$]	-
	19	15.3	45.5	7.1	32.1	20
	47	6.3	56.5	15.3	21.8	45
	93	9.5	51.8	18.0	20.7	48

[$] The amount of water and clinker phases is 96.0 vol%. The remaining 4.0 vol% is due to the minor components: gypsum, bassanite, calcite and quartz

[#] The amount of water and clinker phases is 96.4 vol%. The remaining 3.6 vol% is due to the minor components: gypsum, bassanite, calcite and quartz

• Supplementary Figures

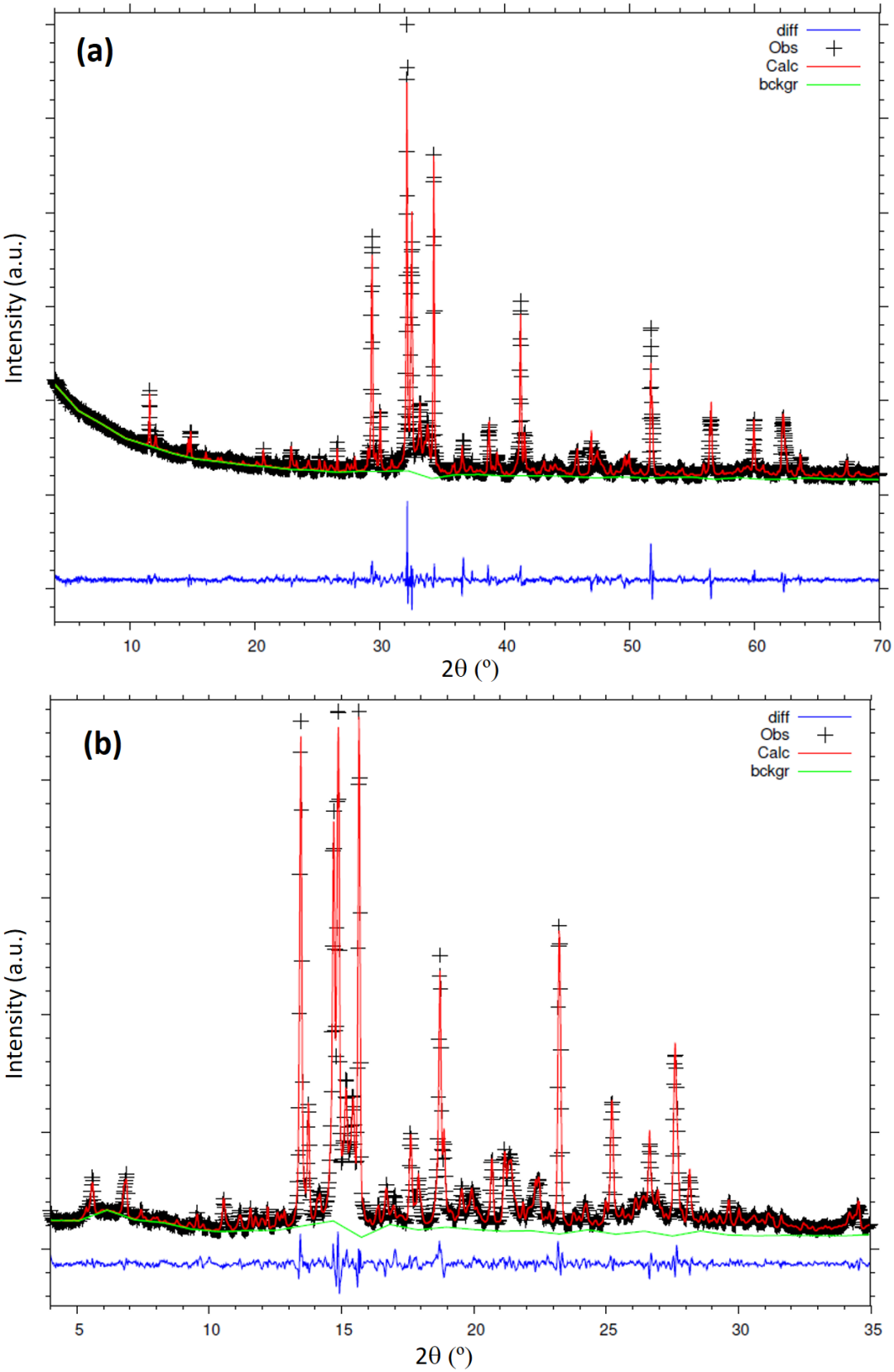

Figure S1. Laboratory Rietveld plots for the anhydrous cements. (a) PC-52.5 (CuKα_1 radiation, λ=1.5416 Å). (b) PC-42.5 (MoKα_1 radiation, λ=0.7093 Å).

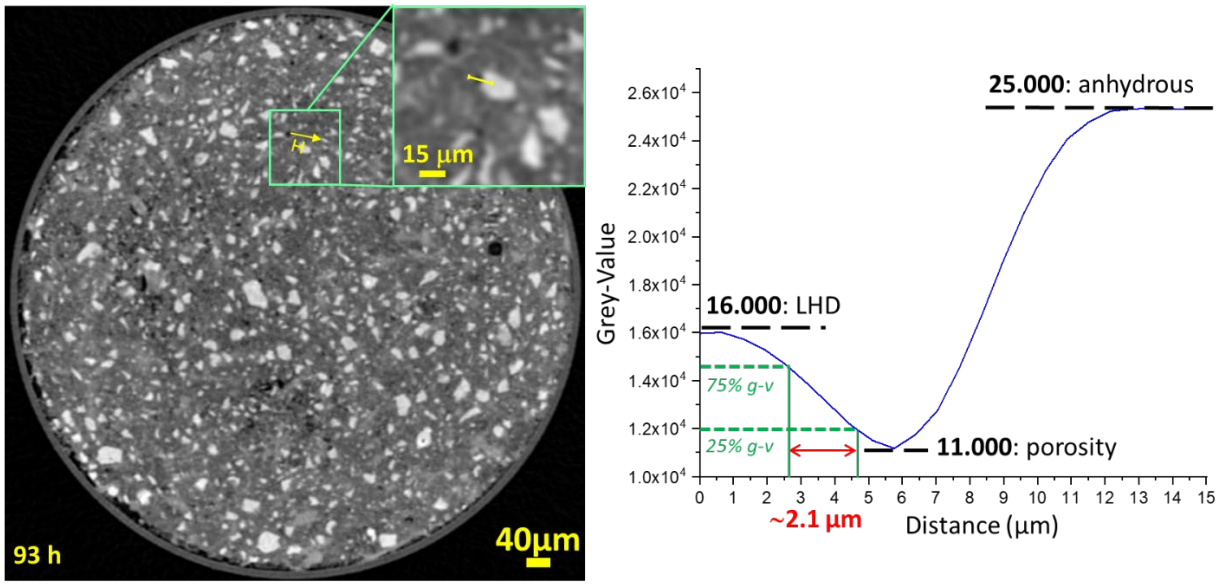

Figure S2. (Left) Selected orthoslice and (Right) grey-value profile of the yellow line (shown in the right panel) including a sharp interface for the laboratory, attenuation-contrast, microtomographic study (PC-52.5 paste with w/c=0.40, dataset at 4 days of hydration). The estimated spatial resolution, from this approach, is ~1.9 µm.

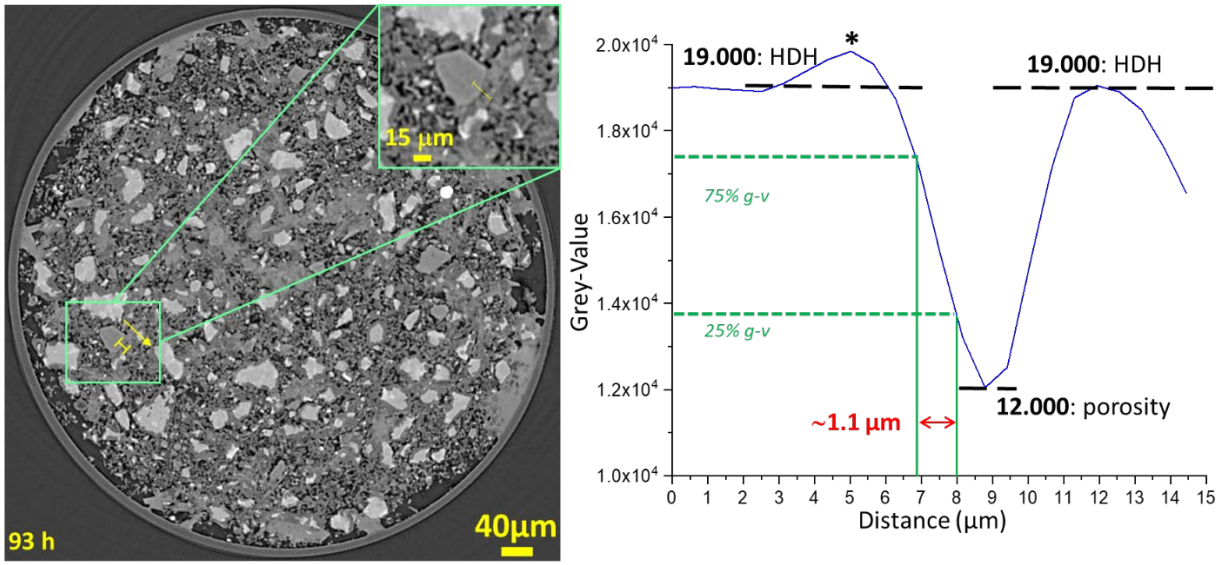

Figure S3. (Left) Selected orthoslice and (Right) grey-value line profile of a sharp interface for the synchrotron, phase propagation based-contrast, microtomographic study (PC-42.5 paste with w/c=0.50, dataset at 4 days of hydration). The estimated spatial resolution, from this approach, is ~ 0.75 µm. The star symbol highlights the small artefact (edge enhancement not fully corrected by the Paganin algorithm) which is commonly observed in in-line propagation-based phase-contrast synchrotron tomography.

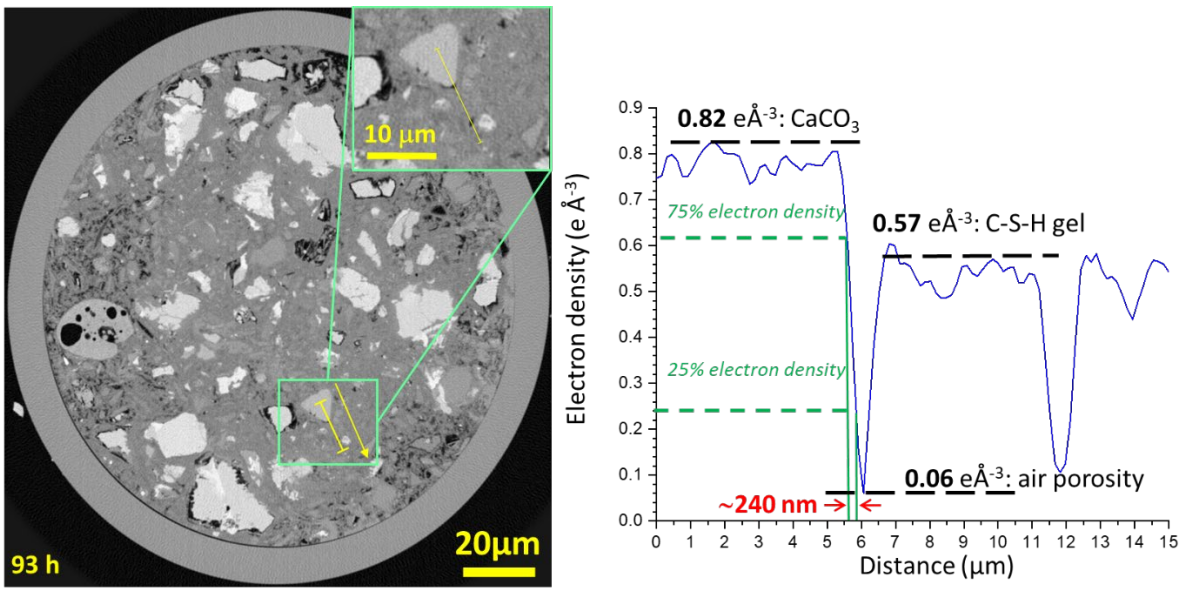

Figure S4. (Left) Selected orthoslice and (Right) line profile of a sharp interface for the near-field ptychographic X-ray computed tomographic study (PC-52.5 paste with w/c=0.40, dataset at 4 days of hydration). The estimated spatial resolution, from this approach, is ~250 nm.

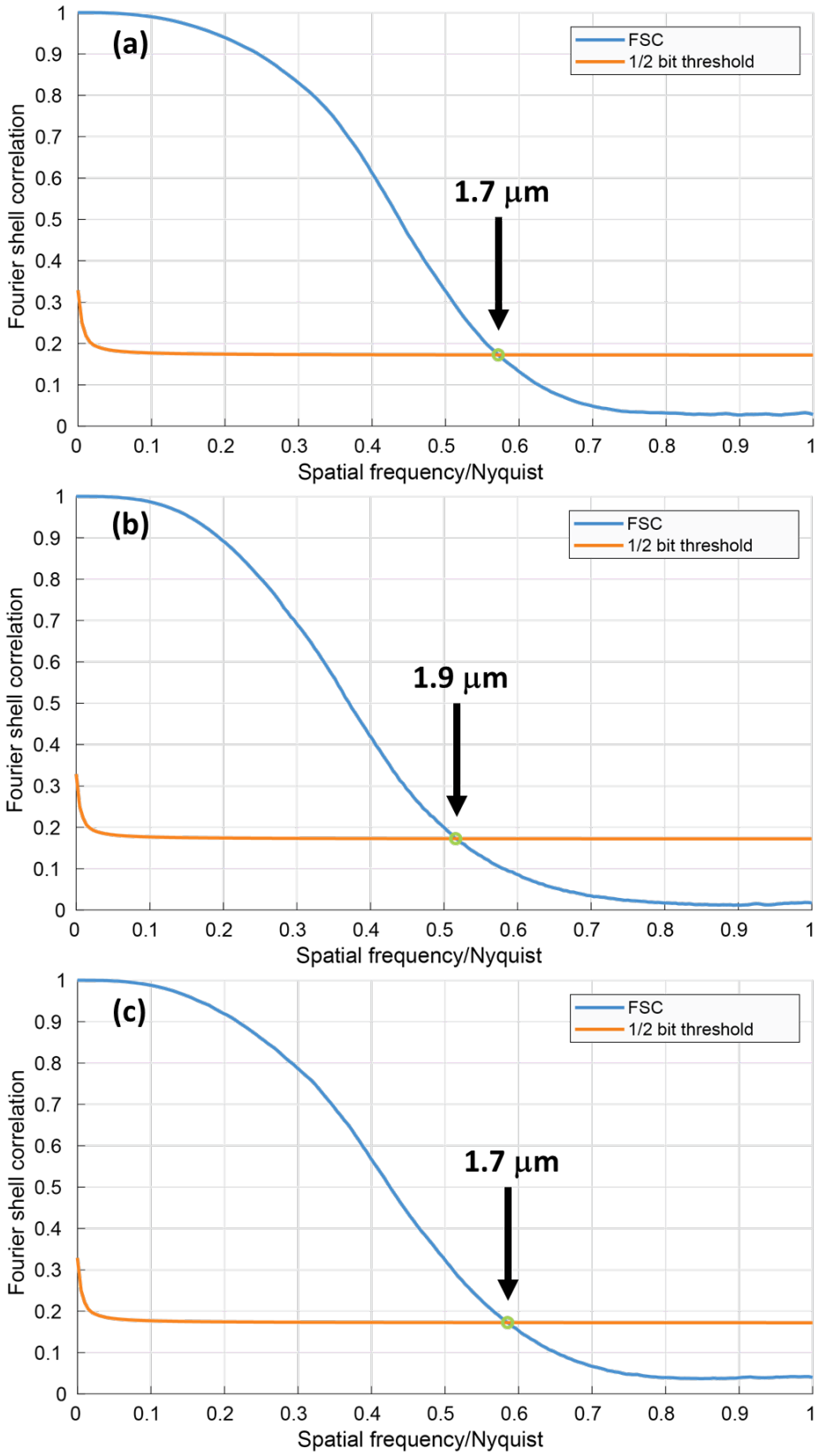

Figure S5. Fourier Shell Correlation plots for the laboratory, attenuation-contrast, microtomographic study, PC-52.5 paste (w/c=0.40) at (a) 19 h, (b) 47 h and (c) 93 h of hydration. The cuts between the FSC traces and the threshold lines give an indication of the spatial resolution of each tomogram.

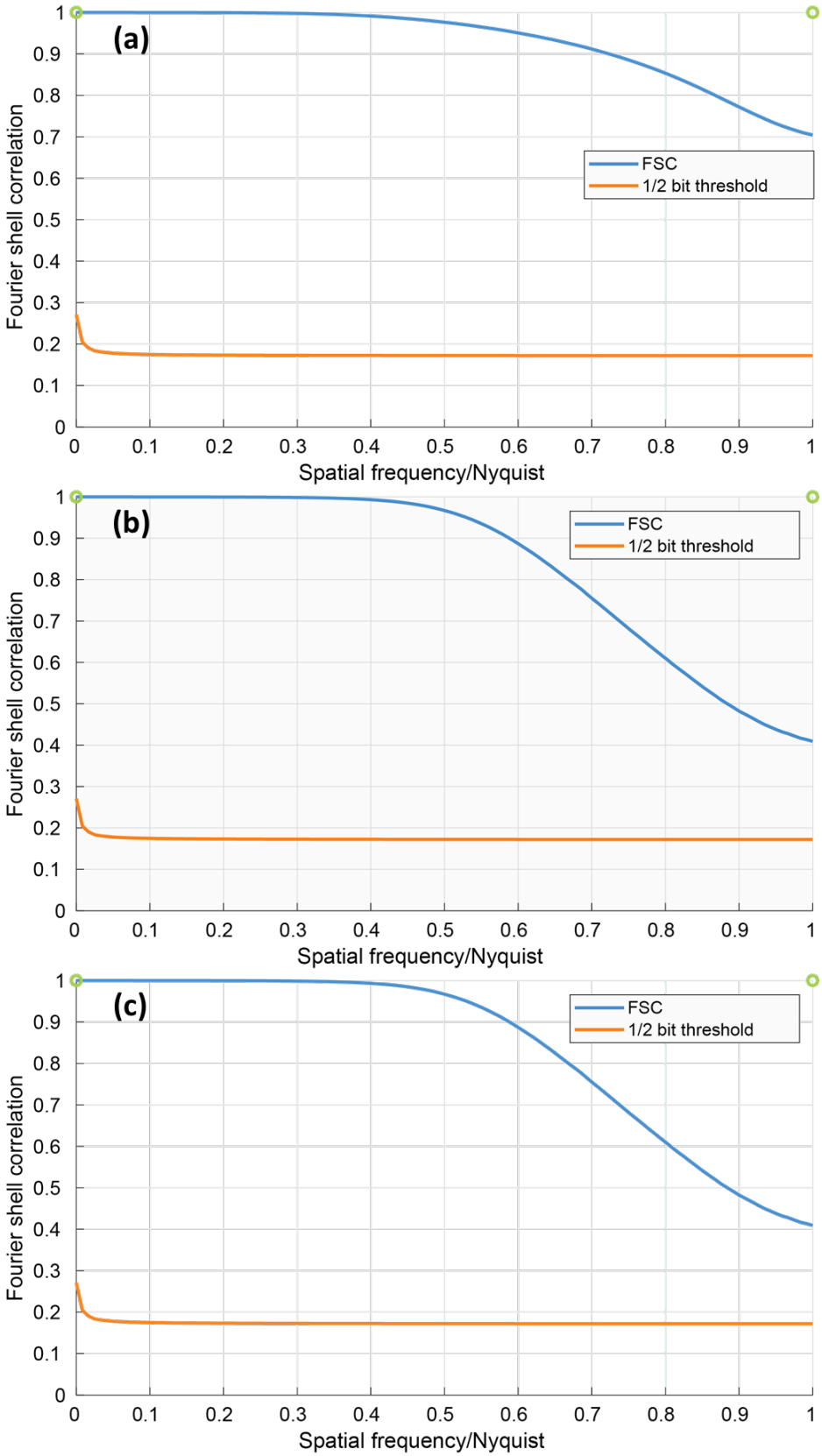

Figure S6. Fourier Shell Correlation plots for the propagation-based synchrotron phase-contrast X-ray computed microtomographic study, PC-42.5 paste (w/c=0.50) at (a) 19 h, (b) 47 h and (c) 93 h of hydration. The FSC traces do not cut the threshold indicating that, from this approach, the overall spatial resolution is limited by the sampling (pixel size).

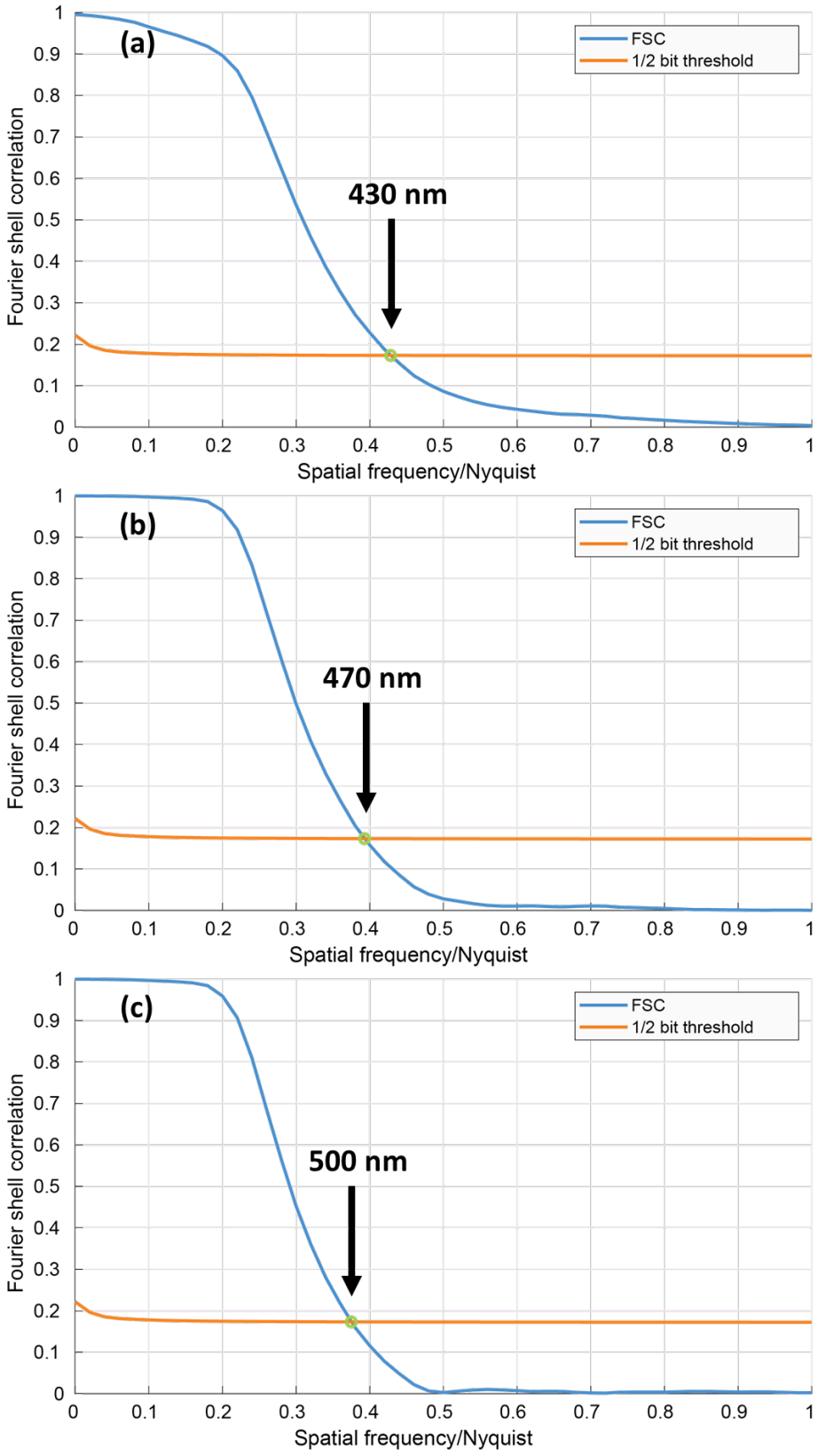

Figure S7. Fourier Shell Correlation plots from the near-field ptychographic X-ray computed tomographic study for the PC-52.5 paste (w/c=0.40) at (a) 19 h, (b) 47 h and (c) 93 h of hydration. The cuts between the FSC traces and the threshold lines give an indication of the spatial resolution of each tomogram. The slightly better spatial resolution measured for the 19 h tomogram is very likely due to the smaller scanning step size, i.e. 6 μm, and the corresponding larger acquisition time, i.e. 3h 55 min. The scanning step size for the other two tomograms was 7 μm, yielding 3h 6 min of acquisition time.

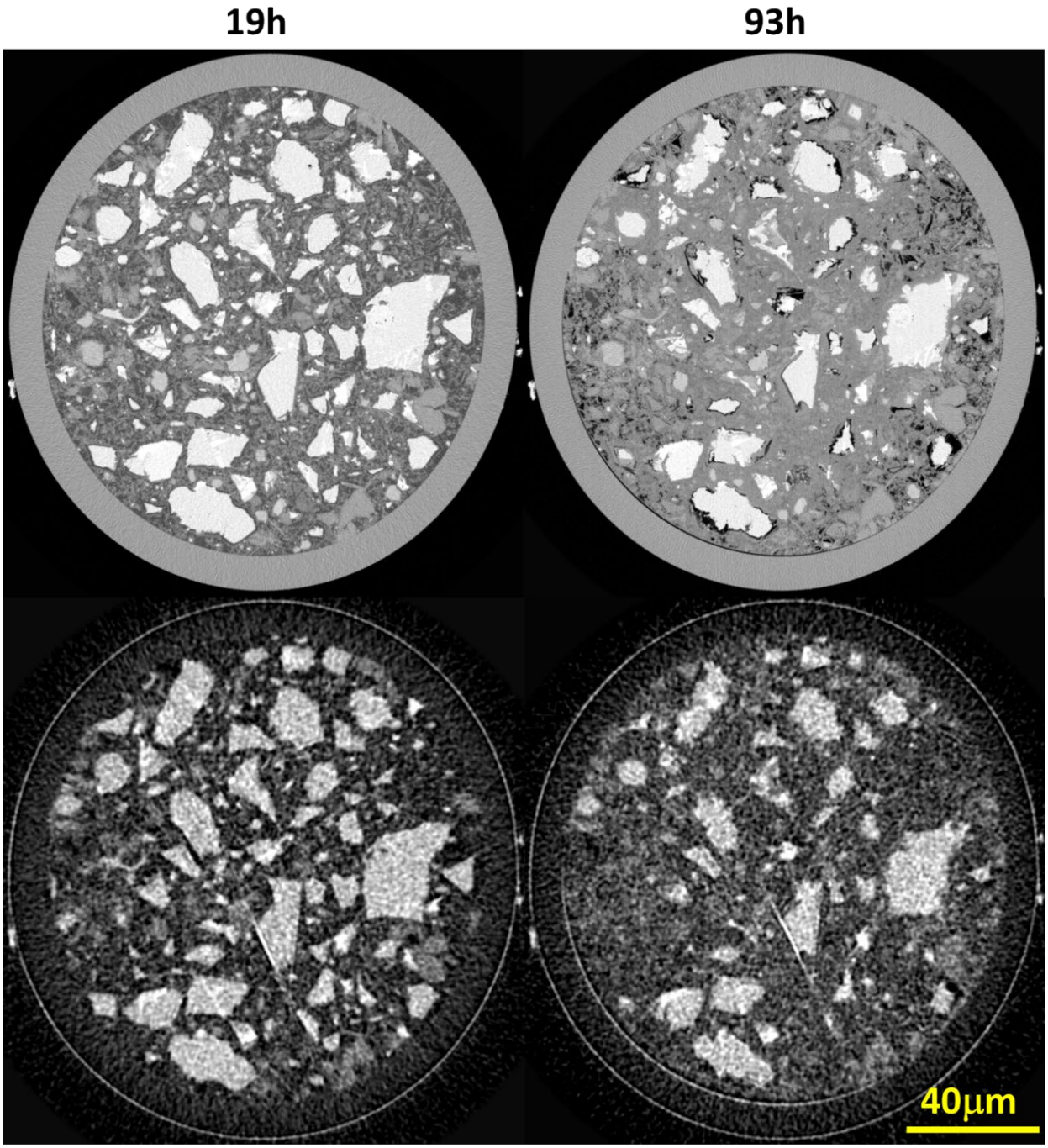

Figure S8. Selected PXCT orthoslices at 19 and 93 h of hydration. (Top) Electron density datasets. (Bottom) Absorption datasets.

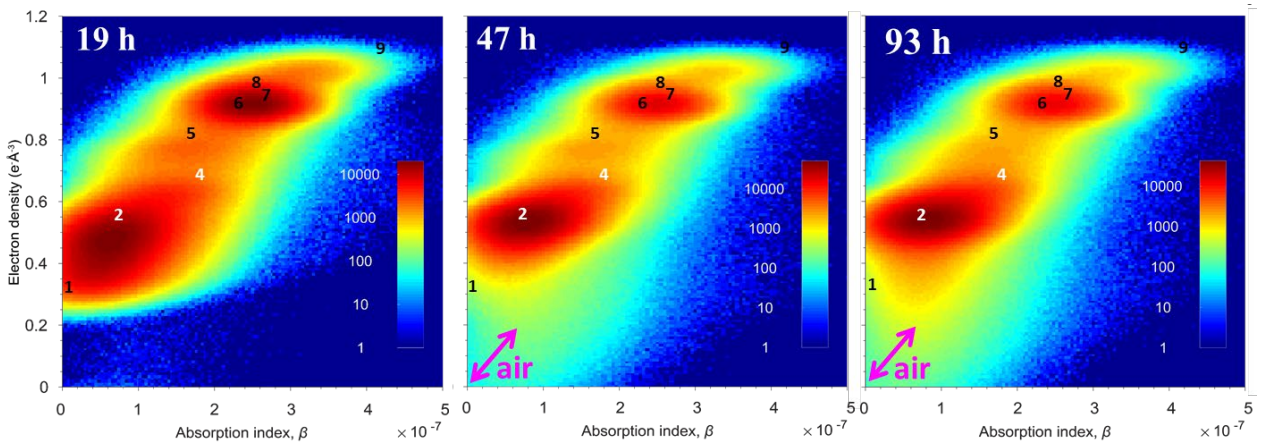

Figure S9. Bivariate histograms of electron densities and absorption indexes (β) for the PXCT study of the PC-52.5 paste (w/c=0.40) at the three studies hydration ages. The positions of the different components, as expected from the crystallographic data, are given. C-S-H gel position (component #3) is not given, as it is a non-stoichiometric solid, but it should be close to ettringite (#2). The electron density and absorption of air is zero but the partial volume effect slightly displaces the values, see pink arrows. For the numbers/components, the reader is referred to Table S7.

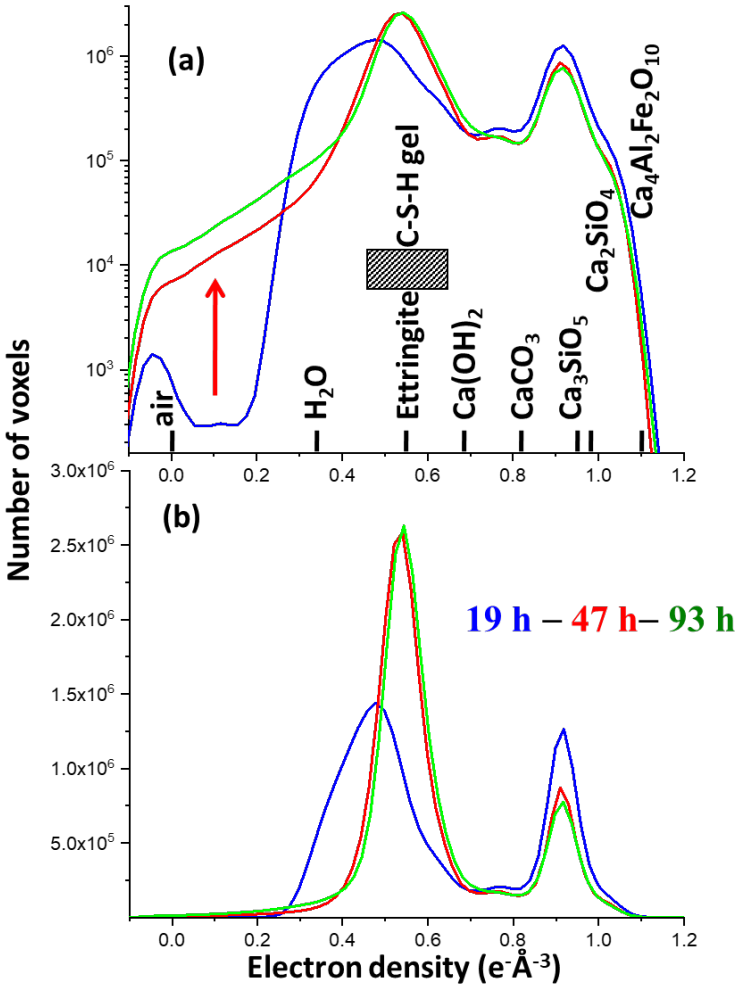

Figure S10. Volume-of-interest histogram of the electron densities for the PXCT study of the PC-52.5 paste (w/c=0.40) at (blue) 19 h, (green) 47 h and (red) 93 h of hydration. (a) Logarithmic scale, (b) Linear scale. The expected (from the crystal structures) electron densities for the different components are labelled in (a). C-S-H gel is an amorphous solid with variable water content and Ca/Si molar ratio and therefore, the expected electron densities are a range.

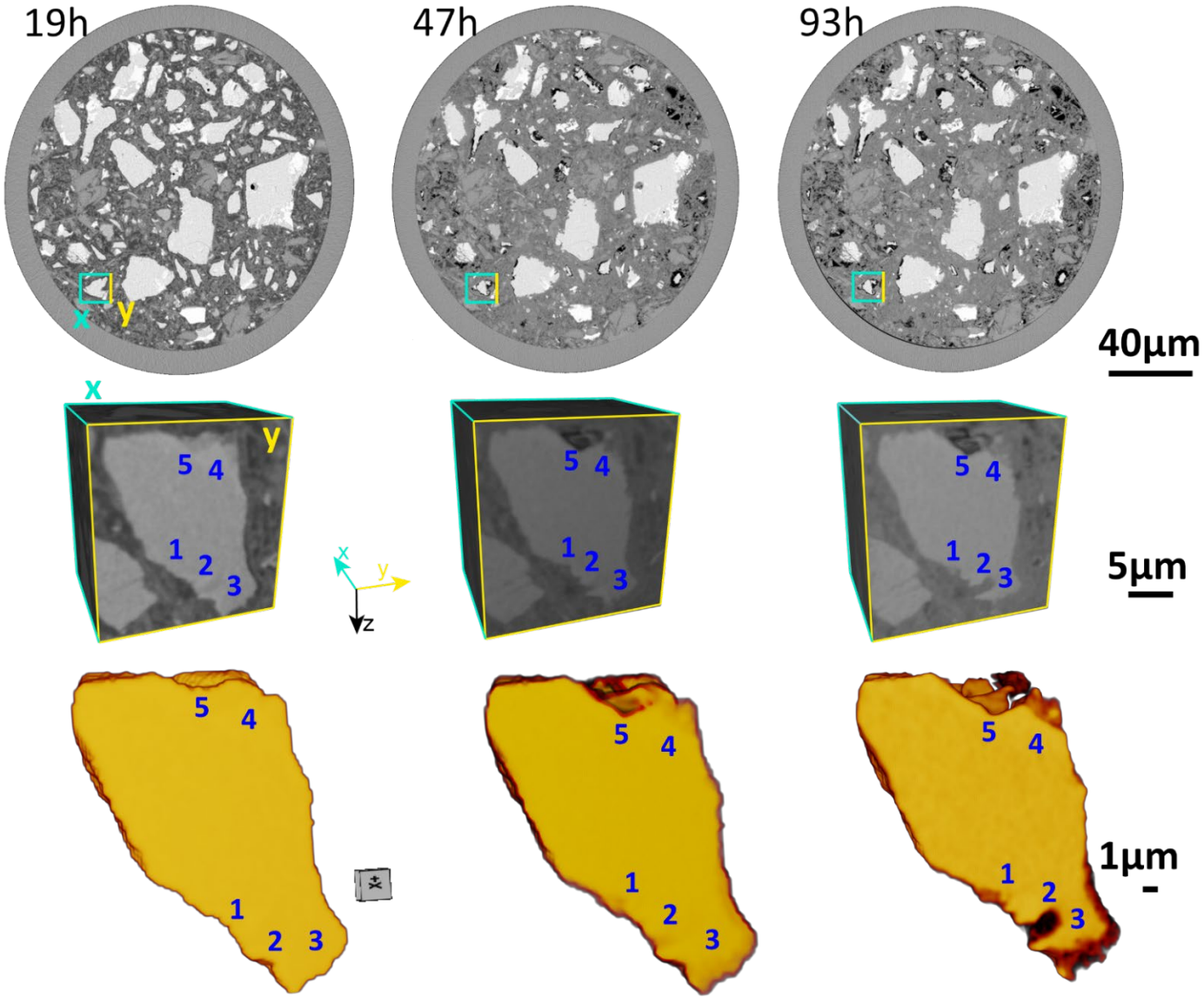

Figure S11. Second etch-pit evolution picture. (Top row) PXCT orthoslices at the three studied ages. (Intermediate) 3D rendering of a volume including a fraction of the alite particle highlighted in the top panels. (Bottom) 3D representation of the segmented particle to highlight the evolution of the etch-pits. These 3D rendered views do not show exactly the electron densities as they are affected by visualization features like the lighting source.

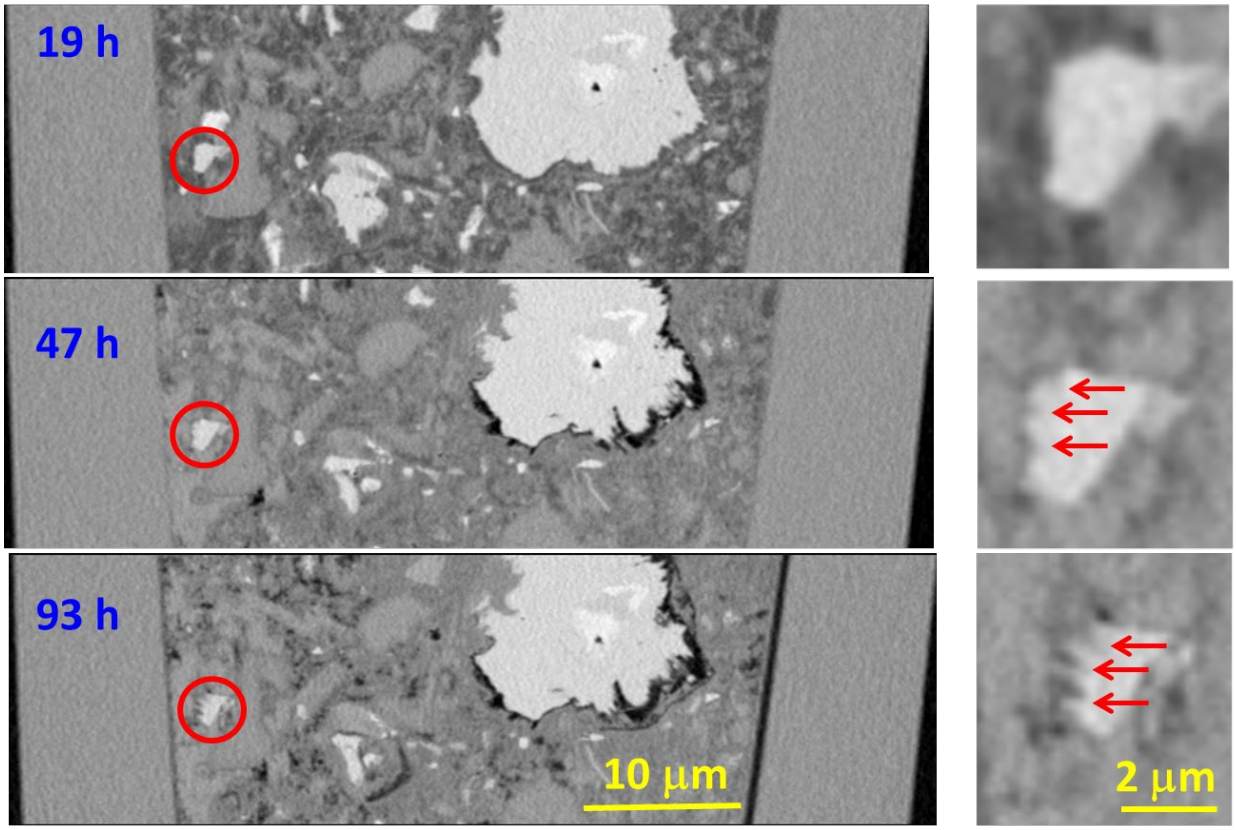

Figure S12. Selected PXCT vertical views at the studied ages showing the evolution of the PC-52.5 paste. This series is intended to show the evolution of water porosity (dark-grey) towards air porosity (black) with time. Moreover, the enlarged views (right images) show the evolution of a small alite particle, initial size about 3 µm, which develops etch-pits of sizes of ~700 nm, highlighted with red arrows.

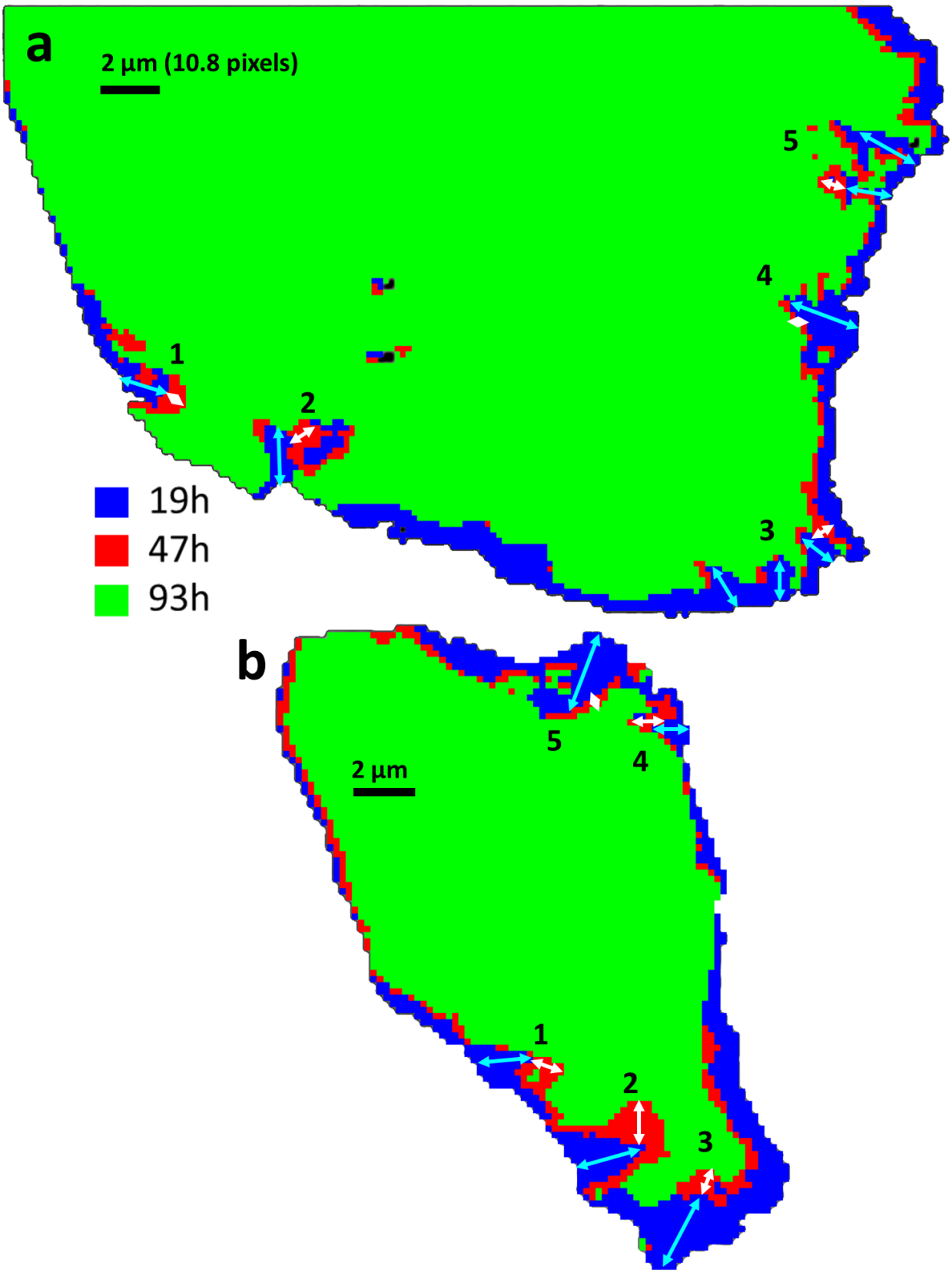

Figure S13. Overlay of the (2D-projected) alite segmented pixels during the hydration process to show the large variability in the growth rates of the etch-pits. a, five etch-pits corresponding to the Figure 4 of the manuscript. b, five etch-pits corresponding to the Figure S11 of this SI. Pale-blue arrows show size changes from 19h to 47h, meanwhile white arrows display to the changes from 47h to 93h.

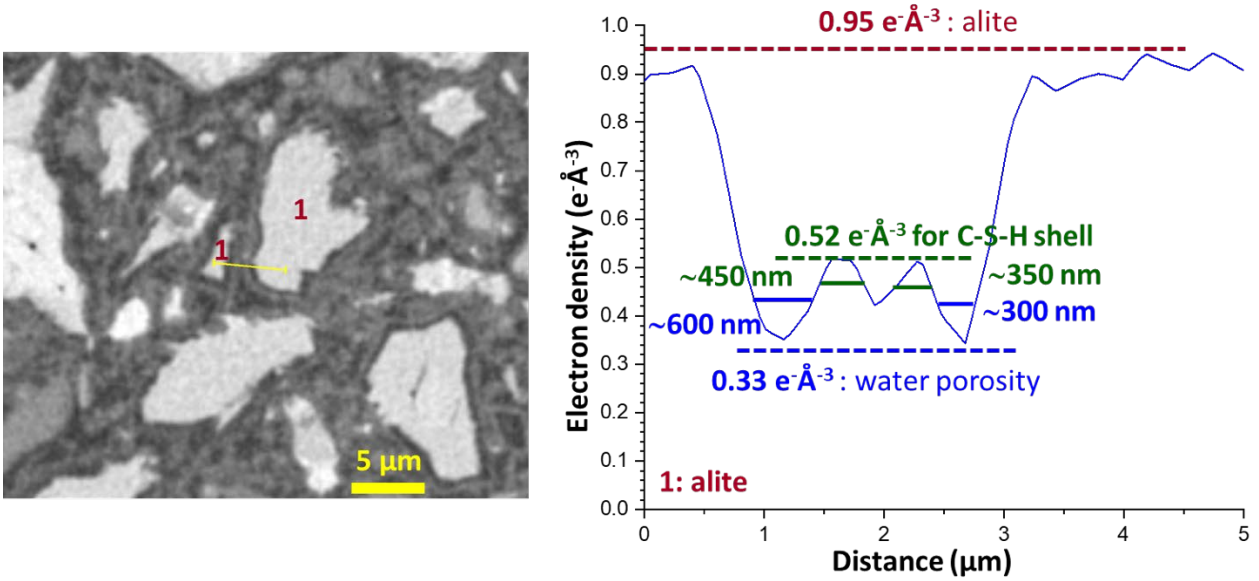

Figure S14. (Left panel) Selected 2D view of the PXCT data at 19 h. (Right) Electron density profile corresponding to the yellow straight line. The line profile signals the water porosity region (blue) surrounding the two alite particles, with the sizes of the C-S-H gel shells and their electron densities given in green.

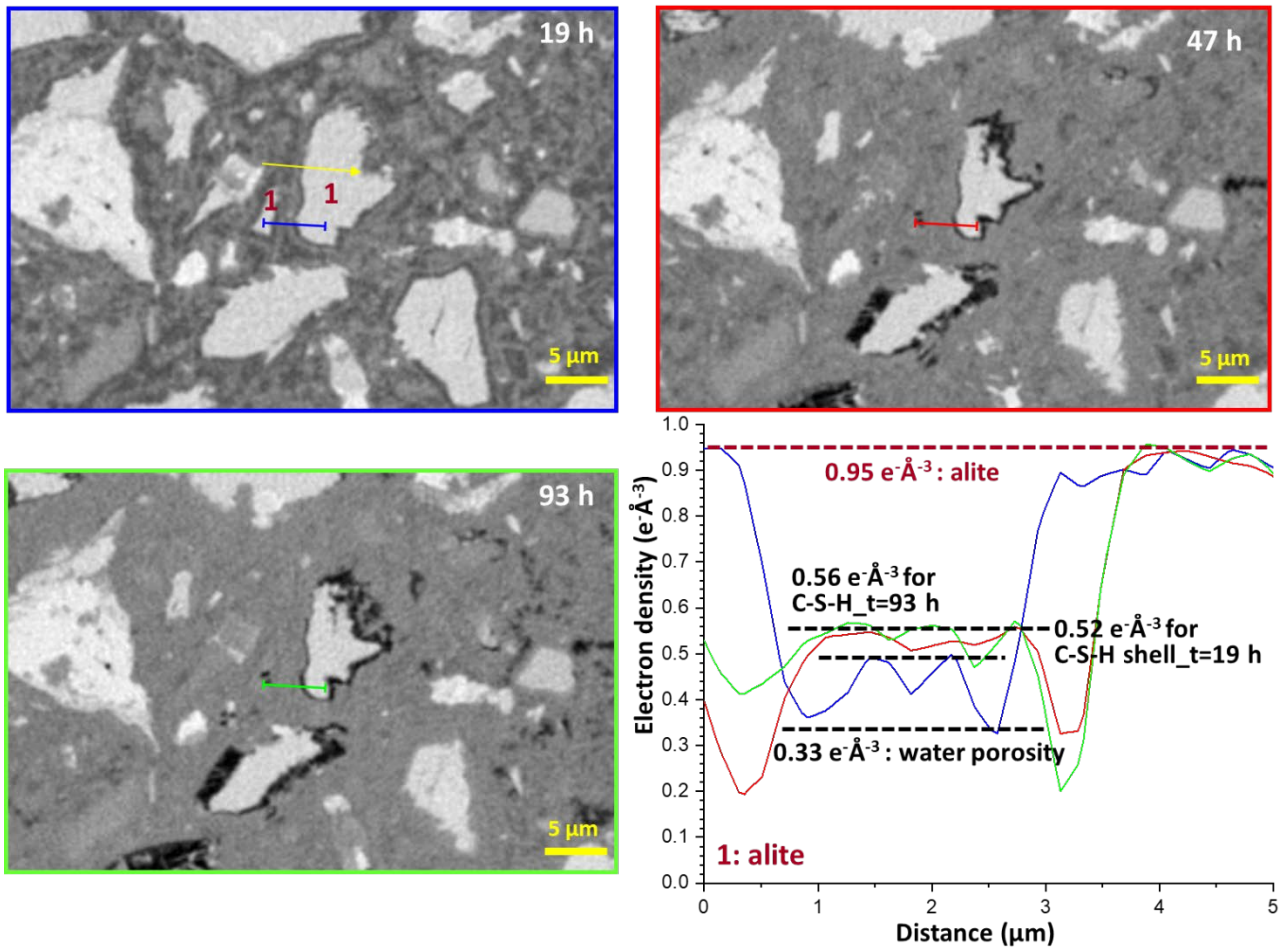

Figure S15. Study of the alite dissolution and C-S-H gel (shell) densification with hydration time. Same region than that shown in Fig. S13.

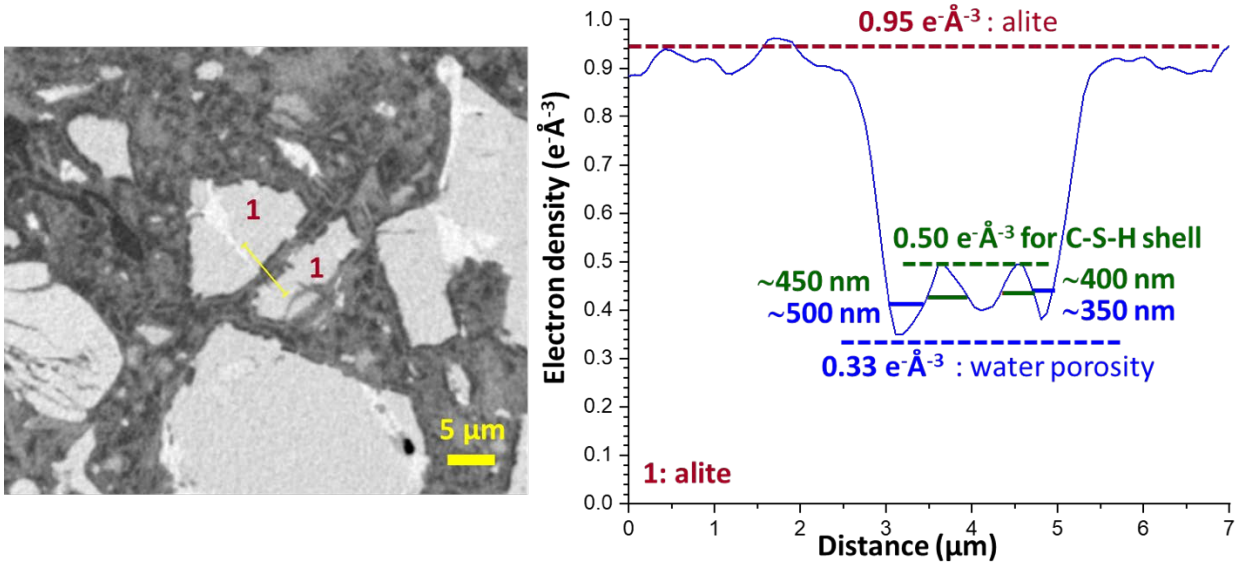

Figure S16. (Left panel) Selected 2D view of the PXCT data at 19 h. (Right) Electron density profile corresponding to the yellow straight line. The line profile signals the water porosity region (blue) surrounding the two alite particles, with the sizes of the C-S-H gel shells and their electron densities given in green.

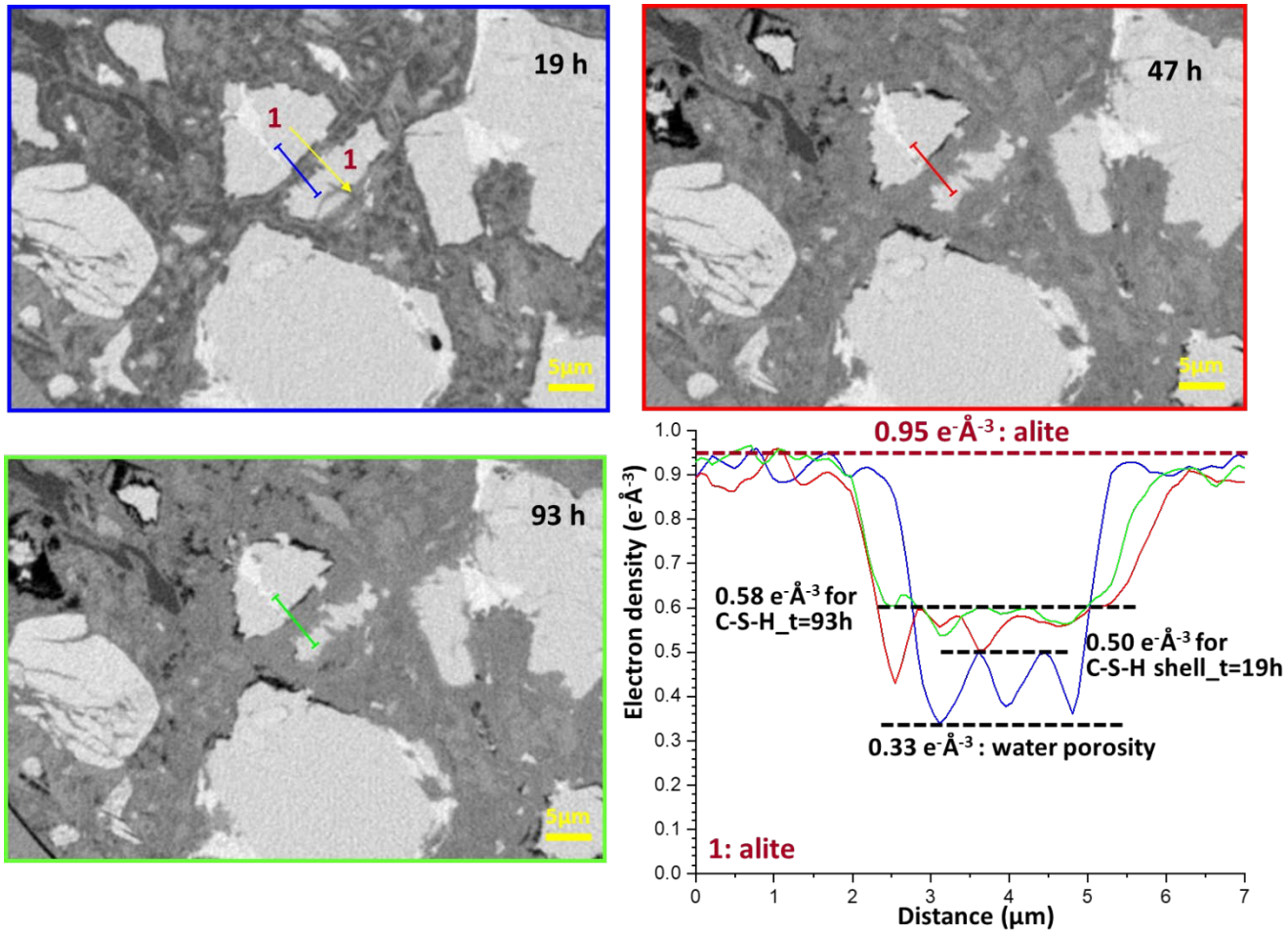

Figure S17. Study of the alite dissolution and C-S-H gel (shell) densification with hydration time. Same region than that shown in Fig. S15. Capillary pore water is still visible at 93 h in the top left region of the image.

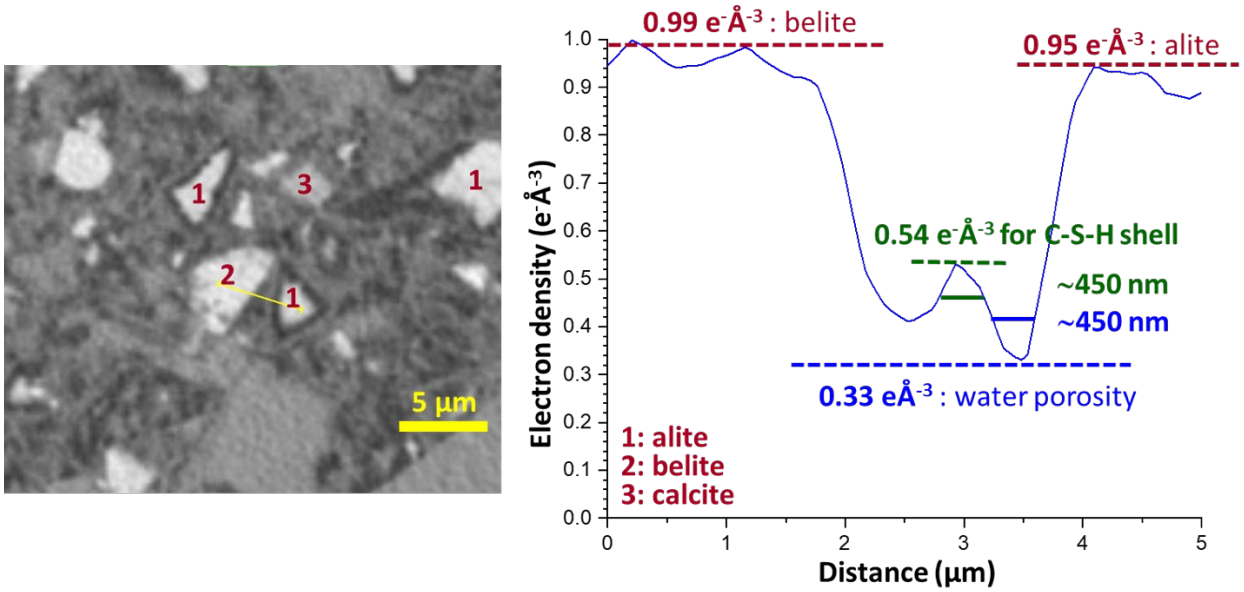

Figure S18. (Left panel) Selected 2D view of the PXCT data at 19 h. (Right) Electron density profile corresponding to the yellow straight line in the right image. The C-S-H porous shell covers every alite particle but it does not surround belite neither calcite. The line profile signals the water porosity region (blue) surrounding alite, with the size of the C-S-H gel shell and its electron density given in green.

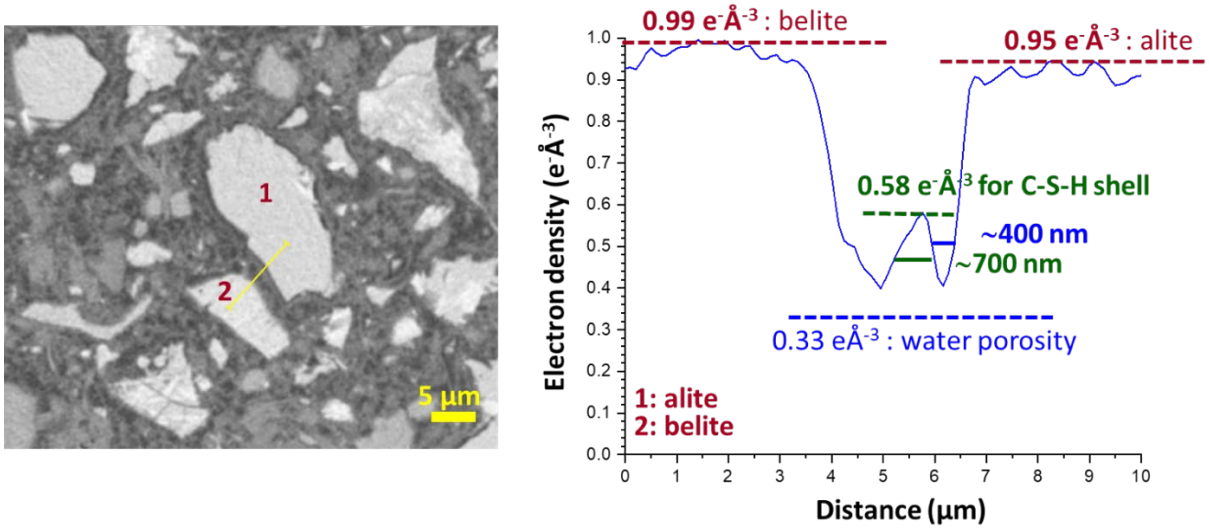

Figure S19. (Left panel) Selected 2D view of the PXCT data at 19 h. (Right) Electron density profile corresponding to the yellow straight line. The C-S-H porous shell covers every alite particle but it does not surround belite grains. The line profile signals the water porosity region (blue) surrounding alite, with the size of the C-S-H gel shell and its electron density given in green.

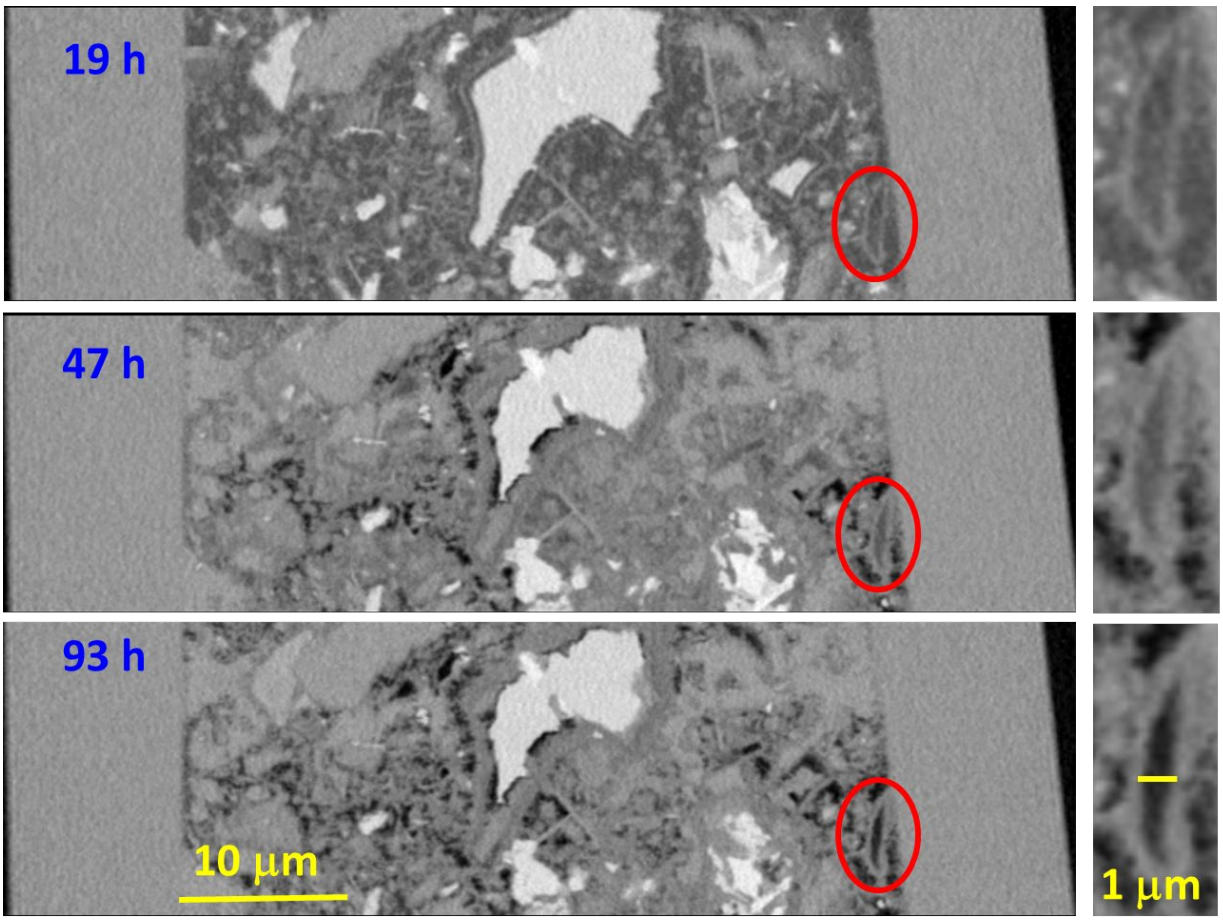

Figure S20. Selected PXCT vertical views at the studied ages showing the evolution of the PC-52.5 paste. This series is intended to show the evolution of water porosity (dark grey) towards air porosity (black) with time. The enlarged views (right images) show the change of a hollow-shell volume, also known as Hadley grain, with hydration time. The hollow-shells, Hadley grains, are fully hydrated small alite particles that contain a void within the original boundary of the anhydrous grain. The hollow regions of the Hadley grains are filled with water at 19 and 47 h but dried at 93 h, see enlarged pictures to the right. This illustrates that most of the capillary pores with sizes larger than ~1 µm are already water emptied at 93 h of hydration, see bottom right. Moreover, it also illustrated that the C-S-H shells are porous as they allow the water diffusion from the inner regions towards the exterior.

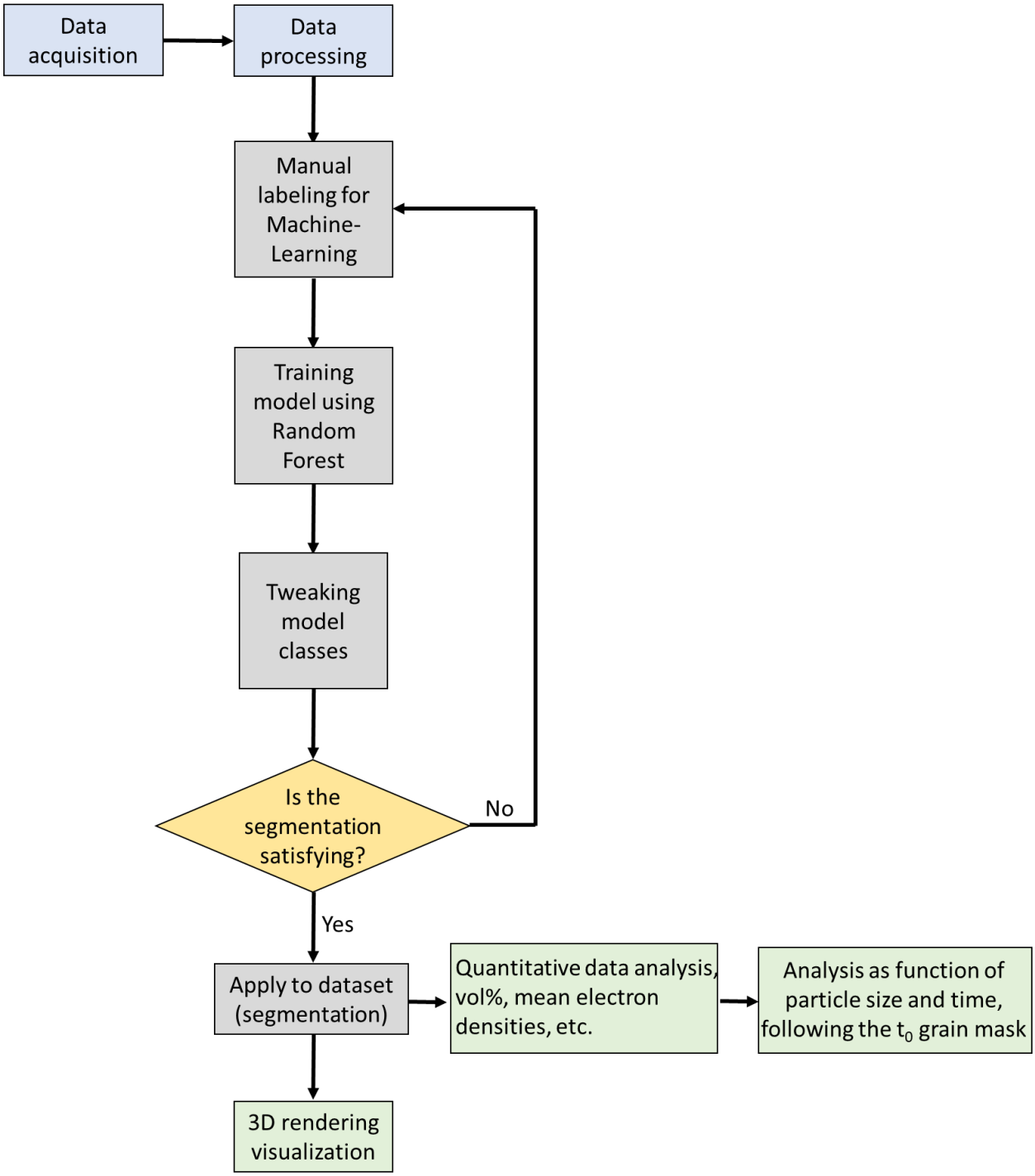

Figure S21. Flow chart describing the data treatment in this work and detailing the machine learning training steps (boxes in grey).

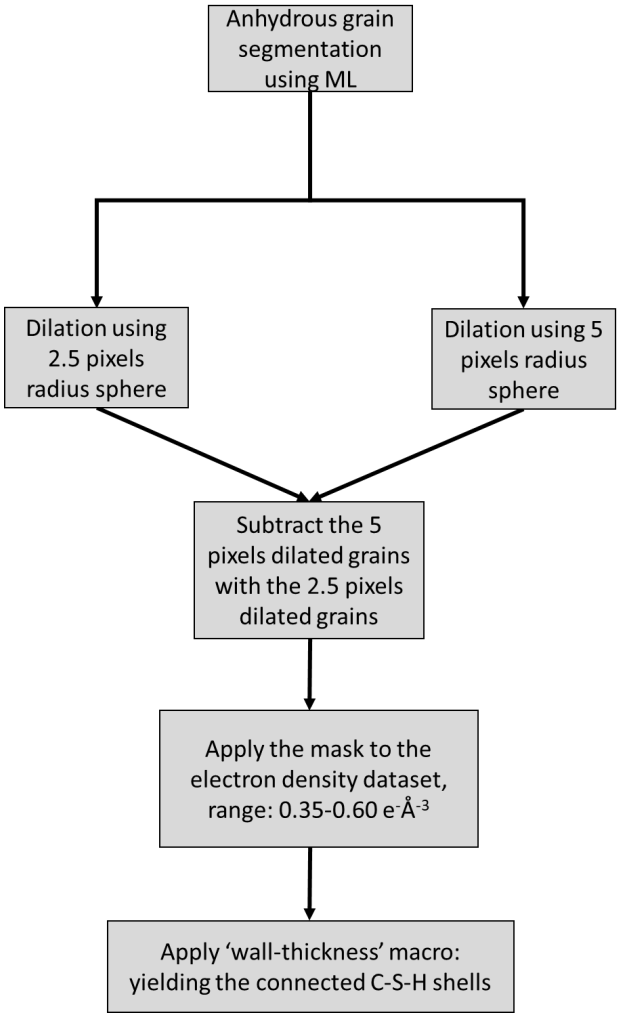

Figure S22. Flow chart detailing the steps for the C-S-H shell segmentation in the 19 h PXCT dataset.

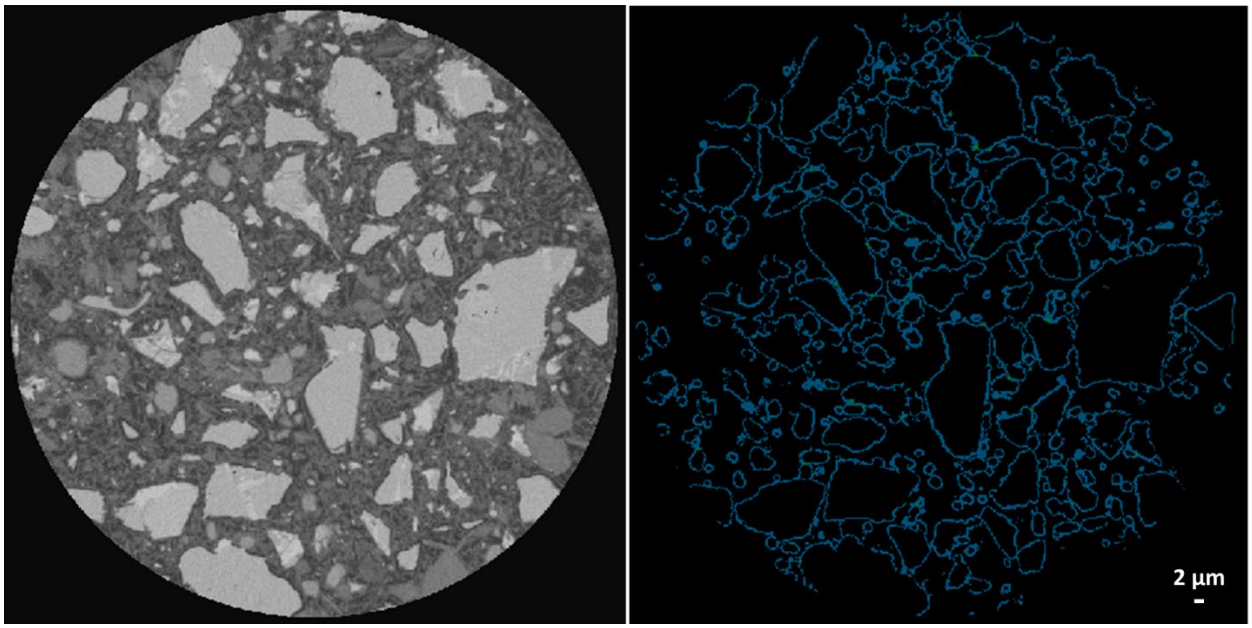

Figure S23. Views, at the same scale, comparing the C-S-H shell as observed in the PXCT raw dataset at 19 h of hydration (left) and the C-S-H shell segmentation output applying the procedure detailed in Fig. S21.

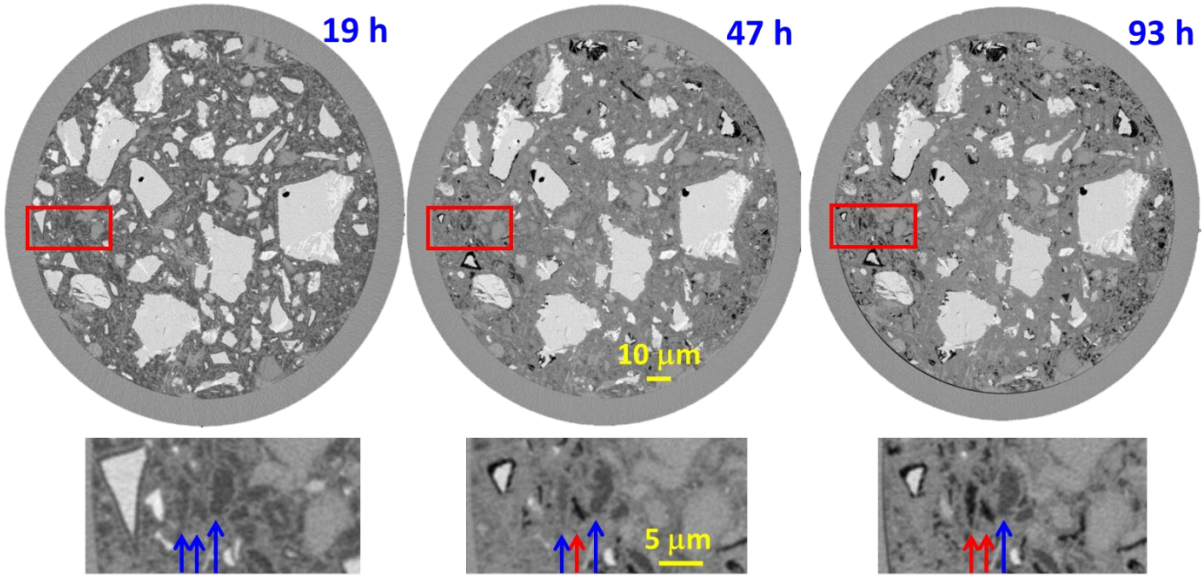

Figure S24. Selected PXCT orthoslices at the studied ages showing the evolution of the PC-52.5 paste. The enlarged views (bottom) show the evolution of porosity within the paste, where several pores of sizes smaller than ~2 µm are dried (red arrows) at 93 h but other larger, pores keep filled with water (blue arrows).

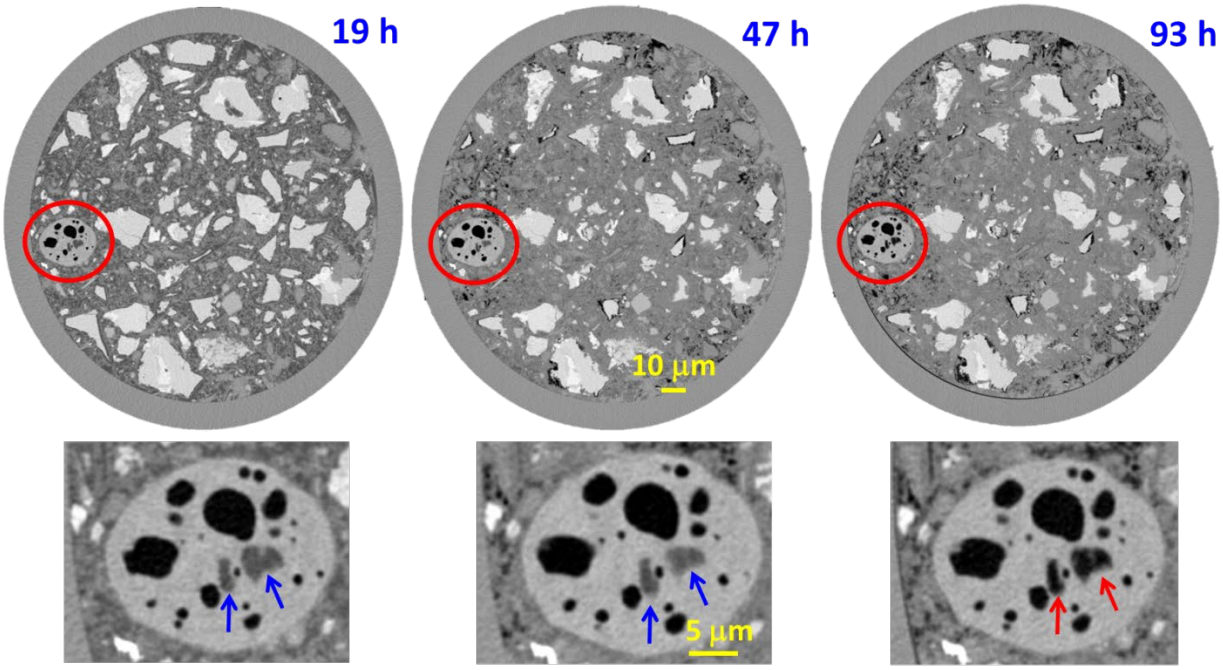

Figure S25. Selected PXCT orthoslices at the three studied ages showing the evolution of the PC-52.5 paste. The enlarged views (bottom) show the evolution of a large calcite particle with internal pores. At 19 and 47 h of hydration some pores are filled with water (highlighted with blue arrows) which are connected to the surface. At 93 h, these pores are empty (red arrows) releasing water for further hydration.

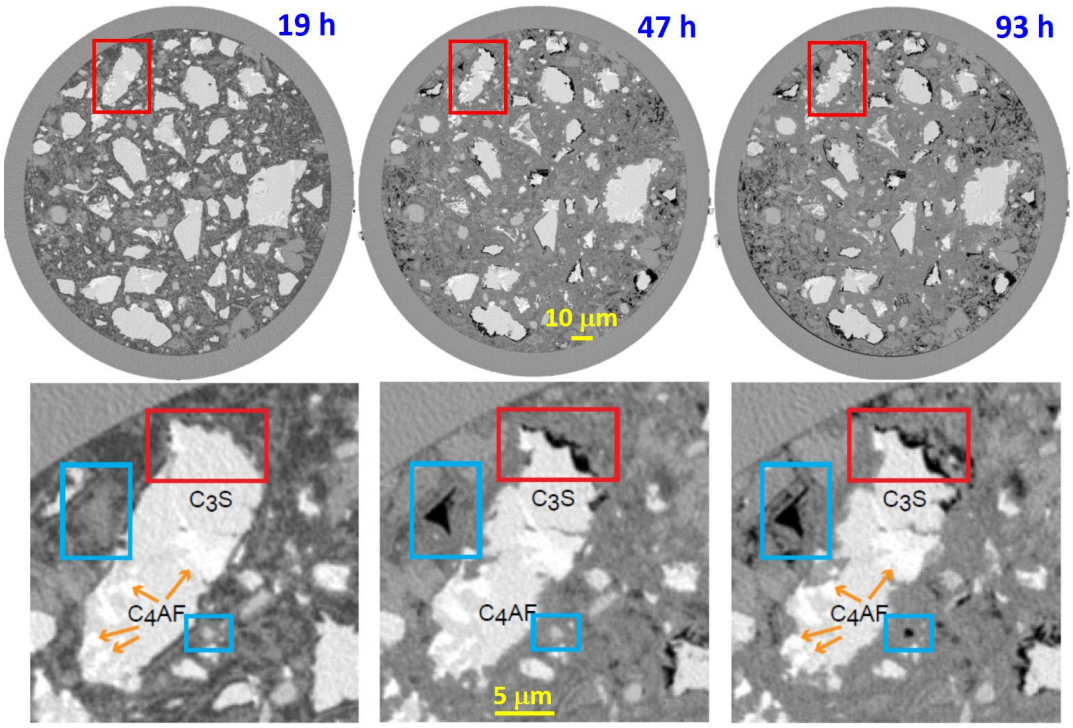

Figure S26. Selected PXCT orthoslices at the studied ages. The chemical shrinkage is evident at 93 h because the appearance of empty (black) regions. The enlarged views (bottom) show: (1) the hydration of a large alite particle with aluminoferrite, C_4AF, intergrown, i.e. the whitest regions, see brown arrows. In addition to the etch-pit evolution, it can be seen that hydration stops at the regions where C_4AF is exposed to the hydration medium; (2) the blue rectangles highlight the dissolution of C-S-H gel particles to give dry (air-filled) pores. Moreover, alite hydration also stops as soon as air porosity (pore drying) develops on the surfaces of the anhydrous grains, see red rectangles in the bottom panels.

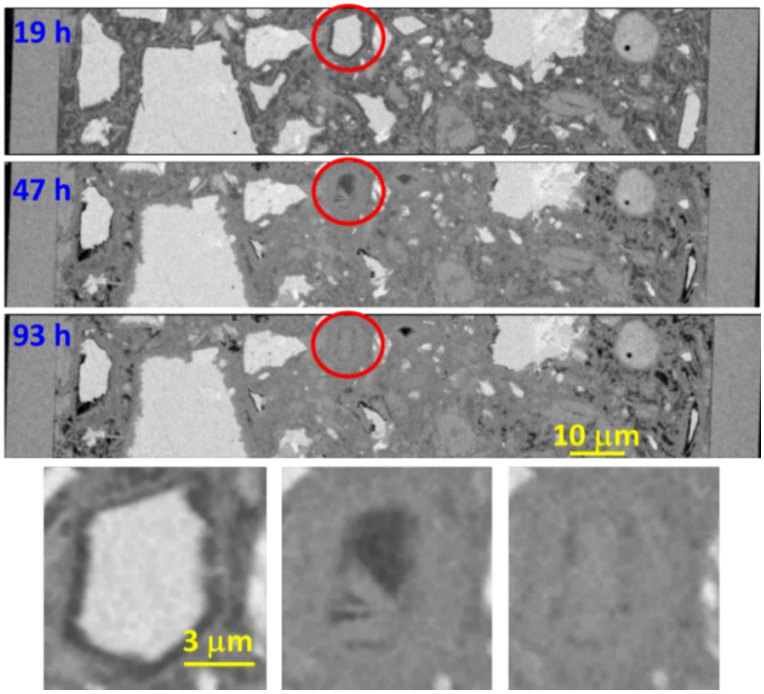

Figure S27. Selected PXCT vertical pictures with enlarged views (bottom) displaying the hydration pathway of a very fast dissolving particle, i.e. a 4 µm particle fully dissolved between 19 and 47 h. The electron density of this small volume, 0.91 $e^{-}Å^{-3}$, is compatible with C_3S or C_3A. It already shows a gap at 19 h indicating a highly soluble component. At 47 h, two hydrate rods of diameter smaller than 1 µm, morphologically suggesting ettringite, grow in the pristine region which is filled with capillary water. At 93 h, the volume is fully occupied by hydrate(s). The dissolution rate between 19 and 43 h is faster than 75 nm/h suggesting C_3A. However, the chemical nature of this tine particle could not be firmly established.

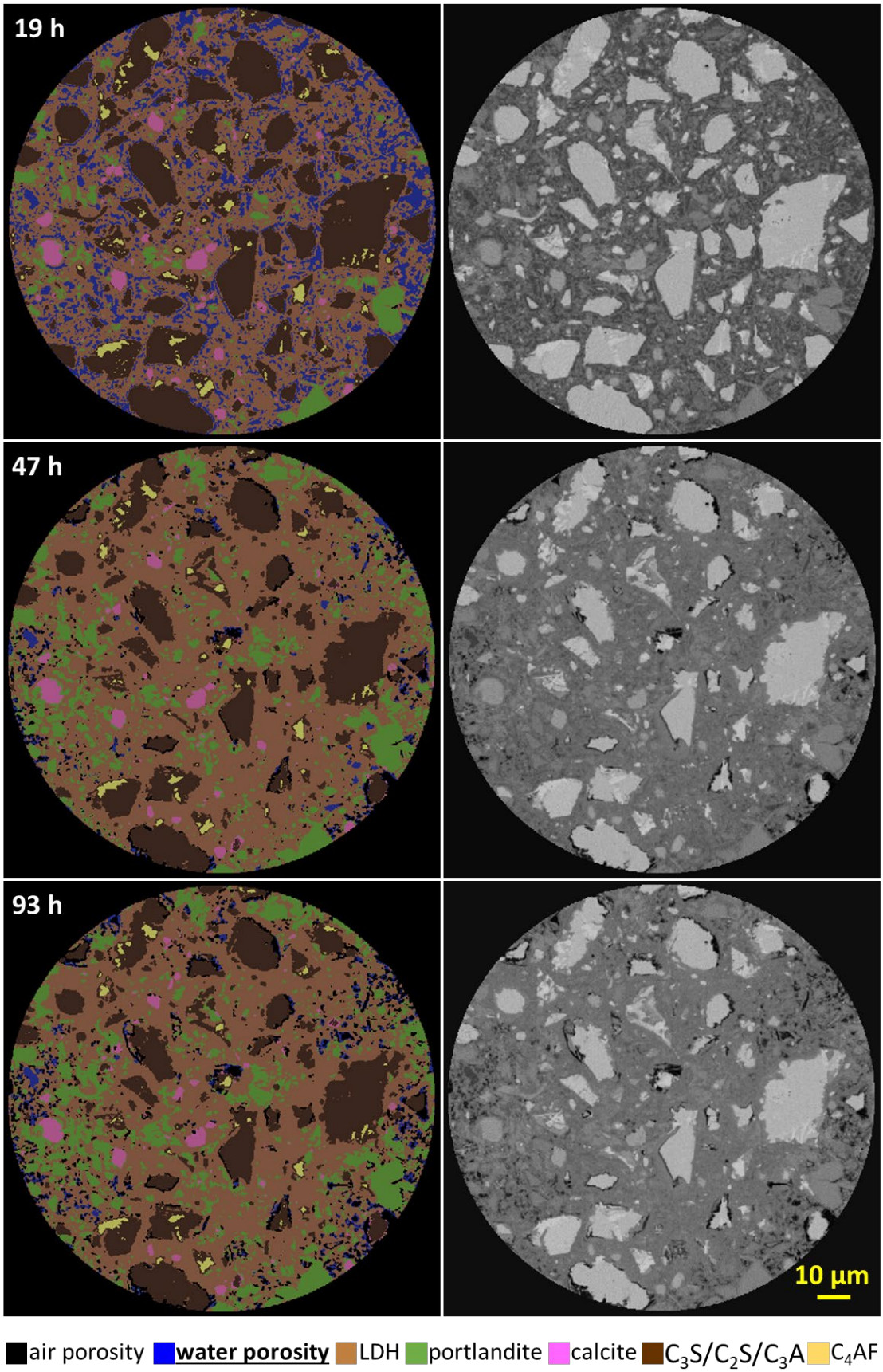

Figure S28. Capillary water porosity evolution, with the obtained spatial resolution (i.e. approximately two voxels). Field of view ~160 µm. (Left) ML segmentation output. (Right) 2D orthoslices of the raw PXCT datasets.

• Supplementary movies

- **Movie-1:** "Summary of 4D nanoimaging of cement hydration" 43 seconds.

  A summarized display of the cement paste hydration evolution as seen by this nanoimaging study. The progress of the different components is displayed after segmentation by Machine-Learning. Moreover, key changes like water porosity evolution or shrinkage development are highlighted on the video by embedded written text.

- **Movie-2:** " C-S-H shell characterization at 19 hours " 17 seconds.

  A video revealing the arrangement of the 3D segmented C-S-H shells through the 19 h nanoimaging dataset.

The size of each short video is standard 640×480 pixels in mp4 format as suggested by Nature journal. Therefore, users can download them quickly.

Article cover image:

Title: "X-ray nanoimaging of a hydrating cement paste at early ages"

Description: The precipitating calcium silicate hydrate shells (blue) surround the dissolving alite particles (yellow) with regions of calcium aluminoferrite highlighted in orange. For better visualisation: only the C-S-H shells in the left part, the three components in the middle region, just the anhydrous cement particles in the right part. The gaps, approximately 500 nm, between the C-S-H shells and the dissolving alite particles are readily visible in the central part of the image.

The cover image is a high resolution 5000×4005 pixels size in .tif format.

Cover image credit: Shiva Shirani, Cover design: Maziar Moussavi

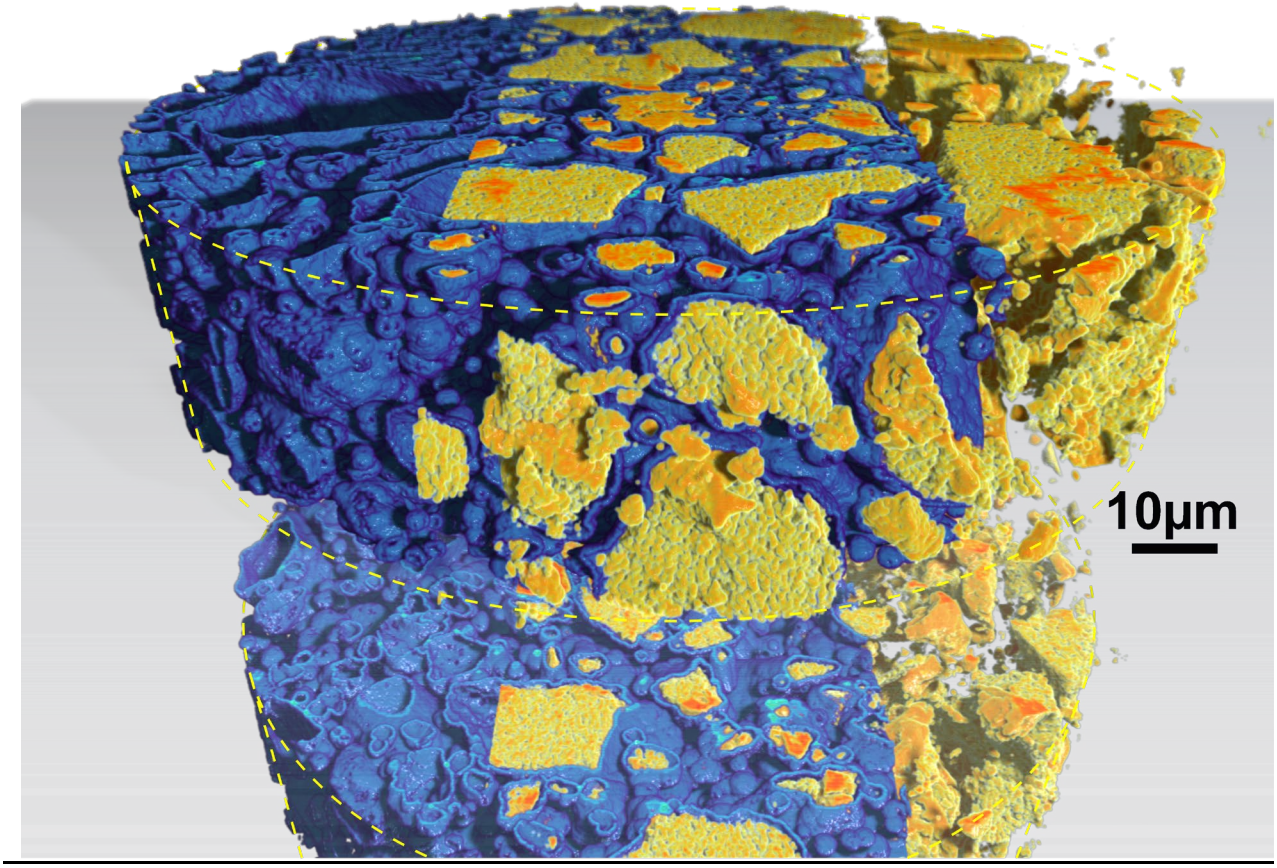

• **Supplementary References**

1. Douissard, P. A. *et al.* A versatile indirect detector design for hard X-ray microimaging. *J. Instrum.* **7**, P09016 (2012).
2. Martin, T. *et al.* LSO-based single crystal film scintillator for synchrotron-based hard X-ray micro-imaging. *IEEE Trans. Nucl. Sci.* **56**, 1412–1418 (2009).
3. Paganin, D., Mayo, S. C., Gureyev, T. E., Miller, P. R. & Wilkins, S. W. Simultaneous phase and amplitude extraction from a single defocused image of a homogeneous object. *J. Microsc.* **206**, 33–40 (2002).
4. Vigano, N., Cloetens, P., di Michiel, M., Rack, A. & Tafforeau, P. Redefining the ESRF tomography software. in *Digital Holography and Three-Dimensional Imaging 2021* paper DF2G.4 (OSA Technical Digest, Optica Publishing Group, 2021). doi:10.1364/DH.2021.DF2G.4.
5. van Heel, M. & Schatz, M. Fourier shell correlation threshold criteria. *J. Struct. Biol.* **151**, 250–262 (2005).
6. Holler, M. *et al.* An instrument for 3D x-ray nano-imaging. *Rev. Sci. Instrum.* **83**, 073703 (2012).
7. Holler, M. *et al.* X-ray ptychographic computed tomography at 16 nm isotropic 3D resolution. *Sci. Rep.* **4**, 3857 (2014).
8. Odstrčil, M., Lebugle, M., Guizar-Sicairos, M., David, C. & Holler, M. Towards optimized illumination for high-resolution ptychography. *Opt. Express* **27**, 14981 (2019).
9. Huang, X. *et al.* Optimization of overlap uniformness for ptychography. *Opt. Express* **22**, 12634 (2014).
10. Dinapoli, R. *et al.* EIGER: Next generation single photon counting detector for X-ray applications. *Nucl. Instruments Methods Phys. Res. Sect. A Accel. Spectrometers, Detect. Assoc. Equip.* **650**, 79–83 (2011).
11. Odstrcil, M., Lebugle, M., Lachat, T., Raabe, J. & Holler, M. Fast positioning for X-ray scanning microscopy by a combined motion of sample and beam-defining optics. *J. Synchrotron Radiat.* **26**, 504–509 (2019).
12. Wakonig, K. *et al.* PtychoShelves, a versatile high-level framework for high-performance analysis of ptychographic data. *J. Appl. Cryst* **53**, 574–586 (2020).
13. Thibault, P., Dierolf, M., Bunk, O., Menzel, A. & Pfeiffer, F. Probe retrieval in ptychographic coherent diffractive imaging. *Ultramicroscopy* **109**, 338–343 (2009).
14. Guizar-Sicairos, M. *et al.* Phase tomography from x-ray coherent diffractive imaging projections. *Opt. Express* **19**, 21345 (2011).
15. Odstrčil, M., Holler, M., Raabe, J. & Guizar-Sicairos, M. Alignment methods for nanotomography with deep subpixel accuracy. *Opt. Express* **27**, 36637–36652 (2019).
16. Diaz, A. *et al.* Quantitative x-ray phase nanotomography. *Phys. Rev. B* **85**, 020104 (2012).
17. Kaestner, A. P. *et al.* Recent developments in neutron imaging with applications for porous media research. *Solid Earth* **7**, 1281–1292 (2016).
18. Donnelly, C. *et al.* Time-resolved imaging of three-dimensional nanoscale magnetization dynamics. *Nat. Nanotechnol.* **15**, 356–360 (2020).
19. Li, X. *et al.* Direct observation of C3S particle dissolution using fast nano X-ray computed tomography. *Cem. Concr. Res.* **166**, 107097 (2023).
20. Cuesta, A. *et al.* Quantitative disentanglement of nanocrystalline phases in cement pastes by synchrotron ptychographic X-ray tomography. *IUCrJ* **6**, 473–491 (2019).
21. Linderoth, O., Wadsö, L. & Jansen, D. Long-term cement hydration studies with isothermal calorimetry. *Cem. Concr. Res.* **141**, 106344 (2021).
22. Trtik, P., Diaz, A., Guizar-Sicairos, M., Menzel, A. & Bunk, O. Density mapping of hardened cement paste using ptychographic X-ray computed tomography. *Cem. Concr. Compos.* **36**, 71–77 (2013).
23. Aranda, M. A. G., Cuesta, A., De la Torre, A. G., Santacruz, I. & León-Reina, L. Diffraction and

crystallography applied to hydrating cements. in *Cementitious Materials: Composition, Properties, Application* (ed. Pöllmann, H.) 31–60 (De Gruyter, 2017). doi:10.1515/9783110473728-003.

24. De la Torre, A. G., Santacruz, I., Cuesta, A., León-Reina, L. & Aranda, M. A. G. Diffraction and crystallography applied to anhydrous cements. in *Cementitious Materials* (ed. Pöllmann, H.) 3–29 (De Gruyter, 2017).
25. Henke, B. L., Gullikson, E. M. & Davis, J. C. X-Ray Interactions: Photoabsorption, Scattering, Transmission, and Reflection at E=50−30,000 eV, Z= 1−92. *At. Data Nucl. Data Tables* **54**, 181–342 (1993).

nature portfolio

Peer Review File

4D nanoimaging of early age cement hydration

REVIEWER COMMENTS

Reviewer #1 (Remarks to the Author):

The strength of this study, in my opinion, is in the exploration of a new nanoimaging technique, PXCT, to study the early hydration of Portland cement. With the unprecedented spatial resolution and contrast of PXCT, in situ identification of the evolution of various mineral phases, the C-S-H gel shells, etch pits, water pores and air pores, etc. became possible, hence the corresponding cement dissolution and precipitation processes at early ages associated with them was studied, and qualitative and quantitative results were obtained. The results are of potential interest to researchers working in X-ray computerized tomography and could illustrate a new characterization direction for the cement-based materials community.

The approach, data analysis and interpretation are valid, comprehensive and correct, and the evidence presented justify the conclusions. The literature is adequately cited. The clarity and accessibility of the text is good, and the results have been provided with sufficient context and consideration of previous work.

There are several issues however that I think should be clarified to help improve the work.

1.In the manuscript, it is said "In situ near-field data were taken as detailed in methods……. radiation damage cannot be discarded but it is small, if any. (Page 5) " "Time resolutions of ~1 h will open the way to accurately study the processes in the acceleration period. However, in these cases, radiation damage could be an issue if the total dose is not kept low. (Page 12)"
Will radiation damage affect the visualization results of the evolution of water porosity towards air porosity with time? In addition, migration of C-S-H gel was observed. Is it possible that this was also affected by radiation damage? How will the effect of radiation damage be considered in the future research with higher time resolution?

2.The evolution of water porosity towards air porosity with time was observed around some Alite grains. How will this affect further hydration of Alite and etch pits growth when there is no water around?

3.In the manuscript, it is said "The hollow regions of the Hadley grains are filled with water at 19 and 47 h but dried at 93 h, see enlarged pictures to the right. This illustrates that most of the capillary pores with sizes larger than ~1 μm are already water emptied at 93 h of hydration, see bottom right. (Figure S19)", "The enlarged views (bottom) show the evolution of porosity within the paste, where several pores of sizes smaller than ~2 μm are dried (red arrows) at 93 h but other larger, pores keep filled with water (blue arrows). (Figure S23)"
Is there a contradiction between those two conclusions, for the pores to be empty at 93 h, the former is >1μm and the latter is <2μm? Does the water migrate randomly?

4.The water to cement ratio is relatively higher near the capillary wall than that in the center. In Figure S27, wall effect in the 19h capillary tube sample could be observed. Will the degree of hydration of cement particles of the same size be affected by wall effect at different locations? It should be addressed in the manuscript.

Reviewer #2 (Remarks to the Author):

In this manuscript, the authors report the study of the early stage of cement hydration using mainly near-field ptychographic X-ray computed tomography. They provide a unique combination of spatial & temporal resolution + field of view. It allows the determination of quantitative values for dissolution rates and etch-pit growth rates. A comparison with data obtained by lab and synchrotron X-ray micro-tomography is also proposed. The paper shows an extended collection of data using state of the art technique and an interesting 3D data analysis based on machine learning process. Nevertheless, the manuscript shows some incoherencies and approximations, the results are not sufficiently described and discussed, especially the ones reported in the abstract.

Thus, I cannot support this work for publication in Nature communications in its present form.
Some specific comments and remarks linked to my previous general comment:
For the PXCT study, the size of the capillary used is different between the different sections and figures 160 µm vs 200 µm. This information is important. Indeed, it is highlighted (in the supplementary methods) that the sample should be smaller than the FOV (186 µm) in order to have quantitative results (" The field of view must be larger than the size of the capillary to include an air region at both sides of the sample, which is needed for successful tomographic reconstructions and for quantitative contrast.").
It is mentioned in the first paragraph of the "result and discussion" section that the particles size of the sample PC-52.5 for PXCT study are finer than the sample described in the table S3 and used for the lab measurements (XRD, tomography…). How is it done? What is the impact on the comparison of the results between the different measurements?
The w/c ratio value for the sample used for PXCT measurements differs from 0.4 to 0.5 when described in the SI file, in situ multicontrast X-ray tomographic studies of cement hydration and method sections.
What are the units in Table2 ?

In figure 2:
- In b, it can be seen that the images of the Lab-uCT scan are more blurred at 93h than at 19h. Why ? Why does the analysis performed in Figure S5 not show the same tendency?
- On the contrary, Figure S7 clearly shows a degradation on the spatial resolution that is not observed by eye on the images.
- It is concluded that the resolution is estimated at two pixels (How?). It means that the resolution of the PXCT study is 374 nm. Then, how representative and trustable are the values given in figure S13 –Figure S15 ?
- Looking at the figure c: Can you link the difference of the grey-value in the diagram of lab-uCT and syn-uCT to the different behaviour of the two different cements ?
- There is a comparison between the lab-uCT diagram and the PXCT one. What is the abscissa axis label for the lab-uCT ? I understood that it was grey-value. If yes, what is the link to compare grey-values of absorption tomography to electron density obtain by PXCT ?
- Is the diagram of figure 2c the same than Figure S10? Are they representative of the same sub-volume ? Is "the largest possible volumes without including the glass capillary walls" is equivalent to the ~1×10 5 µm3 VOI mentioned in the "tomographic data analysis section" of SI for the PXCT study?

Looking at the spatial resolution analysis:
How many interfaces have been studied as in figures S2-3-4 to determine the resolution estimations? What is the standard deviation? Can the calculation linked to the figure s5-s6-s7 be detailed? How the resolution values are deduced from the curves?

Are the volumes used to determine the data of Table S7 and Figure S10 equal to the VOI?
It can be seen that there is a difference between the theoretical electron density of the components and the measured one. How do you explain the difference? Why did you choose to use the theoretical value to indicate the different components in figure S10 ? Why is there no measured values for air, water and LDH ? Which electron densities have been used to train the machine learning for those phases?

Why the grey values of the 3D rendering in figure 4 are different from one-step to another?

How has been the etch pit growth rate evaluated?

At the beginning of page 6 it is mentioned the spatial dissolution rate of alite. Since alite, C3A and belite has been classified in the very same category for the segmentation, how is it possible to make the difference between them when looking at C-S-H gel shells. I guess that the belite particles are not surrounded by gel shells because the DoH is equal to zero in table S5 but what about the differentiation between C3S and C3A?
Do we have an idea of how many particles of alite <3um were present in the sample at the beginning of the experiment?

Is the figure 5b representative of the 19h step?

At the end of the page 9 and in figure 8, it is mentioned, "PXCT yields underestimated values for the DoH likely due to the limited scanned volume" and "These data are scattered for PXCT because the limited height of the studied cylinder yields a poor representative elementary volume for this feature". It is in contradiction with the conclusion given in page 4 "giving confidence to the relevancy of the nanoimaging results in spite of the limited amount of volume scanned to have submicrometer resolution". Can you give more info and comment on the representativeness of the volume scanned by PXCT?

What is the UCP volume mentioned in page 10?

How is it possible to link the results obtained from 2D figures 5 and S13 to S18 to the ones obtained with the 3D segmentation? Are the results giving the same spatial dissolution rate?

Can you specify what you mean by quantification in this sentence: "Etch-pit growth rate, ~40 nm/h, and coalescence have also been measured but better spatial resolution is required for etch-pit quantification"?
At the end of the " implications and outlook" paragraph it is written that " The current spatial resolution of in situ near-field PXCT, ~370 nm, can be improved by increasing the number of projections, without larger acquisition times" which, from my knowledge, is false. While in the supplementary info section it is reported and especially pointed out that "The resolution obtained, see subsection dedicated to the spatial resolution, was limited by the number of projections, which was chosen to have reasonable scan times".

Is the sample perfectly stable from one measurement to another? Is there a need to "realign" the volume from one-step to another? Is there a need for volume registration? If yes, how has it be done ?

Reviewer #3 (Remarks to the Author):

Major revision is needed.
This paper presents a method to observe the hydration process of cement using 4D nanoimaging. The idea is novel, but there are some problems:
[1]The literature should be updated, more literature should be in recent three years.
[2]In the Introduction, the disadvantages of the references should be summarized clearly to emphasize the importance of this work. The difficulties of 4D nanoimaging also need to be summarized.
[3]In Fig.7, the time selection is very strange."19h","47h","93h". what is the reason. The title of this paper focuses on the early hydration. why not select some early hydration points? for example, Non-contact multiple-frequencies AC impedance instrument for cement hydration based on a high-frequency weak current sensor.
[4]This paper is interesting, cement pastes are multi-phase materials. Some phases are overlapped with others in some localized regions. Some nano-scale C-S-H and CH may be mixed together. It is said that the intrinsic size of C-S-H is about 5 nm(doi.org/10.3390/fractalfract5020047). Therefore, in Fig.4 nanoimaging, C-S-H may not be identified in the scale bar 5 μm. Therefore, at least, the typical size of each phase during the cement hydration should be listed out from literature, so that reader can compare comprehensively.
[5]As we know, some commercial PCs have some mineral admixtures. What about the XRF results of these two commercial PCs in this work.
[6]Fig. 3. Left figure is terrible. We can not identify which is which. It is only black and while.
[7]From Fig.7, the samples used in PXCT have serious carbonation. However, other samples do not have such carbonation. Besides, in Fig.7, how do authors identify the different kinds of C-S-H gels. Is it from AFM test according to porosity or NMR according to silicate calcium chain(doi.org/10.1016/j.conbuildmat.2020.118807 & doi.org/10.1016/j.measurement.2021.110019)

[8]In Fig.6,authors claim they can monitor the evolution of water porosity (dark-grey) to air porosity (black). Does it mean that water can be distinguished by near field PXCT? As I know, only neutron can examine the presence of water.
[9]In Fig.8,PXCT test results seem that C4AF content does not change much. It is not reasonable. Common sense tells us that the hydration rate is C3A > C3S > C4AF > C2S.

Reviewer #4 (Remarks to the Author):

A superbly presented, detailed study of cement hydration using various X-ray methods. I would recommend a review by someone expert in the cement hydration field, since I cannot comment on the impact of the results from the point of view of the application. What I can say is that the ptychographic imaging is a significant real-world demonstration of the near-field approach and, to my mind, represents the current state-of-the-art.

I have no issue recommending the article for publication, subject only to minor improvement of the English - which although always comprehensible could do with a proof-read.

Malaga, 7th of March, 2023

Response to reviewers document. Reference **NCOMMS-22-47460-T**
Title. "**4D nanoimaging of early age cement hydration**"

To help the readability and understanding of this revision, our answers are highlighted **in green** in the response to reviewer's letter and the changes are highlighted **in blue** in the revised version of the manuscript and in the S.I. file.

Reviewer #1 (Remarks to the Author):

The strength of this study, in my opinion, is in the exploration of a new nanoimaging technique, PXCT, to study the early hydration of Portland cement. With the unprecedented spatial resolution and contrast of PXCT, in situ identification of the evolution of various mineral phases, the C-S-H gel shells, etch pits, water pores and air pores, etc. became possible, hence the corresponding cement dissolution and precipitation processes at early ages associated with them was studied, and qualitative and quantitative results were obtained. The results are of potential interest to researchers working in X-ray computerized tomography and could illustrate a new characterization direction for the cement-based materials community.

The approach, data analysis and interpretation are valid, comprehensive and correct, and the evidence presented justify the conclusions. The literature is adequately cited. The clarity and accessibility of the text is good, and the results have been provided with sufficient context and consideration of previous work.

Author reply: Many thanks for acknowledging the main contributions of this work.

There are several issues however that I think should be clarified to help improve the work.

1.1. In the manuscript, it is said "In situ near-field data were taken as detailed in methods……. radiation damage cannot be discarded but it is small, if any. (Page 5) " "Time resolutions of ~1 h will open the way to accurately study the processes in the acceleration period. However, in these cases, radiation damage could be an issue if the total dose is not kept low. (Page 12)"

Will radiation damage affect the visualization results of the evolution of water porosity towards air porosity with time? In addition, migration of C-S-H gel was observed. Is it possible that this was also affected by radiation damage? How will the effect of radiation damage be considered in the future research with higher time resolution?

1.1. Author general reply: With the data currently available, we can only speculate on these interesting questions. It is known that the radiolysis of water in cement pastes yields, in a first stage, electrons and H_2O_2. After a cascade of reactions, the identified products (under gamma irradiation) are H_2 and calcium peroxide, i.e. $CaO_2{\cdot}8H_2O$ [see for instance, Bouniol and Aspart, Cement and Concrete Research (1998) "Disappearance of oxygen in concrete under irradiation: the role of peroxides in radiolysis"]. There are many papers dealing with gamma-irradiation of mortars and concretes but we are not aware of any investigation dealing with the radiation damage mechanism by 'mild' X-ray irradiation, that it does not necessarily need to be identical.

1.1. Author reply-a: We do not think that possible radiation damage will significantly modify the water porosity towards air porosity evolution. However, at this stage, this is a speculation that we prefer not to include in the revised version of the manuscript.

1.1. Author reply-b: C-S-H migration (dissolution and re-precipitation) has been observed in some small volumes/regions of the sample and we think this is due to local under/over saturation fluctuations rather than radiation damage. Unfortunately, we do not have data to firmly establish this point. More high-resolution imaging studies are required.

1.1. Author reply-c: Higher time resolution does not necessarily imply higher doses (and therefore larger radiation damage). For instance, sparsity techniques can be coupled to PXCT in order to decrease the overall acquisition time for the whole series by 90% [Gao et al., *Sci. Adv.* 7, eabf6971 (2021)]. Another approach could be to use ML for the reconstruction and denoising of datasets collected with (much) less X-ray dose [Hendriksen, et al., *Sci. Rep.* 11, 11895 (2021)].

The two key important points are now addressed in the revised version on page 14: "… Higher time resolution does not necessarily imply higher doses and therefore possibly larger radiation damage. For instance, sparsity techniques could be coupled to PXCT in order to decrease the overall acquisition time for the whole series by as much as 90%, as recently reported[64]. Another approach could be to use machine learning/deep learning for denoising of datasets collected with much less X-ray dose[65]. On the other hand, gamma irradiation of Portland pastes, mortars and concretes is known to produce water radiolysis finally leading to H_2 microbubbles and

calcium peroxide, $CaO_2 \cdot 8H_2O$[66]. Therefore, the signatures of these species should be monitored for studies with high X-ray doses.…" Three new references have been added.

1.2. The evolution of water porosity towards air porosity with time was observed around some Alite grains. How will this affect further hydration of Alite and etch pits growth when there is no water around?

1.2. Author reply: As soon as there is no contact with water, alite hydration stops. This can be seen in Figs. 5 and 6 and also in some figures in the S.I. However, with the data at hand, it is not possible to know if later-age water diffusion could re-wet some alite grain, and hence, hydration could progress. This is the reason we prefer not to speculate too much about this. In any case, this feature is now explicitly stated in the manuscript in the caption of Fig. 6 by adding "... Moreover, alite hydration also stops as soon as air porosity (pore drying) develops on the surfaces of the anhydrous grains, see red rectangles...". Figure 6 has been consequently updated with the corresponding red rectangles.

1.3. In the manuscript, it is said "The hollow regions of the Hadley grains are filled with water at 19 and 47 h but dried at 93 h, see enlarged pictures to the right. This illustrates that most of the capillary pores with sizes larger than ~1 μm are already water emptied at 93 h of hydration, see bottom right. (Figure S19)", "The enlarged views (bottom) show the evolution of porosity within the paste, where several pores of sizes smaller than ~2 μm are dried (red arrows) at 93 h but other larger, pores keep filled with water (blue arrows). (Figure S23)"

Is there a contradiction between those two conclusions, for the pores to be empty at 93 h, the former is >1μm and the latter is <2μm? Does the water migrate randomly?

1.3. Author reply-a: We do not think that there is a contradiction between the highlighted observations. Our interpretation is the importance of heterogeneity, which is key in cement hydration when analysed with enough spatial resolution and contrast. Just in Fig. 6, panel b, it can be directly seen that at 47 h, a pore of about 1 μm size is dried, but being very close to two larger water-filled pores, of sizes larger than 2 μm. At first sight, this seems to contradict Kelvin-Laplace equation that relates the relative humidity (RH) to the size of the dried pores. This implies that the pores are emptied of water from largest to smallest sizes as hydration progresses. This is indeed correct in the absence of impediments for water diffusion (which is not the case as C-S-H gel is a barrier to diffusion) and if the RH is constant within the paste, which is also not held. For instance, in regions where ettringite crystallizes, consuming a lot of water, the RH drops more than in other regions where only C-S-H/portlandite precipitates, which have lower water contents. This has been clarified in the caption of figure 6, b-panel, by adding the following statements. "… It is noted that at 47 h, a tiny pore of about 1 μm size is already dried, but being very close to two larger water-filled pores, of sizes larger than 2 μm. This observation remarks the heterogeneity in cement hydration. It can be deduced that the relative humidity is not constant, at a given time, through the sample. This is due to a set of factors including the barriers to water diffusion and the crystallization/precipitation of different hydrates with quite different water contents, for instance ettringite and portlandite...".

1.3. Author reply-b: We do not have enough data to model/deal with the migration of water. This is indeed a very interesting issue that will be treated when we collect a major number of tomograms at different ages.

1.4. The water to cement ratio is relatively higher near the capillary wall than that in the center. In Figure S27, wall effect in the 19h capillary tube sample could be observed. Will the degree of hydration of cement particles of the same size be affected by wall effect at different locations? It should be addressed in the manuscript.

1.4. Author reply: This is a quite important observation that was not treated in the submitted version. The 'wall effect' –the increased cement paste content near the wall of the container respect to the large aggregate particles in mortars and concretes– is well known (in mortars and concretes) and it has been extensively studied by numerous techniques including electron microscopy and synchrotron microtomography. The 'wall effect' in pastes, where water is partly segregated towards the wall of the capillary, has also been reported but it has been less studied. We have addressed the reviewer's comment by adding the following set of sentences on page 11, and the corresponding two new references. "… It seems that at 19 h, the free water is preferentially located close to the walls of the capillary. This could be related to the 'wall effect' well known in mortars and concretes, where the cement paste content is slightly higher near the wall of the container respect to the larger aggregate particles which are preferentially arranged towards the centre. This feature, and its implications in the interfacial transition zone, has been extensively studied by numerous techniques, including synchrotron microtomography, see for example[62]. For cement pastes, higher porosity near the capillary wall has been observed by synchrotron microtomography.[24] For a water-rich alite paste, wall effect was clearly observed by PXCT where the resulting C-S-H gel had higher water content near the capillary wall.[63] In order to quantitatively study this feature, the scanned capillary was divided into two volumes, a central cylinder with half of the radius and the outer region up to the glass capillary wall. The mean electron densities were computed, but the voxels with electron density smaller than 0.24 $e^{-}Å^{-3}$, air porosity, were not included in order to minimise any bias due to the shrinkage / pore

drying. The results for the centre volume were 0.614, 0.618 and 0.617 $e^{-}Å^{-3}$ for the 19, 47 and 94 h datasets, respectively. The corresponding mean electron density values for the outer region were 0.608, 0.610 and 0.601 $e^{-}Å^{-3}$. The 1 % difference between the two regions at 19 h is quite small but not negligible. Hence, the degree of hydration could slightly be a function of the horizontal position of the particles...."

Two new references have been added:
(62) *Energy Procedia* **114**, 5109–5117 (2017) (63) *Langmuir* **31**, 3779–3783 (2015)

Reviewer #2 (Remarks to the Author):

In this manuscript, the authors report the study of the early stage of cement hydration using mainly near-field ptychographic X-ray computed tomography. They provide a unique combination of spatial & temporal resolution + field of view. It allows the determination of quantitative values for dissolution rates and etch-pit growth rates. A comparison with data obtained by lab and synchrotron X-ray micro-tomography is also proposed. The paper shows an extended collection of data using state of the art technique and an interesting 3D data analysis based on machine learning process. Nevertheless, the manuscript shows some incoherencies and approximations, the results are not sufficiently described and discussed, especially the ones reported in the abstract. Thus, I cannot support this work for publication in Nature communications in its present form.

Author reply: thanks for your general comment which explicitly acknowledges the key contribution of this work "… They provide a unique combination of spatial & temporal resolution + field of view. …".

Some specific comments and remarks linked to my previous general comment:

2.1. For the PXCT study, the size of the capillary used is different between the different sections and figures 160 µm vs 200 µm. This information is important. Indeed, it is highlighted (in the supplementary methods) that the sample should be smaller than the FOV (186 µm) in order to have quantitative results (" The field of view must be larger than the size of the capillary to include an air region at both sides of the sample, which is needed for successful tomographic reconstructions and for quantitative contrast.").

2.1. Author reply: We thank the reviewer for allowing us to clarify this issue, which is very important. The glass capillary has a nominal diameter of 200 µm, however it is not fully uniform in its length. In the imaged vertical region, it has a thickness of 160 µm. Therefore, it was scanned with a FoV of 186 µm in order to have more than 10 µm of air outside the capillary, which is needed as a reference for quantitative phase imaging. This is now explicitly stated in the method section of the main manuscript. On page 15: "... introduced in a glass capillary of 200 µm of nominal diameter..." and "... The thickness of the capillary in the imaged region was 160 µm. Therefore, it was scanned with a FOV of 186 µm in order to have more than 10 µm of air outside the capillary, which is required for quantitative phase imaging...".

2.2. It is mentioned in the first paragraph of the "result and discussion" section that the particles size of the sample PC-52.5 for PXCT study are finer than the sample described in the table S3 and used for the lab measurements (XRD, tomography…). How is it done? What is the impact on the comparison of the results between the different measurements?

2.2. Author reply: We now are aware that our wording was misleading. We have used two PCs, one PC-52.5 and another PC-42.5. PC-52.5 was used for the PXCT study, and for the laboratory characterization: µ-CT, Rietveld quantitative phase analysis and calorimetry. The PC-52.5 employed in these measurements was identical. Indeed, PC-42.5, employed for the synchrotron µ-CT, has slightly larger particle sizes as measured in Fig. 1a, Table S3 and Fig. 8. This is clarified in the revised version by explicitly stating on page 3: "PC-52.5 was used for the PXCT and laboratory µ-CT imaging studies and the additional laboratory characterization. PC-42.5, with slightly larger average particle size, was used for the synchrotron µ-CT imaging study."

2.3. The w/c ratio value for the sample used for PXCT measurements differs from 0.4 to 0.5 when described in the SI file, in situ multicontrast X-ray tomographic studies of cement hydration and method sections.

2.3. Author reply: The nominal w/c ratio employed for the paste, that filled the capillary in the PXCT study, was 0.50. However, it is very challenging to control the w/c homogeneity within very thin capillaries. Therefore, the w/c ratio of the scanned volume in the PXCT study was measured and the value was slightly smaller. This is now fully clarified by adding on page 4 "… The nominal w/c mass ratio employed to fill the PXCT narrow capillary, 200 µm of nominal diameter, was 0.50, see methods. However, it is very difficult to accurately control the w/c ratio in very thin capillaries. Therefore, the w/c ratio of the scanned volume for the PXCT measurement was measured as previously published[46] and detailed in a subsection of the S.I. The w/c ratio of the scanned volume in the PXCT study was 0.41.".

2.4. What are the units in Table 2?

2.4. Author reply: The units are wt%, and this is corrected in the heading of Table S2.

2.5. In figure 2: - In b, it can be seen that the images of the Lab-uCT scan are more blurred at 93h than at 19h. Why? Why does the analysis performed in Figure S5 not show the same tendency?

2.5. Author reply: The FSC for laboratory microtomography, shown in Fig. S5, does not indicate higher degradation of the spatial resolution at 93 h. This is a direct observation. Fig 2b (laboratory data) shows a change which is not blurring but the consequence of hydration. At 19 h, the image has more free water and anhydrous components, hence it has higher contrast. At 93 h, the consumption of water to give hydrated phases results in a poorer contrast between them and the unhydrated phases, which may appear as a blurring effect.

2.6. On the contrary, Figure S7 clearly shows a degradation on the spatial resolution that is not observed by eye on the images.

2.6. Author reply: We thank the reviewer for allowing us to clarify this issue. The spatial resolution, as measured by FSC, for the 47 and 93 h tomograms, i.e. 470-500 nm, is slightly poorer than that of the 19 h, 430 nm. This was very likely due to the employed scanning step size that was 6 µm for the 19 h tomogram (resulting in 3h 55 min of total acquisition time), and 7 µm for the other two tomograms (resulting in 3h 6 min of total acquisition time). This was detailed in the experimental section, but now we understand that this was not enough. Therefore, this is now clarified in Figure S7 caption by adding "The slightly better spatial resolution measured for the 19 h tomogram is very likely due to the smaller scanning step size, i.e. 6 µm, and the corresponding larger acquisition time, i.e. 3h 55 min. The scanning step size for the other two tomograms was 7 µm, yielding 3h 6 min of acquisition time.".

2.7. It is concluded that the resolution is estimated at two pixels (How?). It means that the resolution of the PXCT study is 374 nm. Then, how representative and trustable are the values given in figure S13 –Figure S15?

2.7. Author reply-a: We thank him/her for allowing us to clarify this point about the spatial resolution which is indeed very important. Be aware that this point is intimately linked to the point 2.11, below. We acknowledge that this point was not treated with the required depth in the submitted version. We have carried out further studies to characterise this key feature: Now in the revised version "… The spatial resolution was characterised by two approaches as recently reported[52]. The procedures are thoroughly detailed in Supplementary Information (SI). On the one hand, the spatial resolution can be determined by the edge sharpness across selected interfaces. A point spread function (PSF) used to determine the spatial resolution of the images as ISO/TS 24597 defines the Gaussian radius of the PSF as the resolution, which equals a change between 25 %–75 % grey value along the studied interfaces.[38] The spatial resolutions, determined by this approach, were 250(25) nm, 264(25) nm, 272(34) nm, 748(19) nm and 2.21(17) µm, for PXCT-19h, PXCT-47h, PXCT-93h, Syn-µCT and Lab-µCT datasets, respectively. As examples of this procedure, Figures S2-S4 display line profiles of sharp interfaces between high (i.e. alite) and low density (i.e. porosity) components within the capillaries. On the other hand, Fourier-shell-correlation (FSC)[53] has also been employed to estimate spatial resolution. Figures S5-S7 displays the FSC traces for the three imaging modalities. The agreement between both approaches is satisfactory for Syn-µCT and Lab-µCT, but not for PXCT. The worse spatial resolution estimated by FSC for PXCT is very likely due to the low number of projections, i.e. 420, which make the subtomograms employed in the FSC calculation severely undersampled." Reference 52 has been added: (52) *Nat. Nanotechnol.* **15**, 356–360 (2020).

2.7. Author reply-b: Moreover, we have included a full new subsection in S.I. which reads:

"Spatial resolution analysis.

The spatial resolution was characterised by two approaches as recently reported[17]. On the one hand, it can be determined from the grey-value changes in line profiles through the edge sharpness of the interfaces. A point spread function (PSF) used to determine the spatial resolution of the images as ISO/TS 24597 defines the Gaussian radius of the PSF as the resolution, which equals to a change between 25 %–75 % grey value along the studied interfaces.[18] Here, a common interface present in the three imaging modalities has been selected for the line profiles: the glass capillary wall – air (i.e. exterior of the capillaries). We have measured 25 interfaces in every tomogram, which allowed us to determine the average spatial resolution and its associated standard deviation. Moreover, as examples, Figures S2-S4 display line profiles of sharp interfaces between high (i.e. alite) and low density (i.e. porosity) components within the capillaries. The spatial resolutions, determined by this approach, were 250(25) nm, 264(25) nm, 272(34) nm, 748(19) nm and 2.21(17) µm, for PXCT-19h, PXCT-47h, PXCT-93h, Syn-µCT and Lab-µCT datasets, respectively.

On the other hand, FSC plots[5] have been also computed. The traces are displayed in Figures S5-S7 giving spatial resolution values of 430 nm, 470 nm, 500 nm, 650 nm and 1.9 µm, for PXCT-19h, PXCT-47h, PXCT-93h, Syn-µCT and Lab-µCT datasets, respectively. Moreover, the FSC trace for PXCT-19h shows a smooth decrease in the 0.0-0.2 spatial frequency range, which is likely due to the hydration of cement during the 4-hour measurement. As expected, this behaviour is not shown at later ages.

It should be noted that the agreement between the spatial resolution results between the edge sharpness approach and FSC method is satisfactory for Syn-µCT (750 vs. 650 nm) and Lab-µCT (2.2 vs.1.9 µm) datasets. However, the agreement between these two approaches is not good for PXCT (for instance, 250 vs 430 nm at 19 h). The poorer resolution estimated by FSC can be explained because the angular sampling is very tight, i.e. 420 projections, so the two employed subtomograms in the FSC, each of 210 projections, were significantly undersampled compared to the number of voxels across the diameter of the sample. This means that the correlation between two such undersampled tomograms can give a low estimation of the spatial resolution. This feature is not observed for Syn-µCT and Lab-µCT as the total number of projections were 6000 and 1637, respectively. In other words, the subtomograms with half the number of projections were not undersampled for these two imaging modalities."

2.7. Author reply-c: In our opinion, we can trust the results shown in Figures S13-S15 as these features have dimensions 400-500 nm, significantly larger than the spatial resolution of PXCT study, which is determined as ~250 nm, see just above.

2.8. Looking at the figure 2c: Can you link the difference of the grey-value in the diagram of lab-uCT and syn-uCT to the different behaviour of the two different cements?

2.8. Author reply: It is not straightforward to link the different behaviour of PC-52.5 in Lab-µCT and PC-42.5 in Syn-µCT in Figure 2c because the Paganin phase retrieval is highly sensitive to the initial porosity. However, the expected behaviour: faster reactivity of PC-52.5 at early ages than PC-42.5, because of the finer particle sizes, is beautifully shown in Figure 8 b. As dictated by the particle sizes and as measured by calorimetry, PC-52.5 reacts faster between 19 and 47 h and then very little from 47 to 93 h, see Fig. 1b panel. This is clearly shown in the cumulative volume traces from Lab-µCT, see Figure 8 (top). Conversely, from calorimetry, PC-42.5 reacts slower between 19 and 47 h but it keeps reacting between 47 to 93 h, see Fig. 1b panel. This is evident in the cumulative volume traces obtained from Syn-µCT, see Figure 8 (intermediate). This was discussed in the segmentation subsection of the manuscript.

2.9 There is a comparison between the lab-uCT diagram and the PXCT one. What is the abscissa axis label for the lab-uCT? I understood that it was grey-value. If yes, what is the link to compare grey-values of absorption tomography to electron density obtain by PXCT?

2.9. Author reply-a: Yes, the abscissa axis label for lab-µCT is "grey-value". This is corrected in the revised version of the manuscript.

2.9. Author reply-b: It is not possible to quantitatively link the grey-values in the lab-µCT and the electron density in PXCT. The electron density values in PXCT are related to the imaginary part of the refractive index of every component. This relationship is quantitative but some nuances should be taken into account, such as partial volume effects and that amorphous phases and solid solutions have (slightly) variable compositions and hence, electron density values. Conversely, the grey-values in Lab-µCT are related to the attenuation coefficient of every component (i.e. the real part of the refractive index). Moreover, the relationship between grey-values and the attenuations is not quantitative because the polychromatic nature of the laboratory radiation. This has been clarified in the revised version by adding on pages 4-5"… The grey-values in the Lab-µCT study, see Fig. 2c (top panel), are related to the attenuation coefficients of the components in this PC-52.5 paste, but the relationship is not quantitative due to the polychromatic nature of the employed radiation. Conversely, the electron density values obtained for the same paste by PXCT are quantitative. Therefore, the grey scales in the Lab-CT and the electron densities in the PXCT datasets cannot be directly related as they derived from the imaginary and the real part of the refractive index of every component.".

2.10. Is the diagram of figure 2c the same than Figure S10? Are they representative of the same sub-volume? Is "the largest possible volumes without including the glass capillary walls" is equivalent to the ~1×10 5 µm^3 VOI mentioned in the "tomographic data analysis section" of SI for the PXCT study?

2.10. Author reply: Yes, the VOI were exactly the same and as big as possible without incorporating the glass capillary walls. There was a problem with the colours of the different traces in Fig S10, to be consistent with the main text, and this is now corrected. The revised figure S10 has the 93 h trace in green.

2.11. Looking at the spatial resolution analysis: How many interfaces have been studied as in figures S2-3-4 to determine the resolution estimations? What is the standard deviation? Can the calculation linked to the figure s5-s6-s7 be detailed? How the resolution values are deduced from the curves?

2.11. Author reply: For the reported number, we have studied 25 interfaces for every type of imaging modality. The average values and the associated standard deviations are now given, see point 2.7 above. The calculations are fully detailed now in the S.I.

2.12. Are the volumes used to determine the data of Table S7 and Figure S10 equal to the VOI?

2.12. Author reply: We thank the reviewer for allowing us to clarify this. The VOI used to obtain Figure S10 is the biggest possible volume leaving out the capillary. However, for Tables S7 and S8, the measured electron densities for the different phases/components are carried out for the large available particles. This was explicitly stated at the bottom of Table S8 but not in Table S7, which was misleading. This has been corrected by adding the information at the bottom of Table S7. " # Electron densities, from particle picking, were obtained by the average of 10 cubes for the capillary; 5, 4, 5 and 6 grains for portlandite, calcium carbonate, alite and belite, respectively."

2.13. It can be seen that there is a difference between the theoretical electron density of the components and the measured one. How do you explain the difference? Why did you choose to use the theoretical value to indicate the different components in figure S10 ? Why is there no measured values for air, water and LDH ? Which electron densities have been used to train the machine learning for those phases?

2.13. Author reply-a: We thank the reviewer for allowing us to clarify this point which was not dealt with in the original submission. The differences between the theoretical electron densities and the measured ones are mainly due to partial volume effects. This is now explicitly stated in the revised version on pages 6-7 "… The differences between the theoretical electron densities and the measured ones are mainly due to partial volume effects. For instance, portlandite, i.e. $Ca(OH)_2$, has a theoretical electron density value of 0.69 $e^-Å^{-3}$. The measured values at 19 and 93 h were 0.62(2) and 0.651(5) $e^-Å^{-3}$, see Table S7. These numbers are 6-10% smaller than the theoretical one, with the difference being higher than the errors of the measurements, which are estimated in 2-3%[46,54]. This difference is very likely due to the presence of residual water porosity below the spatial resolution of the measurements, which we refer to partial volume effects." Reference 54 has been added:
(54) *Phys. Rev. B* **85**, 020104 (2012).

2.13. Author reply-b: We prefer to indicate the theoretical values of electron densities in Fig. S10 because they are free of partial volume effects and they can be used in future works with higher spatial resolution and therefore, where the implications of the partial volume effects will be smaller.

2.13. Author reply-c: Concerning the measured values for air, water and LDH. They are now included in Table S7. "… Moreover, 5 cubes at 19 h gave the reported measured electron density for capillary water. Similarly, 5 cubes at 93 h were computed to obtain the value for air. Finally, the electron density of LDH (low density hydrates) was measured at 93 h in 5 cubes yielding 0.56(1) $e^-Å^{-3}$ that it corresponds to ettringite and/or C-S-H as they cannot be distinguished."

2.13. Author reply-d: Concerning the electron density values used to train the machine learning. It should be noted that we did not use a single value of electron density but a range of approximately 5% of the measured electron density value for the initial classification and training of the different components. Afterwards, based on the obtained results, some voxels were relabelled and further training was carried out based on the electron density values and on the morphology of the components. We acknowledge that this information was not given and this is now corrected in the revised version of the S.I. by adding "… The initial classification was based on the electron densities with a variation of ~5% of the measured values, from selected volumes, which are given in Table S7."

2.14. Why the grey values of the 3D rendering in figure 4 are different from one-step to another?

2.14. Author reply: The change in grey values between each step in Fig 4b is caused by the "diffuse light" effect used for 3D rendering. We have to note that the 3D rendered views do not show exactly the grey values (or electron densities) but they are affected by the visualization features. This is now clarified in the figure caption. "… These 3D rendered views do not show exactly the electron densities as they are affected by visualization features like the lighting source."

2.15. How has been the etch pit growth rate evaluated?

2.15. Author reply: We acknowledge that the procedure for etch pit growth rate estimation/evaluation was not detailed and this is now corrected two-fold. We have added a small subsection in the S.I. detailing the procedure and its limitations. Furthermore, the results have been updated in the main text. This point is also very much related to the point 2.22, from this reviewer, see below. It is noted that this is not a full quantitative determination but an estimation, as the spatial resolution of our imaging study, ~250 nm, is not good enough for a thorough study of these tiny features.

Now in the S.I.: **Etch pit growth rate evaluation.**

The estimation of the etch-pit growth rate was based on the analysis of 27 etch-pits from 5 different large alite grains. It is noted that the etch-pits have irregular 3D shapes and therefore, for its spatial dissolution rate estimation, some simplifications were undertaken. Moreover, the spatial resolution of this PXCT work, ~250 nm, is limited for accurate analyses. Therefore, we consider this approach as an estimation. Firstly, etch pits were visually selected from grains with sizes larger than 10 µm. Secondly, their overall shapes were compared in two

hydrating steps. Then, two envelopes from pixels with at least 90% of the electron density of alite were developed. The estimated/calculated distance (in pixels) was computed between these edges for the deepest perpendicular length. These values were converted to dissolution rate by taking the ratio with respect to the time between measurements. The result for the analysis between 19 and 47 h datasets gave 6.1 pixels of average distance which is equivalent to 41(29) nm/h. There was large variability in the rates, the fastest being 110 nm/h and the slowest being 10 nm/h. From this investigation, it is not possible to know if this large variability comes from the heterogeneity in the defects within these regions, or if other variables like the spatial resolution of this work and the local water-to-cement ratio variations are also playing important roles. More imaging studies are necessary to establish this. The very same 27 etch-pits were also analysed between 47 and 93 h datasets. In this case, the etch-pit growth rate was slower 7 nm/h, showing that the water diffusion is already limiting hydration at four days.

Now, in the manuscript on page 7: "… The etch-pit growth rate was estimated, as detailed in S.I., from the analysis of 27 dissolving regions in five alite grains. The resulting rate, between 19 and 47 h, was 41(29) nm/h. The etch-pit growth rate between 47 and 93 h was slower with a large variability, 7(8) nm/h, showing that the water diffusion is already limiting hydration."

2.16. At the beginning of page 6 it is mentioned the spatial dissolution rate of alite. Since alite, C3A and belite has been classified in the very same category for the segmentation, how is it possible to make the difference between them when looking at C-S-H gel shells. I guess that the belite particles are not surrounded by gel shells because the DoH is equal to zero in table S5 but what about the differentiation between C3S and C3A?

2.16. Author reply: This comment is quite related to 2.21 below, both related to the C3S spatial dissolution rate. Here we clarify that, in the original submission, the spatial dissolution rate of alite was not determined from the segmentations but from the analysis of 22 surfaces of particles of different sizes. Firstly, C_2S particles were excluded because they do not have a C-S-H shell at 19 h of hydration. C_3A particles were also discarded as they have a smaller electron density, ~0.90 $e^-Å^{-3}$ instead of the ~0.95 $e^-Å^{-3}$ of alite particles. This is now clarified in the text by "Chiefly, the spatial dissolution rate of alite was determined from the study of the surface evolution of selected particles, see Fig. 5a and Figs. S13-S18, as examples. C_2S particles were identified and excluded from this analysis, because they do not have C-S-H shells at 19 h of hydration. C_3A particles were also recognised and discarded because of their smaller electron density values, i.e. ~0.91 $e^-Å^{-3}$, 5 % lower than that of alite. From 22 measurements along different surfaces, the dissolution rate between 19 and 47 h was 25(14) nm/h...".

2.17. Do we have an idea of how many particles of alite <3um were present in the sample at the beginning of the experiment?

2.17. Author reply: From the particle size distribution measurement by laser diffraction, we can estimate that ~20 vol% of PC has sizes smaller than 3 µm. Because the cement has 61 % of alite, the initial cement had about 12 vol% of alite with these particle sizes. Moreover, the scanned region of the capillary is filled with a paste containing a w/c mass ratio of 0.40. Due to the large difference in densities (water=1 g/cc and cement=3.12 g/cc) the capillary contained at the time of mixing, 56.1 vol% of water and 43.9 vol% of cement particles. Therefore, the alite volume at the beginning of the experiment with particle sizes smaller than 3 µm is estimated as ~5.3 vol%. As the scanned volume of paste was ~5 10^5 $µm^3$ (the total volume was 8.1 10^5 $µm^3$ but this included the glass capillary and the air) and it contained about ~26000 $µm^3$ of alite particles smaller than 3 µm. A back of the envelope calculation indicates that if all particles have 3 µm, and they have cubic shape, it should be around 1000 particles. Conversely, if all particles have 1 µm isotropic size, it should be around 26,000 particles. This coarse calculation agrees reasonably well with the segmented number of alite particles at 19 h of hydration with sizes between 1 and 3 µm, i.e. 1117 particles which come from partly hydrated larger ones, stated in the manuscript (given the number of approximations, and taken into account that all small particles are dissolved at early hydration ages). At this stage, we prefer not to include this calculation in the manuscript as all data to carry out this coarse estimation are in the paper. However, if the reviewer thinks differently, we could include this calculation in the supplementary information file.

2.18. Is the figure 5b representative of the 19h step?

2.18. Author reply: Yes, fully representative. We forgot to include that description in the figure caption. This mistake has been corrected by adding "… for the 19 h tomogram."

2.19. At the end of the page 9 and in figure 8, it is mentioned, "PXCT yields underestimated values for the DoH likely due to the limited scanned volume" and "These data are scattered for PXCT because the limited height of the studied cylinder yields a poor representative elementary volume for this feature". It is in contradiction with the conclusion given in page 4 "giving confidence to the relevancy of the nanoimaging results in spite of the limited amount of volume scanned to have submicrometer resolution". Can you give more info and comment on the representativeness of the volume scanned by PXCT?

2.19. Author reply: We do not think that there is a contradiction between these statements. In fact, it is highlighted from the very beginning "… in spite of the limited amount of volume scanned to have submicrometer resolution" We have also carried out Syn-µCT and Lab-µCT, because the scanned volume in PXCT is limited. It is explicitly stated in the experimental section, and visually in Figure 7, that PXCT only scans 30 µm in the vertical direction of the capillaries (meanwhile Syn-µCT and Lab-µCT scan 1000 µm). With large alite grains of about 20 µm, scanning 30 µm in the vertical direction is limited (although 160 µm was imaged in the transversal section of the capillary which allowed to scan many particles. Indeed, to image a larger volume, vertical dimension of about 60-100 µm would require about 7-9 hours per scan which may not allow to accurately study the hydration as important changes can occur during the acquisition time.

We have clarified this by adding the following set of sentences to the revised version on page 12: "… Finally, it should be noted that the scanned length in the vertical direction, 30 µm, for PXCT is limited taking into account that some alite grains with sizes of 20 µm, or slightly larger, are present in PC cements. This was mitigated by imaging 160 µm in the transversal direction. This type of experiment will benefit from imaging cylindrical volumes with 60-100 µm of height. However, with the current experimental procedure, this would lead to acquisition times larger than 7-9 hours and therefore changes due to hydration could take place during an acquisition. Procedures for faster data collection are being explored and some are discussed in the next section."

2.20. What is the UCP volume mentioned in page 10?

2.20. Author reply: This is the total volume of the anhydrous cement particles at 19 h as determined from PXCT. We now realize the sentence was not fully clear and we have replaced on page 12 "… The groups contained 1117, 204, 61 and 20 particles, respectively, and the corresponding percentages with respect to the UCP volume were 5.4, 12.9, 21.5 and 60.2%." by "… The groups contained 1117, 204, 61 and 20 particles, respectively. The corresponding volume percentages with respect to the overall anhydrous cement particle volume at this hydration age, were 5.4, 12.9, 21.5 and 60.2%.".

2.21. How is it possible to link the results obtained from 2D figures 5 and S13 to S18 to the ones obtained with the 3D segmentation? Are the results giving the same spatial dissolution rate?

2.21. Author reply: We thank the reviewer for allowing us to elaborate on this important result from the segmentation quantitative analysis point of view. Based on quantitative analysis derived from ML segmentation of the PXCT datasets (for the C_3S/C_2S class, dark brown colour code in the 3D visualization of Fig. 7), it is possible to derive an average spatial dissolution rate. We used mathematical morphology tools to retrieve the outer layer of the 19 h hydration and 47 h hydration segmented grain. Then, we computed the average distance between these outer layers for each grain, giving a mean value of 1.92 pixels (i.e. ~13 nm/h). This value is smaller than that obtained from 2D analysis for alite, 25 nm/h. However, it should be noted that in the segmentation analysis, alite and belite were classified together and therefore, the obtained spatial dissolution rate is underestimated as belite does not dissolve at early ages. Table S5, from the Rietveld analysis, indicates that the amount of belite is approximately half of that of alite during this stage. Therefore, the spatial dissolution rate can be corrected. The value, only for alite, would be close to 13/0.67 or 19 nm/h. This rate agrees relatively well with that obtained from the 2D analysis of 22 measurements, 25 nm/h, given the number of approximations which took place for both calculations. Now in the revised version on page 7: "… Moreover, this spatial dissolution rate can also be estimated from the segmentation results presented in the next subsection. Based on the quantitative analysis derived from Machine Learning (ML) segmentation of the PXCT datasets (for the C_3S/C_2S class, dark brown colour code in the 3D visualization of Fig. 7), it is possible to derive an average spatial dissolution rate. Mathematical morphology tools were used to retrieve the outer layer of the segmented grains at 19 and 47 h. Subsequently, the average distance between these outer layers was computed for each grain, giving a mean value of 1.92 pixels (i.e. ~13 nm/h). This value is smaller than that obtained from the analysis performed in 2D slices for alite, 25 nm/h. However, it should be noted that in the segmentation calculation, alite and belite were classified together and therefore, the obtained spatial dissolution rate is underestimated as belite does not dissolve at early ages. Table S5, Rietveld analysis results, indicates that the amount of belite is half of that of alite during this stage. Therefore, the spatial dissolution rate can be corrected. The alite spatial dissolution rate should be close to 13/0.67 or 19 nm/h. This value agrees relatively well with 25 nm/h, obtained from 22 measurements in 2D slices, given the number of approximations which took place for both calculations....".

2.22. Can you specify what you mean by quantification in this sentence: "Etch-pit growth rate, ~40 nm/h, and coalescence have also been measured but better spatial resolution is required for etch-pit quantification"?

2.22. Author reply: This point is related to that about etch-pit evaluation, 2.15. We acknowledge that the wording was somehow misleading. The etch-pit growth rate was/is an estimation, not an accurate measurement. In fact, due to this, we decided not to report a number in the abstract. Thus, "Etch-pit growth rate, ~40 nm/h, and coalescence have also been measured but better spatial resolution is required for etch-pit quantification" has been replaced by : "… The alite etch-pit growth rate between 19 and 47 h has been estimated as ~40 nm/h, which

decreases to ~7 nm/h in the 47 to 93 h interval. Moreover, etch-pit coalescence, the merging of different branches, has also been visually observed. However, better spatial resolution is required for a thorough etch-pit growth rate quantification."

2.23. At the end of the " implications and outlook" paragraph it is written that " The current spatial resolution of in situ near-field PXCT, ~370 nm, can be improved by increasing the number of projections, without larger acquisition times" which, from my knowledge, is false. While in the supplementary info section it is reported and especially pointed out that "The resolution obtained, see subsection dedicated to the spatial resolution, was limited by the number of projections, which was chosen to have reasonable scan times".

2.23. Author reply: Clearly, as previously stated there was a contradiction. This is very much related to point 1.1 above. The way to have better resolution (acquiring more projections) without increasing the dose too much (to avoid radiation damage) is to decrease the acquisition times. As stated in the answer to point 1.1-c the approach would be to collect data with faster acquisition times (worst signal-to-noise ratio) and to use ML for reconstruction and denoising of datasets. Alternatively, sparsity techniques can be coupled to PXCT, which is being implemented at cSAXS beamline. The text was revised as stated in point 1.1, above.

2.24. Is the sample perfectly stable from one measurement to another? Is there a need to "realign" the volume from one-step to another? Is there a need for volume registration? If yes, how has it be done?

2.24. Author reply: This is an important question that it requires a detailed answer. We acknowledge that the original submission did not contain the requested details. Furthermore, as there are three imaging modalities (ptychography, synchrotron microtomography and laboratory microtomography) the answer depends upon the employed technique. This has been addressed by adding the following information in the S.I. material:

"… Initially, the re-alignment of the data, when needed must be detailed.

For the PXCT, the capillary position was very accurate, as the capillary/holder system was mounted from the tray storage to the sample stage by the flOMNY gripper (robot). Hence, the angular orientation of the sample was maintained. The field of view of the sample was aligned carefully based on features visible in the 2D projections. The scanned regions with time were consistent within a few voxels and therefore no alignment between different acquisitions was required.

For the Syn-µCT, a mark was drawn on the sample holder and sample stage for the incident beam to minimise the initial incidence angular position variability. Before each scan, a projection was acquired as a reference for the next one in order to scan the same region. A minor manual registration was required, mostly rotations around x- and y-axes.

For the Lab-µCT, manual registration was required to align the different acquisitions. The process is described next. The capillary was considered as a cylinder and we manually made the cylinders vertical and centred in the reconstructed volume. The remaining rotation around the z-axis was visually done by superimposing distinguishable landmarks in the corresponding images.

Reviewer #3 (Remarks to the Author):

Major revision is needed.

This paper presents a method to observe the hydration process of cement using 4D nanoimaging. The idea is novel, but there are some problems:

Author reply: Many thanks.

3.1. The literature should be updated, more literature should be in recent three years.

3.1. Author reply: We thank the reviewer for this comment. We have included five new references (2020-2023), just to respect the maximum number of references, which in the guideline for submission is stated as 70. The revised version of this manuscript had already 69 references. Now in the introduction of the revised version "… In the last three years, important advances have been reported including: i) the automated correction for the movement of suspended particles at very early ages[34] which allowed to follow *in situ* PC hydration after water mixing[35]; ii) to follow the fast dissolution of plaster and the precipitation of gypsum[36]; iii) the simultaneous use of neutron and laboratory X-ray tomographies for *in situ* studying the microstructural changes of PC mortars on moderate heating[37]; and iv) the measurement of alite particle dissolution using fast synchrotron nano X-ray computed tomography[38,39]" The new references added are the followings (reference 35 was already included in the original submission):

(34) Vigor, J. E., Bernal, S. A., Xiao, X. & Provis, J. L. Automated correction for the movement of suspended particulate in microtomographic data. *Chem. Eng. Sci.* **223**, 115736 (2020).
(36) Seiller, J. *et al.* 4D in situ monitoring of the setting of α plaster using synchrotron X-ray tomography with

high spatial and temporal resolution. *Constr. Build. Mater.* **304**, 124632 (2021).
(37) Cheikh Sleiman, H., Tengattini, A., Briffaut, M., Huet, B. & Dal Pont, S. Simultaneous x-ray and neutron 4D tomographic study of drying-driven hydro-mechanical behavior of cement-based materials at moderate temperatures. *Cem. Concr. Res.* **147**, 106503 (2021).
(38) Li, X. *et al.* Direct observation of C3S particle dissolution using fast nano X-ray computed tomography. *Cem. Concr. Res.* **166**, 107097 (2023).
(39) Li, X., Hu, Q., Robertson, B., Tyler Ley, M. & Xiao, X. Direct observation of C3S particles greater than 10 μm during early hydration. *Constr. Build. Mater.* **369**, 130548 (2023).

3.2. In the Introduction, the disadvantages of the references should be summarized clearly to emphasize the importance of this work. The difficulties of 4D nanoimaging also need to be summarized.

3.2. Author reply-a: Concerning the disadvantages of the published work, we thank the reviewer since this helps to focus on the work we present in this manuscript. This was already treated in the introduction but we acknowledge that not with the required depth. Now in the revised version: "… In particular, hard X-ray synchrotron microtomography has not the required submicrometer spatial resolution neither sufficient component contrast[35,40], hard X-ray synchrotron nanotomography has not the required contrast between the components to be able to classify the hydrates[38,39] and soft X-ray synchrotron nanotomography has the contrast but it requires very large w/c ratios and very small fields of view which does not allow the hydrates to growth in relevant condition (i.e. confined space with low water-cement ratios)[32].".

3.2. Author reply-b: We think that the difficulties were already detailed in the introduction by stating the four (stringent) requirements that should be met simultaneously. To refer this to 4D imaging in a more obvious way, we have rephrased now this part on page 2: "…. However, none of these 4D imaging works combine the stringent four requirements needed for carrying out relevant contributions to the understanding of the mechanism(s) of Portland cement hydration at early ages: (i) water to cement mass ratio (w/c) close to 0.50, (ii) submicrometer spatial resolution, (iii) good contrast to be able to identify the different evolving components (more than eight), and (iv) relatively large scanned volume to allow hydration to progress with appropriate particle sampling, the particle sizes of commercial PCs have $D_{v,50} \in$ 10-20 μm." We prefer not to reiterate this message.

3.3. In Fig.7, the time selection is very strange."19h","47h","93h". what is the reason. The title of this paper focuses on the early hydration. why not select some early hydration points? for example, Non-contact multiple-frequencies AC impedance instrument for cement hydration based on a high-frequency weak current sensor.

3.3. Author reply: The selection of the hydration time was given by the availability of synchrotron beamtime that was shared with other nanotomographic study. On the other hand, there are several techniques that can help to characterise the overall water porosity evolution with time such as "Non-Contact Multiple-Frequency AC Impedance Instrument for Cement Hydration Based on a High-Frequency Weak Current Sensor; doi: 10.3390/act12010026" but they lack the submicrometer spatial resolution that is the focus of this work.

3.4. This paper is interesting, cement pastes are multi-phase materials. Some phases are overlapped with others in some localized regions. Some nano-scale C-S-H and CH may be mixed together. It is said that the intrinsic size of C-S-H is about 5 nm(doi.org/10.3390/fractalfract5020047). Therefore, in Fig.4 nanoimaging, C-S-H may not be identified in the scale bar 5 μm. Therefore, at least, the typical size of each phase during the cement hydration should be listed out from literature, so that reader can compare comprehensively.

3.4. Author reply: We fully agree with the reviewer's statement. This is also linked to the partial volume effects highlighted by reviewer 2 in his/her remark 2.13. We have clarified this by adding the following set of sentences to the text: "…It should be noted that individual C-S-H nanoparticles have sizes close to 5 nm[12,55] much smaller than the spatial resolution of this work, i.e. ~ 250 nm. Therefore, the C-S-H regions analysed here very likely contain other components like gel and capillary water porosities and interspersed calcium hydroxide. On the other hand, ettringite and portlandite particles have larger sizes, usually ranging 1-5 μm, and they can be imaged in the present work.[3] In any case, partial volume effect (the presence of components contributing below the spatial resolution of the measurements) is always taking place in cement pastes as some hydrates may have quite small particle sizes.[17]" We have also added the suggested reference:
(55) Tang, S. *et al.* Structure, fractality, mechanics and durability of calcium silicate hydrates. *Fractal Fract.* **5**, 47 (2021).

3.5. As we know, some commercial PCs have some mineral admixtures. What about the XRF results of these two commercial PCs in this work.

3.5. Author reply: Indeed, most commercial PCs have limestone in addition to the gypsum used as set regulator, this is also linked to the 3.7 point, below. The employed PCs are type I where only gypsum and limestone are added to the clinker and their contents lower than 5 wt%. The XRF, and the LoI, data were given in Table S1.

3.6. Fig. 3. Left figure is terrible. We can not identify which is which. It is only black and while.

3.6. Author reply: We have made an effort to clarify the message but the bottom-line feature cannot change: the relatively poor spatial resolution and contrast of synchrotron (propagation-based phase-contrast) microtomography when compared to ptychographic nanotomography. When inspecting the fine details at the same (high) magnification, synchrotron microtomography shows the relatively coarse voxel size with limited contrast. Figure 3 caption has been revised to detail the new views. Now in the revised version:

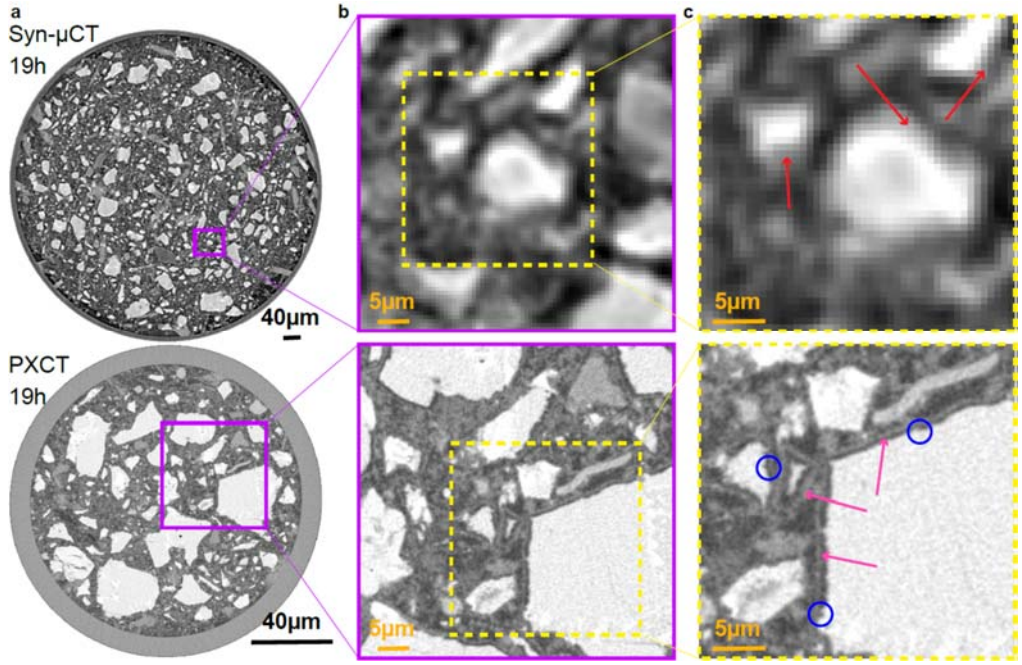

Fig. 3. Comparison of phase-contrast synchrotron tomography and ptychographic X-ray computed tomography. a, Selected orthoslices at 19 h for (top) Syn-µCT [voxel size: 650 nm, total scanned volume: 5.25 10^8 µm^3, overall acquisition time: 5 min], and (bottom) PXCT [voxel size: 186.64 nm, total scanned volume: 8.15 10^5 µm^3, overall acquisition time: 3 h, 55 min]. **b,** enlarged views of the highlighted regions (purple squares) in **a**, in order to illustrate the level of detail that can be observed with these imaging modalities. Every voxel in Syn-µCT image starts to be evident. **c,** Further enlarged views to illustrate the maximum level of detail that can be observed. (Top) The Syn-µCT image shows whitish particles (anhydrous cement particles) surrounded by hydrates (greyish voxels) which are highlighted by red arrows. (Bottom) The PXCT data, at the same magnification, shows a much higher level of detail. The C-S-H gel shells surrounding the alite particles are clearly visible (pink arrows). There is a water gap between the shell and the alite grain due to the inward dissolution of alite. Moreover, etch-pits on the surfaces of the alite particles are also visible (blue circles). The highest spatial resolution and better contrast of PXCT data allow visualizing submicrometre features of the dissolution-precipitation processes which are not visible in propagation-based Syn-µCT. Conversely, propagation-based Syn-µCT permits to scan much larger volumes in much smaller acquisition times, showing the complementary nature of both techniques.

3.7. From Fig.7, the samples used in PXCT have serious carbonation. However, other samples do not have such carbonation. Besides, in Fig.7, how do authors identify the different kinds of C-S-H gels. Is it from AFM test according to porosity or NMR according to silicate calcium chain (doi.org/10.1016/j.conbuildmat.2020.118807 & doi.org/10.1016/j.measurement.2021.110019)

3.7. Author reply-a: Related to carbonation. We do not agree with this statement. The samples have not serious carbonation. It is noted that the employed cements are commercial and these materials have normally 4-5 wt% of limestone addition. This was already shown in the cement mineralogical analyses, see Table S2, where PC-52.5 and PC-42.5 have 2.8 and 3.7 wt% of crystalline calcite, respectively. This is now clarified in the caption of Figure 7 by adding: "… This calcite comes very likely from the limestone addition to the Portland cement as quantified in the anhydrous material, see Table S2."

3.7. Author reply-b: We are aware that there are different C-S-H from the nano-mechanical point of view with different gel pore water contents. Unfortunately, with the spatial resolution and contrast currently available, we cannot distinguish them. From synchrotron microtomography we can distinguish hydrates with high mass/electron densities (portlandite, calcite, high-density C-S-H) from low density compounds (ettringite, AFm-type phases and low-density C-S-H). PXCT allows to distinguish calcite but it does not allow to distinguish high

density and low density C-S-H. This is now clarified in the caption of Figure 7 by adding: "… It is noted that with the quality of the data reported in this study (spatial resolution and electron density contrast), it is not possible to disentangle low-density from high-density C-S-H".

3.8. In Fig.6, authors claim they can monitor the evolution of water porosity (dark-grey) to air porosity (black). Does it mean that water can be distinguished by near field PXCT? As I know, only neutron can examine the presence of water.

3.8. Yes, PXCT can distinguish water from air, if the measurements are done to yield quantitative electron densities. This requires thin specimens surrounded by air. This is known since 2012: "Quantitative x-ray phase nanotomography, doi: 10.1103/PhysRevB.85.020104", where a sensitivity of about 0.02 $e^{-}Å^{-3}$ was demonstrated for the electron density contrast. The electron density of water is 0.33 $e^{-}Å^{-3}$, larger than that of air, i.e. 0.00 $e^{-}Å^{-3}$. This is clarified in the revised version ". It is underlined that PXCT readily distinguishes air and water porosities because of their difference in electron densities, 0 and 0.33 $e^{-}Å^{3}$, respectively; when the phase retrieval is carried out quantitatively[54].".

Obviously, we fully agree that neutron imaging is another technique that can disentangle water from air porosities. The key advantage of neutron imaging is clear, it can scan large volumes. However, it must also be noted that at a much worse spatial resolution compared to PXCT.

We have clarified this in the S.I. by adding "… PXCT provides 3D maps of the electron density of the specimen with quantitative contrast, the sensitivity being about 0.02 $e^{-}Å^{-3}$.[16] For attaining quantitative electron densities, the entire specimen must be included in the field of view, containing some empty space around it, which was the case in our measurements. Therefore, it is possible to easily distinguish air and water regions in the specimen, which have electron densities of 0.00 and 0.33 $e^{-}Å^{-3}$, respectively. Obviously, neutron imaging is the standard technique to disentangle water from air porosities. A key advantage of neutron imaging is its ability to can scan large volumes. However, it must also be noted that at a much worse spatial resolution compared to PXCT."

3.9. In Fig.8, PXCT test results seem that C_4AF content does not change much. It is not reasonable. Common sense tells us that the hydration rate is $C_3A > C_3S > C_4AF > C_2S$.

3.9. Author reply: The reviewer is right to point out a) the well-known hydration rate sequence, $C_3A \sim C_3S > C_4AF > C_2S$; and b) that C_4AF does not change much in our study. However, we do not consider this observation unreasonably for two reasons: i) C_4AF reactivity starts to take place mainly after about 2 days of hydration and our last measurement took place at 4 days (i.e. 93 h); and ii) the w/c ratio in the scanned volume was about 0.40. A low w/c ratio means less water available for the hydration of the phases with the slower kinetics, i.e. C_4AF. We have clarified this by adding the following statement in the figure caption. "… PXCT data shows that C_4AF hydrates little up to 93 h. This is likely due to the low w/c ratio in the scanned volume and its slow hydration rate.".

Reviewer #4 (Remarks to the Author):

A superbly presented, detailed study of cement hydration using various X-ray methods. I would recommend a review by someone expert in the cement hydration field, since I cannot comment on the impact of the results from the point of view of the application. What I can say is that the ptychographic imaging is a significant real-world demonstration of the near-field approach and, to my mind, represents the current state-of-the-art. I have no issue recommending the article for publication, subject only to minor improvement of the English - which although always comprehensible could do with a proof-read.

Author reply: Many thanks

REVIEWERS' COMMENTS

Reviewer #1 (Remarks to the Author):

The author has replied to all the issues and revised the manuscript accordingly. I recommend it for publication.

Reviewer #2 (Remarks to the Author):

First of all, I would like to thank the authors for their very detailed and precise answers. I acknowledge the work they have done to improve the manuscript and precise the methods used for the quantitative analysis of the images. I would recommend adding graphs detailing the large variability in the results of the etch-pit growth rate in the SI. I am happy to reconsider my previous decision and support this work for publication in Nature communications.

Reviewer #3 (Remarks to the Author):

Major revision is needed.
1) In Table S5, the content of Cc increases from 2.0 to 3.6 at 96h. obviously, the serious carbonation occurs, see the review comments 3.7
2) In Table S7, data of AFm and C-A-S-H are missing. As Ca/Si ratio of C-S-H is very close to 1.7, not 1.8. Do authors have data related to C-S-H with Ca/Si 1.7. C-S-H gels are glassy phases so their values are within a certain range in Table S7. What is the range? The electron density of C-S-H and CH are close to each other. In most cases, the hydrating pastes, C-S-H and CH are mixed together with porosity, and hard to be distinguished. Once C-S-H and CH can not be distinguished, 4D nanoimaging of hydration can not be achieved because they are occupied up to 80% volume of hydrates.
3) Some key points should be clarified. Raw clinker of cement is mixture. The microstructure of pastes includes time-evolving multi-phases with different multi-scale(nano-,meso-, and micro). Therefore, if PXCT enables to distinguish the amount and distribution of different phases, these phases should have “distinct” features in electron density derived from PXCT. Obviously, single test or measurement can not achieve this objective. Therefore, other test results and literature results should be carried out and compared to support the evidences in the manuscript. Please the review comment 3.7.

Malaga, 14th of April, 2023

Response to reviewers document. Reference **NCOMMS-22-47460A** (second revision)

Title. "**4D nanoimaging of early age cement hydration**"

Reviewer #1 (Remarks to the Author):

The author has replied to all the issues and revised the manuscript accordingly. I recommend it for publication.

Author reply: Many thanks.

Reviewer #2 (Remarks to the Author):

First of all, I would like to thank the authors for their very detailed and precise answers. I acknowledge the work they have done to improve the manuscript and precise the methods used for the quantitative analysis of the images. I would recommend adding graphs detailing the large variability in the results of the etch-pit growth rate in the SI. I am happy to reconsider my previous decision and support this work for publication in Nature communications.

Author reply-1: Many thanks.

Author reply-2: Concerning the etch-pit growth rate, we can only agree. Therefore, we have prepared a new figure, Fig. S13 with two particles showing the evolution of ten etch-pits. The remaining figures have been renumbered. Figure S13 and its caption are reproduced below.

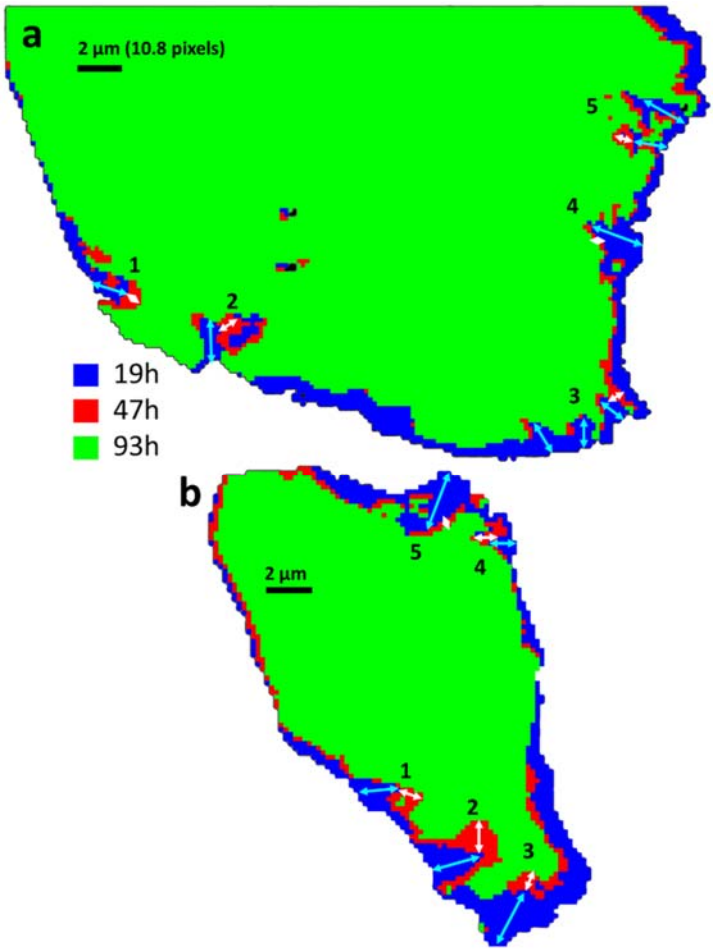

Figure S13. Overlay of the (2D-projected) alite segmented pixels during the hydration process to show the large variability in the growth rates of the etch-pits. **a,** five etch-pits corresponding to Figure 4 of the manuscript. **b,** five etch-pits corresponding to the Figure S11 of this S.I. Pale-blue arrows show size changes from 19h to 47h, meanwhile white arrows display the changes from 47h to 93h.

Reviewer #3 (Remarks to the Author):

Major revision is needed.

3.1. In Table S5, the content of Cc increases from 2.0 to 3.6 at 96h. obviously, the serious carbonation occurs, see the review comments 3.7.

Author reply: The initial PC had an average calcite content of 2.8 wt%, see Table S2, that when diluted with the water resulted in a calcite content of 2.0 wt% (value at t=0). For the large capillary used in the laboratory micro-CT & LXRPD study, ϕ=1.0 mm, the calcite content increased to about 3.6 wt% at 96 h, i.e. the calcite amount increased 1.6 wt%. This is now explicitly acknowledged in the footnote of Table S5. However, the paste within the much thinner capillary, ϕ=0.2 mm, used in the PXCT study did not show a significant carbonation. Now in the revised version of S.I., a footnote of Table S5:

"[#] The calcite content increased from 2.0 wt% at t=0 to 3.6 wt% at 96 h, highlighting a significant carbonation of the paste within this large capillary, i.e. 1 mm of diameter. The thinner capillary used in the PXCT study, i.e. 0.2 mm of diameter, did not show a measurable conversion of CH to Cc, see below. Carbonation of a cement paste has been previously measured by PXCT, when its extension was significant.[22]"

We have added new reference (22) in the S.I.: Trtik, P., Diaz, A., Guizar-Sicairos, M., Menzel, A. & Bunk, O. Density mapping of hardened cement paste using ptychographic X-ray computed tomography. *Cem. Concr. Compos.* **36**, 71–77 (2013)

3.2. In Table S7, data of AFm and C-A-S-H are missing. As Ca/Si ratio of C-S-H is very close to 1.7, not 1.8. Do authors have data related to C-S-H with Ca/Si 1.7. C-S-H gels are glassy phases so their values are within a certain range in Table S7. What is the range? The electron density of C-S-H and CH are close to each other. In most cases, the hydrating pastes, C-S-H and CH are mixed together with porosity, and hard to be distinguished. Once C-S-H and CH can not be distinguished, 4D nanoimaging of hydration can not be achieved because they are occupied up to 80% volume of hydrates.

Author reply-1: We agree that data for AFm and C-A-S-H were missed in Table S7. Thus, the expected data for AFm and hemicarbonate (Hc) phases are now included. We cannot include data for C-A-S-H as this component, with aluminium content larger than ~5 %, mainly forms in the pozzolanic reaction which is not the subject of this investigation.

Author reply-2: Concerning the variable Ca/Si ratio. C-S-H gel from PC hydration, without supplementary materials addition, shows variable Ca/Si ratios close to 1.7-1.8. This is now explicitly stated in the revised version of the manuscript "It should also be noted that the employed stoichiometry for C-S-H gel, i.e. $(CaO)_{1.80}(SiO_2)(H_2O)_{4.0}$,[56,57] is an assumption and slightly smaller Ca/Si ratios, ~1.70, have also been reported.[12,58]". Three new references (56-58) are added: (56) Cuesta, A. *et al.* Local structure and Ca/Si ratio in C-S-H gels from the hydration of blends of tricalcium silicate and silica fume. *Cem. Concr. Res.* **143**, 106405 (2021); (57) Zhu, X. & Richardson, I. G. Morphology-structural change of C-A-S-H gel in blended cements. *Cem. Concr. Res.* **168**, 107156 (2023); (58) Duque-Redondo, E., Bonnaud, P. A. & Manzano, H. A comprehensive review of C-S-H empirical and computational models, their applications, and practical aspects. *Cem. Concr. Res.* **156**, 106784 (2022).

We have calculate the values for $(CaO)_{1.7}(SiO_2)(H_2O)_4$ and compared them with those of $(CaO)_{1.8}(SiO_2)(H_2O)_4$. For the first average stoichiometry, the electron density and μ values would be 0.66 $e^-Å^{-3}$ and 102 cm^{-1}. The corresponding values for the second component are 0.66 $e^-Å^{-3}$ and 104 cm^{-1}. We do not report the values for $(CaO)_{1.7}(SiO_2)(H_2O)_4$ in Table S7 as they are, as expected, very close to those of $(CaO)_{1.8}(SiO_2)(H_2O)_4$.

Author reply-3: Concerning C-S-H and CH electron density values. Indeed, the electron density values of these components are close and in some regions, they are interspersed. We could disentangle these components by nano-imaging in most regions. However, the presence of partial volume effect was explicitly acknowledged in the manuscript and reproduced here: "… In any case, partial volume effect (the presence of components contributing below the spatial resolution of the measurements) is always taking place in cement pastes as some hydrates may have quite small particle sizes.[17]"

3.3. Some key points should be clarified. Raw clinker of cement is mixture. The microstructure of pastes includes time-evolving multi-phases with different multi-scale(nano-,meso-, and micro). Therefore, if PXCT enables to distinguish the amount and distribution of different phases, these phases should have "distinct" features in electron density derived from PXCT. Obviously, single test or measurement can not achieve this objective. Therefore, other test results and literature results should be carried out and compared to support the evidences in the manuscript. Please the review comment 3.7.

Author reply-1: The reviewer is right in pointing out that the cements are mixtures. This was detailed in the S.I. by reporting their mineralogical analyses. However, this is now clarified in the main text by adding: "… As reported in Table S2, the anhydrous cements are mixtures with more than eight crystalline phases."

Author reply-2: PXCT allows distinguishing components within the hydrating cement paste but it has limitations that are detailed in the manuscript. The two main limitations are: (i) the current spatial resolution, i.e. 250 nm. Clearly, component interspersed at smaller length scales cannot be disentangled, leading to partial volume effects. (ii) The electron density contrast is about 0.02-0.04 $e^{-}Å^{-3}$ and components with electron densities closer than ~0.04 $e^{-}Å^{-3}$ cannot be separated. However, to use additional techniques to *in situ* study the hydration of these cements (in addition to the already employed ones: calorimetry, laboratory powder diffraction and laboratory microtomography) will be the subject of further works, but this is not within the scope of the present investigation.

Description of Additional Supplementary Files

- File name: Supplementary Movie 1 - Summary of 4D nanoimaging of cement hydration

  Description: A summarized display of the cement paste hydration evolution as seen by this nanoimaging study. The progress of the different components is displayed after segmentation by Machine-Learning. Moreover, key changes like water porosity evolution or shrinkage development are highlighted on the video by embedded written text.

- File name: Supplementary Movie 2 - C-S-H shell characterization at 19 hours

  Description: A movie revealing the arrangement of the 3D segmented C-S-H shells through the 19 h nanoimaging dataset.